Trends in reactivity of oxides

applied to catalytic oxidation of hydrogen halides

Toftelund, Anja

Publication date:
2012

Document Version
Publisher's PDF, also known as Version of record

Trends in reactivity of oxides

- applied to catalytic oxidation of hydrogen halides

Ph.D. Thesis by Anja Toftelund

Supervised by
Thomas Bligaard and
Jan Rossmeisl

February 2012

Center for Atomic-scale Materials Design
Department of Physics
Technical University of Denmark

Preface

This thesis is submitted in candidacy for a PhD degree from the Technical University of Denmark (DTU). It is base on the work carried out at the Center for Atom-Scale Materials Design (CAMD), Department of Physics at DTU, from January 2007 to February 2012 under the supervision of Dr. Thomas Bligaard from Standford University and Associate Professor Jan Rossmeisl from DTU. Financial support has been provided from Haldor Topsoe A/S, Copenhagen Graduate School for Nano Science and Technology and from DTU.

First of all I would like to thank my supervisors. Thank you Thomas, for your enthusiastic and inspiring supervision, if nothing else would have been gained, working with you and getting to know you would have been worth all the effort anyway. Thank you Jan, for excellent and pleasant supervision, during the final part of my PhD, and for being there, when every body else left. It has not bin bad trade. Thanks to Berit Hinnemann form Haldor Topsoe for the great supervision on my work with the zeolites.

I would also like to thank Britt Hvolbæk, Hanne Falsig, Souheil Saadi, Jakob Howalt and my boy friend Morten Anthonsen for proof reading my thesis and helping with technical and time consuming details. Thanks to all my collaborators. Thanks to everybody who have shown their concern about my wellbeing during the final stressful weeks.

Thanks again to Morten, for the extensive help and support during the last period of my PhD. Thank you for taking care of our little family, and for our two lovely children, Nanna and Marie, we had during my PhD. Finaly, a special thank you to my mother for helping with the children.

Lyngby, February 2012
Anja Toftelund

Abstract

The results in this thesis are based on Density Functional Theory calculations.

The catalytic activity of oxides and other compound materials are investigated. It is found that the adsorption energy of the molecules NH_2, NH, OH and SH on transition metal nitride, oxide and sulfide surfaces scales linearly with the adsorption energy of their central N, O and S atoms. It is also found that they follow the same trend as in the case of adsorption of the same molecules on transition metals. The same type of scaling relations are also established between the adsorption energies of the halides (Cl, Br, and I) and OH on a wide range of rutile oxide surfaces.

Furthermore, Brønsted-Evans-Polanyi (BEP) relations are found for the adsorption of a large number of molecules (including Cl, Br and I) on transition metal oxides. In these relations the activation energies scale linearly with the dissociative chemisorption energies. It turns out that the BEP relation for rutile oxides is almost coinciding with the dissociation line, i.e. no barrier exists for the reactive surfaces.

The heterogeneous catalytic oxidation of hydrogen halides (HCl, HBr, and HI) is investigated. A micro-kinetic model is solved and the oxidation activities are compared at different coverage. Based on the obtained scaling relations two descriptors are identified that describe the reactions uniquely. By combining scaling with the micro-kinetic model, activity volcanoes for the three different oxidation reactions are derived. It is found that the commonly used RuO_2 catalyst for HCl oxidation is the closest to optimal for all three oxidation processes.

Finally, a study of transition metal substituted zeolites shows that relations similar to the above mentioned scaling applies for this type material.

Dansk resumé

Resultaterne i denne afhandling er baseret på beregninger udført vha. tæthedsfunktionalteori.

Den katalystiske aktivitet af oxider og andre sammensatte materialer er blevet undersøgt. Det konstateres, at adsorbtionsenergien af molekylerne NH_2, NH, OH og SH på overfladerne af overgangsmetalnitrid, -oxid og -sulfid skalerer lineært med adsorbtionsenergien af det centrale N, O og S atom. Det er også fundet at de følger samme tendens som adsorbtion af de samme molekyler på overgangsmetaller. Den samme type skaleringsrelation er etabeleret mellem adsorbtionsenergier af haliderne (Cl, Br og I) og OH på en lang række rutile oxidoverflader.

Den heterogene katalytiske oxidation af hydrogenhalogenider (HCl, HBr og HI) er blevet undersøgt. En mikrokinetisk model er blevet løst og oxidationsaktiviteterne ved forskellige dækningsgrader er sammenlignet. Baseret på de opnåede skaleringsrelationer er to deskriptorer identificeret som entydigt beskrivende for reaktionerne. På basis af skaleringsrelationerne og den mikrokinetiske model udledes den katalystiske aktivitet som funktion af adsorbtionsenergien (den såkaldte vulkankurve) for tre forskellige oxidationsreaktioner. Det er fundet, at den almindeligt anvendte RuO_2 katalysator for HCl oxidation er tættest på optimal for alle tre oxidationsprocesser.

Sidst i afhandlingen viser et studie af overgangsmetal-substituererettzeolitter at skaleringsrelationer svarende til den ovenfor nævnte relation, også er gældende for denne type materialer.

List of Papers

Paper I

Scaling Relationships for Adsorption Energies on Transition Metal Oxide, Sulfide, and Nitride Surfaces

Eva M. Fernández, Poul G. Moses, Anja Toftelund, Heine A. Hansen, José I. Martínez, Frank Abild-Pedersen, Jesper Kleis, Berit Hinnemann, Jan Rossmeisl, Thomas Bligaard, and Jens K. Nørskov

Angew. Chem. Int. Ed. 2008, 47, 4683-4686

Paper II

On the behavior of Brønsted-Evans-Polanyi relations for transition metal oxides

A. Vojvodic, F. Calle-Vallejo, W. Guo, S. Wang, A. Toftelund, F. Studt, J. I. Martínez, J. Shen, I. C. Man, J. Rossmeisl, T. Bligaard, J. K. Nørskov, and F. Abild-Pedersen

The Journal of Chemical Physics 134, 244509 (2011)

Paper III

Universal transition state scaling relations for (de)hydrogenation over transition metals

S. Wang, V. Petzold, V. Tripkovic, J. Kleis, J. G. Howalt, E. Skúlason, E. M. Fernández, B. Hvolbæk, G. Jones, A. Toftelund, H. Falsig, M. Björketun, F. Studt, F. Abild-Pedersen, J. Rossmeisl, J. K. Nørskov and T. Bligaard

Phys. Chem. Chem. Phys., 2011, 13, 20760-20765

Paper IV

Volcano Relations for Oxidation of Hydrogen Halides over Rutile Oxide Surfaces

Anja Toftelund, Isabela C. Man, Heine A. Hansen, Frank Abild-Pedersen, Thomas Bligaard, Jan Rossmeisl, and Felix Studt

Submitted

Contents

Chapter 1

Introduction

The topics of this thesis are all within the field of heterogeneous catalysis. Heterogeneous catalysts are used to clean emissions from cars, power plants and industrial production, and they also play a key role in the production of a large range of products including fuels, fertilizers, plastics, and pharmaceuticals. It has been estimated that more than 20% of all industrial production worldwide is dependent on heterogeneous catalysis [1]. A heterogeneous catalyst is a solid that facilitates a chemical reaction by adsorbing the reacting molecules on its surface. When the molecules are bound to the surface, the barrier for the chemical reaction is reduced and the rate at which the product is produced is enhanced by many orders of magnitude.

Many catalysts today are transition metal nanoparticles, and supported on a porous material in order to enhance the surface area. In many cases the transition metal of interest is rare and expensive. Therefore, and because of the increasing demands of an increasing population, we need to look at alternative materials in order to develop better and cheaper catalysts. Oxides are good alternatives to the transition metals and considerable progress has been made in the theoretical description of the reactivity of transition metal oxides [2, 3, 4, 5, 6, 7, 8]. However, due to their complexity the understanding of these materials is not as well established as for the transition metal.

Linear relations established between adsorption energies of molecules on different catalytic surfaces are very useful tools in the investigations of heterogeneous catalysis [9, 10, 11]. If we would like to design a new catalyst for a specific reaction, we need to make a thorough analysis of the kinetics

of the reaction over a range of catalysts. However, we would need many parameters like adsorption and activation energies just to do the analysis of a single catalytic surface. By employing linear energy relations we can get information for a large number of catalysts from only a few data points. In this way we can make models of the trends in the reactivity for a range of catalysts.

The energy relations in question here are the scaling relations [12, 13] and the Brønsted-Evans-Polanyi (BEP) relations [14, 15]. The former are linear relations between adsorption energies of different reaction intermediates and BEP relations are linear relations between the activation energy and reaction energy of an elementary reaction step of a catalytic reaction. On transition metal it has been shown that an universal BEP line exists, that it, they obey a reactant independent but geometry dependent linear relation [16, 17, 18, 19].

Ruthenium oxide has recently been established as a good catalyst for oxidation reactions [20]. In this thesis, the focus is on the oxidation of hydrogen halides (HCl, HBr and HI), which results in the production of halides Cl_2, Br_2, and I_2. Halides are versatile compounds in the chemical industry with chlorine being the most important one. Chlorine is produced at scales of mega tonnes per year. It is used as disinfectants and for water treatment. Bromine and iodine are produced at much smaller scales. Bromine has recently attracted attention as it was suggested to be used in small to medium-scale gas to liquid processes[21, 22] where Br_2 can be used to brominate methane or other alkanes into alkyl bromide in the formation of longer alkanes. In this process Br_2 needs to be completely recovered from HBr.

Chlorine is mainly produced via electrochemical reduction of chloride salt solutions[23]. Alternatively it can also be produced via oxidation of HCl (the Deacon process)[24, 25]. This process consumes much less energy compared to the electrochemical processes [26]. Bromine as well as iodine is usually produced via oxidation with chlorine gas [23]. The oxidation of HBr and HI with air via a process similar to the Deacon process, however, should in principle be possible as well and recycling of bromine via oxidation could potentially become one of the key steps in the economically viable catalytic gas to liquid process described above.

Industrial production of chlorine via the Deacon process utilizes a RuO_2 catalyst supported on TiO_2 [25]. There are a few theoretical studies for this

process [8, 27, 28, 29, 30] a theoretical analysis regarding a similar process for HBr and HI oxidation, however, is still missing.

Zeolites are very interesting oxides as they are both porous and catalytically active. They are already widely used in the petrochemical industry, but they are also used in water purification, nuclear industry and as a water softener in laundry detergents [31]. Zeolites can be a good cheap alternative to the solid catalysts. The theoretical knowledge the important parameters of their reactivity is confined. Mainly due to their large unit cells it is only within the recent years, it has been able to perform first principal calculations of the periodic structure of bulk zeolites [32, 33, 34, 35, 36].

The overall aim of this PhD work is via Density Functional Theory (DFT) calculations to provide new insight to the catalytic activity of oxides, by establishing trends in important parameters, and by combining these with micro-kinetic modeling investigate the heterogeneous catalytic oxidation process of hydrogen halides over rutile oxide surfaces. Furthermore, a study of structure and reactivity of zeolites is included.

In chapter 2, a short introduction is given to DFT and related parameters and methods specific to the work included in this thesis.

In chapter 3 about linear energy relations, the concepts of scaling and BEP relations are explained and both types of linear scaling relations are established for compound materials.

In chapter 4, thermodynamics and micro-kinetic methods used in the work of this thesis are introduced.

In chapter 5 a micro-kinetic trend study of the heterogeneous catalyzed oxidation of hydrogen halides over rutile oxide surfaces is given.

In chapter 6 a kinetic expression is obtained for adsorption of larger molecules.

In chapter 7, work regarding the structure and activity of zeolites is presented.

Chapter 2

Density functional theory

A system consisting of a large number of interacting electrons and atomic nuclei can be described within the framework of quantum mechanics by the Schrödinger equation. The complexity of finding the exact solution to the Schrödinger equation increases, however, rapidly with the number of particles in the system. Due to the large difference in mass of an electron and a nuclear, the nuclei are almost unaffected by the movement and localization of the electrons. Therefore, with the Born-Oppenheimer approximation the nuclei can be treated as stationary while the electrons move around them [37]. Despite this simplification the Schrödinger equation still cannot be solved. Density functional theory [38, 39, 40, 41], however, provides a scheme for solving this problem.

The foundation of density functional theory was provided by Hohenberg and Kohn in 1964 [42]. They stated that all properties of the ground state of a given electronic system can be determined uniquely by the electronic density and that all terms of the total energy of a ground state system can be described by a functional of the density. Hohenberg and Kohn did, however, not provide a method for determining the ground state density.

A direct approach to solve this problem was given by Kohn and Sham in 1965 [43]. They presented a calculational scheme for computing the total energy, where the problem of many interacting electrons was reduced to a problem of a set of non-interacting electrons in an external field. Kohn and Sham proposed to write the total energy as:

$$E_{\mathrm{tot}}(n) = E_{\mathrm{kin}}^{\mathrm{non-int}}(n) + E_{\mathrm{ext}}(n) + E_{\mathrm{Hartree}}(n) + E_{\mathrm{xc}}(n), \tag{2.1}$$

where $E_{\mathrm{kin}}^{\mathrm{non-int}}(n)$ is the energy of a non-interacting electron gas, $E_{\mathrm{ext}}(n)$

is the external energy given by the nuclei, and $E_{\text{Hartree}}(n)$ is the classical Hartree term constituting the Coulombic repulsion between all electronic charges.

$E_{\text{xc}}(n)$ is the exchange-correlation energy, and is the only term of (2.1) that is unknown. It is by definition the remaining part of the electronic contribution to the total energy. There are two contributions to $E_{\text{xc}}(n)$, the exchange energy E_{x} and the correlation energy E_{c}.

E_{x} is the most significant contribution to the exchange-correlation energy and is due to the Pauli exclusion principle, which states that electrons of the same spin cannot exist in the same state. This means that around an electron all other electrons of the same spin avoids this electron. This reduces the average Coulomb repulsion of that electron, and the energy gained by this is the exchange energy. This results in a positive region around each electron called the exchange hole. The correlation energy E_{c} is the rest of the exchange correlation energy E_{xc} and results from many-body effects, mainly the coulomb interaction between electrons of opposite spin [38].

The ground state density entering the total energy (2.1) can be obtained from the Kohn-Sham equations [43].

$$\left(-\frac{1}{2}\nabla^2 + v_{\text{eff}}(\mathbf{r})\right)\psi_i(\mathbf{r}) = \varepsilon_i\psi_i(\mathbf{r}), \tag{2.2}$$

and the electron density, is in terms of the Kohn-Sham wave-function

$$n(\mathbf{r}) = \sum_{i=1}^{N} |\psi_i(\mathbf{r})|^2 , \tag{2.3}$$

where i runs over all electrons, and ε_i is the Kohn-Sham eigenvalue of electron i.

v_{eff} is the sum of the external potential, v_{ext}, the classical Hartree term, v_{Hartree}, and the exchange and correlation potential, v_{xc},

$$v_{\text{eff}}(\mathbf{r}) = v_{\text{ext}}(\mathbf{r}) + v_{\text{Hartree}}(\mathbf{r}) + v_{\text{xc}}(\mathbf{r}) \tag{2.4}$$

The external potential is normally the potential generated by the nuclei. The Hartree term is the potential of the classical Coulomb interactions between the electrons and the exchange and correlation potential constitutes all the nonclassical contributions to the potential.

This set of equations can be solved iteratively. Starting by constructing, v_{eff}, using a trial density, whereafter equation (2.2) can be solved and the

density can be found from equation (2.3). The new density can then be used to calculate v_{eff} again. This procedure is continued until self-consistency is obtained.

2.1 Exchange and correlation functionals

In order to obtain a reasonable result from the Kohn-Sham scheme an exchange-correlation functional has to be applied. As the approximation of the exchange-correlation energy constitutes the largest part of the error in density functional calculations, many approaches have been used to improve the functional. The approximations for E_{xc} most generally used are the local density approximation (LDA) and the generalized gradient approximation (GGA).

In LDA the exchange and correlation energies per particle, ε_{x} and ε_{c}, of the homogeneous electron gas, are used to calculate the exchange and correlation energies of the inhomogeneous system:

$$E_{\text{xc}}^{\text{LDA}}(n) = \int \mathrm{d}\mathbf{r} n(\mathbf{r})(\varepsilon_{\text{x}}^{\text{unif}}(n) + \varepsilon_{\text{c}}^{\text{unif}}(n)). \tag{2.5}$$

This approach, despite its simplicity performs surprisingly well for a large number of systems also including systems with large variations in the density [44, 41]. Due to quantum Monte Carlo methods accurate values of $\varepsilon_{\text{c}}^{\text{unif}}$ are available [45].

In order to account for the variations in the electron gas the gradient of the electron density has been introduced in the GGA approach. Furthermore, the criteria that the exchange hole around an electron contains exactly minus one electron is satisfied [46]. The form of the GGA exchange functional is not unique, and a large number of different functionals have been provided. In general the GGA exchange energy can be written in the form:

$$E_{\text{xc}}^{\text{GGA}}(n,s) = \int \mathrm{d}\mathbf{r} n(\mathbf{r}) \varepsilon_{\text{x}}^{\text{GGA}}(n) = \int \mathrm{d}\mathbf{r} n(\mathbf{r}) \varepsilon_{\text{x}}(n) F_{\text{x}}(s), \tag{2.6}$$

where $F_{\text{x}}(s)$ is the exchange enhancement function.

$$s = \frac{|\nabla n|}{2 k_F n} \tag{2.7}$$

is the reduced density gradient and k_F is defined by $n = k_F^3/(3\pi^2)$.

In this thesis the GGA functional RPBE [47] is used. The RPBE enhancement function is given by:

$$F_{\mathrm{x}}^{\mathrm{RPBE}}(s) = 1 + \kappa \left(1 - \mathrm{e}^{-\mu s^2/\kappa}\right), \tag{2.8}$$

where $\mu = 0.21951$ is chosen in such a way that the expansion around $s = 0$ gives the correct linear response in the limit of the homogeneous electron gas and $\kappa = 0.804$ is chosen in order to fulfill the local Lieb-Oxford bound [48]. The RPBE functional gives good results for atomization energies chemisorption energies.

2.2 Implementation

In order to implement DFT in a computational code, further approximations have to be made. In the work of this thesis the DFT-code Dacapo [49] is use. In Dacapo a plane wave basis are employed to describe the valence electrons, while the core electrons are described by pseudo-potentials.

2.2.1 Plane wave basis set

In order to solve the Kohn-Sham equations numerically, the Khon-Sham wave-functions are in the case of Dacapo described by a set of plane wave basis functions. This choice of plane waves as a basis requires the system to be solved in a cell with periodic boundary conditions. This, however, makes the code well suited for investigating bulk crystal structures, which are periodic in all three dimensions. By introducing vacuum regions, two dimensional systems like surfaces can also be calculated. In this case a slab of a reasonable number of layers of atoms is build in order to simulate the surface. Also molecules can be calculated by introducing vacuum in all three dimensions.

In principle an infinite number of plane waves are needed in order describe the wave functions correct. However, in practice we need to set an energy cut-off in order to limit the plane waves to a finite number. Even though the number of plane waves has been made finite by introducing a cut-off energy, the wave function would in principle have to be evaluated over an infinite number of k-points in the first Brillouin zone. In practice only very few k-points are needed. An energy cut-off of at least 350 eV is used for the calculation in this thesis, and the k-points are sampled with a Monkhorst-Pack grid [50]

2.2.2 Pseudo-potentials

The core electrons are confined to a small region near the nucleus, and are not influenced by the chemistry that the atoms take part in. Therefor, it is a good approximation to freeze the core electrons. In Dacapo the core electrons are represented by Vanderbild ultra-soft pseudo-potentials [51]. The potentials are constructed such that it coincide with the real potential at a certain cut-off radius.

2.3 Application

For any real application we need be able to determine the most stable atomic configuration of a system. Due to the Born-Oppenheimer approximation mention above the electrons and ion cores can bee treated separately and we can apply a minimization algorithm for this purpose. However, the minimum of the potential well found by this method is not the actual ground state with respect to atomic vibrations. A zero-point energy correction E_{ZPE} is added in order to find the vibrational ground state energy at 0 K. E_{ZPE} is found by displacing the atoms and calculating the vibrational modes ν_i in a harmonic approximation.

$$E_{\mathrm{ZPE}} = \frac{1}{2}\sum_i h\nu_i \tag{2.9}$$

In practice this is not necessary to do for all atoms in a system. For tightly bound atoms, e.g. in a bulk structure this correction is infinitesimal. For both adsorbed and in gas phase molecules, especially if they contains hydrogen, the correction can be significant.

When the ground state energy are found, we can calculate chemical properties. In the work of this thesis a huge number of adsorption energies are found. These are calculated as

$$\Delta E_{\mathrm{ads}} = E(\mathrm{surface} + \mathrm{molecule}) - E(\mathrm{surface}) - E(\mathrm{molecule}) \tag{2.10}$$

The transition states are of a reaction are found either by the nudged-elastic-band method [52, 53] or by a fixed bond length approach [54], where the potential energy surface defined by the ionic cores, are is searched in a stepwise manner in order to find the transition state saddle point.

Chapter 3

Linear energy relations

3.1 Scaling Relations

This section about scaling relations is based on the included [Paper I] where adsorption energie of small intermediates on compound surfaces are shown to scale linearly. A recent equivalent study by Abild-Pedersen et. al. [12] showed the same kind of relations on transition metal surfaces. In this study the adsorption energy of CH_x, $x = 0, 1, 2, 3$, NH_x, $x = 0, 1, 2$, OH_x, $x = 0, 1$ and SH_x, $x = 0, 1$ on a range of close-packed and stepped transition metal surface was calculated using DFT. In figure 3.1 the binding energy, ΔE^{AH_x}, of the intermediates AH_x (A=C, N, O or S) is plotted against the adsorption energy, ΔE^{A}, of atom A. The figure shows that for each type of adsorbate on close-packed or stepped surface there exist a linear relation of the type

$$\Delta E^{\mathrm{AH}_x} = \gamma(x)\Delta E^{\mathrm{A}} + \xi \tag{3.1}$$

An interesting observation is it that the slope γ is approximately given by

$$\gamma(x) = (x_{\max} - x)/x_{\max} \tag{3.2}$$

where $x_{\max}$ is the number of hydrogen atoms that is needed by the central atom A in order to become a neutral gas-phase molecule. $x_{\max} = 4$ for A=C, $x_{\max} = 3$ for A=N and $x_{\max} = 2$ for A=O, S.

In figure 3.1, some of the scatter around the line can be explained by different types of adsorption site on the surface. For example, CH_3 prefers a one-fold adsorption site on the close-packed surface, while C prefers a three-fold site. In figure 3.2, the adsorption energy of CH_3 is plotted as a function

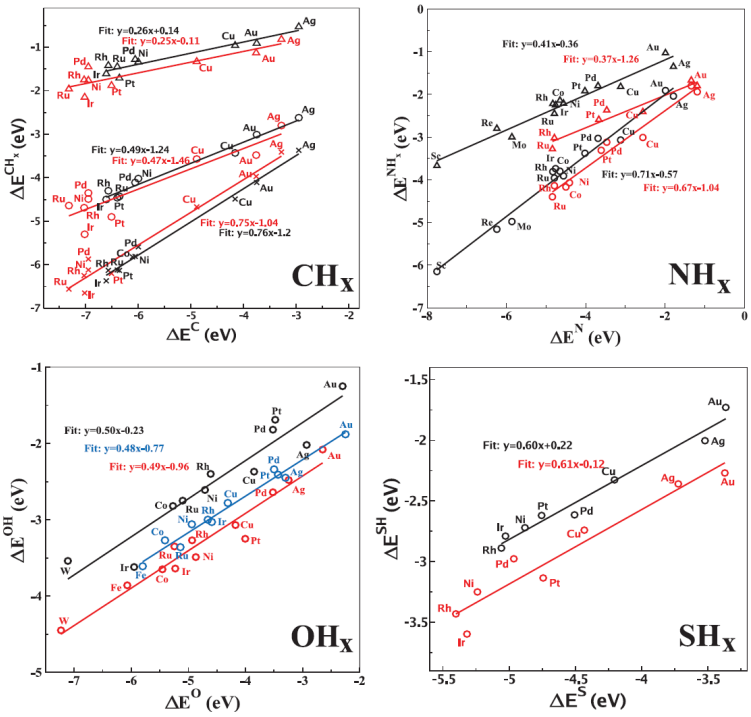

Figure 3.1: Adsorption energies of CH_x intermediates (crosses: $x = 1$; circles: $x = 2$; triangles: $x = 3$), NH_x inter- mediates (circles: $x = 1$; triangles: $x = 2$), OH, and SH inter- mediates plotted against adsorption energies of C, N, O, and S, respectively. The adsorption energy of molecule A is defined as the total energy of A adsorbed in the lowest energy position outside the surface minus the sum of the total energies of A in vacuum and the clean surface. The data points represent results for close-packed (black) and stepped (red) surfaces on various transition-metal surfaces. In addition, data points for metals in the fcc(100) structure (blue) have been included for OH_x. Adapted from [12].

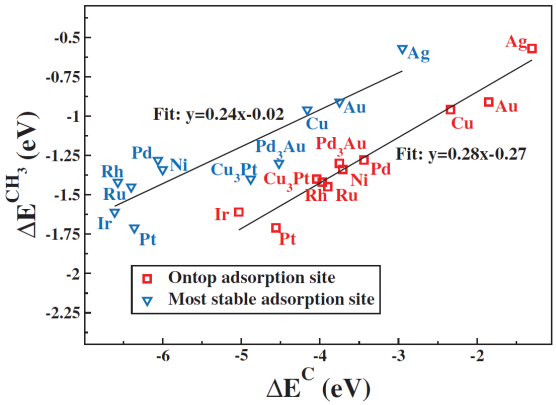

Figure 3.2: Binding energies of CH_3 plotted against the binding energies of C for adsorption in the most stable sites (triangles) and in the case where both CH3 and C have been fixed in the on-top site (squares). Adapted from [12].

of C adsorbed at a one-fold site. This reduces the scatter significantly. Also a few alloys are included in this figure and as it is seen the scaling relation also apply for those.

In a similar study [Paper I] we have found that these scaling relations also exists for the more complex compound materials. We have performed DFT calculations of the same kinds of molecules on oxide, sulfide and nitride surfaces. For the nitride surfaces both a clean surface and a surface with a nitrogen vacancy were studied. For the oxide and sulfide surfaces an oxygen or sulfur covered surface with an oxygen or sulfur vacancy were studied. The structures of the clean surfaces of the considered compounds are shown in figure 3.3. The adsorption energies of the molecules are plotted in figure 3.4 as a function of the adsorption energy of their central atoms, in the same way as for the metal surfaces. The fitted slopes are given approximately by the same expression as in equation (3.2). It is, therefore, interesting to compare the results for adsorption on compound surfaces in figure 3.4 with the results for adsorption energies on transition metal surfaces in figure 3.1. In figure 3.5, the scaling relations for the two classes of surfaces are in the same plots. The black stars are the results for the transition metals and the dashed lines are no longer the best fitted lines, but the best fits with slopes obtained from equation (3.2). It is found that the linear relations

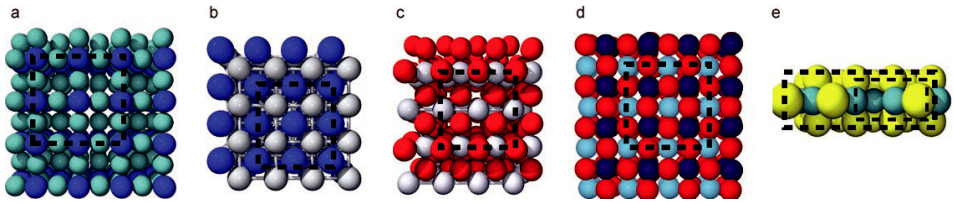

Figure 3.3: Structures of the investigated transition metal nitride, oxide and sulfide surfaces. a) Fcc-like structure for the M_2N (100) surfaces, M = Mo and W. Dark and light blue spheres represent metal and N atoms, respectively. b) Fcc-like rock-salt structure for TiN (100) surface. Dark blue and gray spheres represent Ti and N atoms, respectively. c) Rutile-like (110) surfaces for the MO_2 surfaces, M=Ir, Ru, Pt and Ti. Red and white spheres represent O and metal atoms, respectively. d) Perovskite structure for the $LaMO_3$ (100) surface, with M = Ti, Ni, Mn, Fe, and Co. Red, purple, and violet spheres represent O, La, and metal atoms, respectively. e) Hcp-like (-1010) surfaces for NbS_2, TaS_2, MoS_2, WS_2, Co-Mo-S, Ni-Mo-S, and Co-W-S. Yellow and green spheres represent S and metal atoms, respectively. The black dashed boxes indicate the unit cell. Adapted from [55].

for NH_x are essentially the same for the two classes of systems. Though the relation for NH_2 seems to have a slightly steeper slope than the one predicted by (3.2). For OH and SH there is a shift in the results for the transition metals compared to those for the compound materials. This can be explained by differences in the local geometry of adsorption sites on the two classes of surfaces. On oxides, OH and O in general binds to a single metal atom, while they on metals generally are found to coordinate with more than one metal atom. Likewise sulfur adsorbs at bridge site on the sulfides, while it prefers the fivefold coordinated site on stepped transition metal surfaces. If we plot adsorption energies of O and OH, where they are forced to adsorb in an on-top position and S and SH at a bridge site on the transition metals the results fall on the same line (blue crosses) as those for the compound surfaces.

Compounds are considerably more complex to understand than transition metal. However, the observation above indicates that the underlying physics of the adsorption bond is similar for the compounds as for the transition metals. In case of the transition metal the *d*-band model can give a

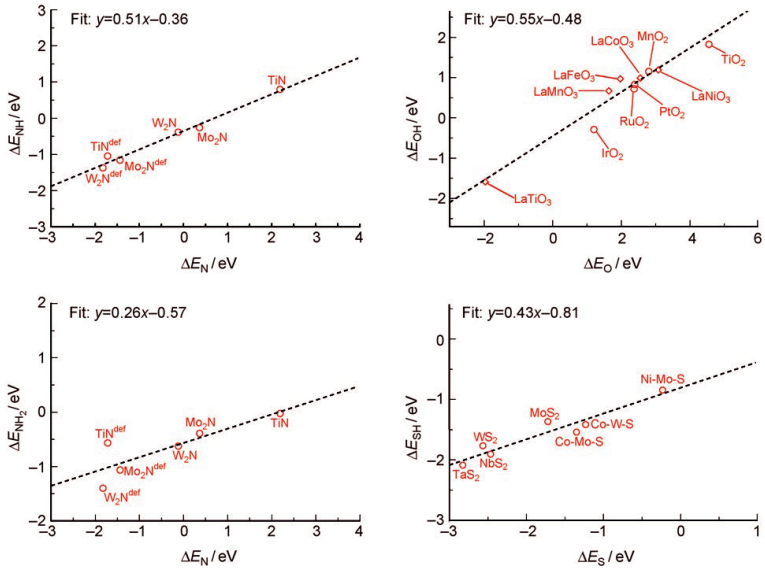

Figure 3.4: Adsorption energies of NH and NH2 intermediatesover nitrides, an OH intermediate over oxides, and an SH intermediate over sulfides plotted against adsorption energies of N over nitrides, O over oxides, and S over sulfides, respectively. The energies are plotted with respect to the gas-phase energies of AH_{max} and H_2.

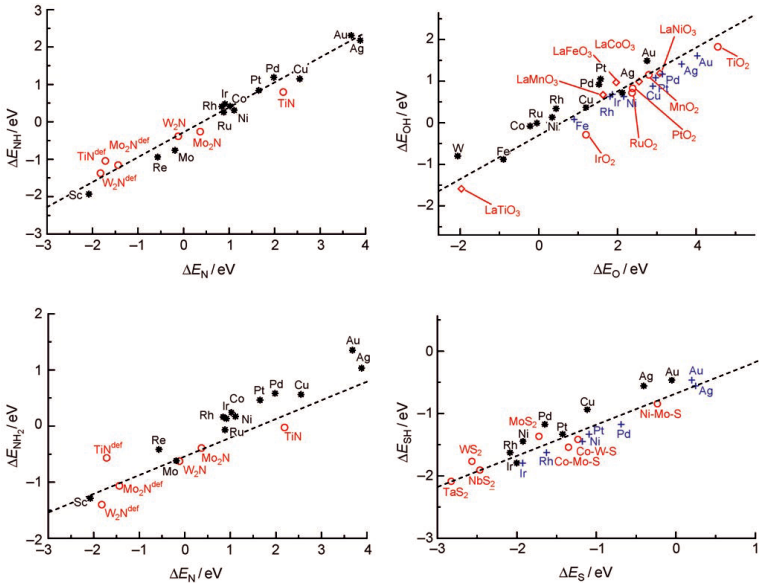

Figure 3.5: Adsorption energies for AH_x types of molecules on compound surfaces as in figure 3.4 (red circles). The same on transition metal surfaces (black stars).The adsorption energies for the OH intermediate on a top site and S intermediates on a bridge site over transition metal centers are included (blue points). The dashed line isthe slope $\gamma(x)$ obtained from equation (3.2).

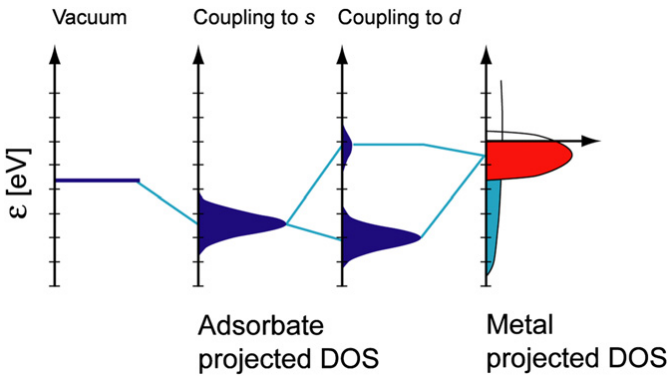

Figure 3.6: Schematic presentation of the bond formation of a chemical bond between an adsorbate valance level and the *s*- and *d*-states of a transition metal surface. Adapted from [10].

good understanding for the observed scaling relations. The *d*-band model is briefly described in the following section.

3.1.1 *d*-band model

The variation in adsorption energy from one transition metal surfaces to the next can be explained by the *d*-band model [56, 57, 58].

Since the *s* states are very delocalized on the metal atoms the overlap is large and therefore the *s* state of a metal has a band, which is broad in energy. The *d* orbitals on the contrary are very localized and therefore the *d* states form a narrow and dense band, due to the small overlap. This is shown schematically in the right panel of 3.6.

In the *d*-band model the adsorption is thought of as divided into two steps. First, the valence states of the adsorbate are coupled to the *s* states of the metal and thereafter, they couple to the *d*-states. This means that the adsorption energy can be divided into two contributions:

$$\Delta E = \Delta E_{sp} + \Delta E_d \tag{3.3}$$

In figure 3.6 the bond formation is shown schematically for a single adsorbate state. First, this sharp valence state of the adsorbate is broadened and shifted down in energy due to the interaction with the *s*-band. This gives rise to the main part of the adsorption energy. Next step is the interaction with the *d*-band, which only contributes with a small amount to

the adsorption energy. Because the d-band is confined in energy this coupling is equivalent to a two-level problem, which gives rise to bonding and anti-bonding states.

Since the s-states of all the transition metals are broad, free electron like and always half filled [59], there is no significant difference from metal to metal in the coupling to the s-states. The variations between the metals can therefore be explained exclusively by the coupling to the d-states. One important factor is the filling of the d-states. As we move toward left in the periodic table the filling of the d-band of the transition metals decreases, which means that the center of the d-band moves up in energy with respect to the fermi-level. As the d-band center moves up in energy, so does the bonding and anti-bonding states of the adsorbate and consequently the anti-bonding states will become depopulated and the bond to the surface strengthened. Another important factor is the size of overlap between the adorbate states and the d-state. The larger the overlap the larger repulsion due to the Pauli exclusion principal. This term increases to the left and down through the periodic table.

3.1.2 Model of scaling laws for adsorption energies

The linear relations in equation (3.1) can be explained by the d-band model described above. According to the d-band model all variations in the adsorption energies between the different transition metals are given by the d-band. Therefore, the x-dependence must be given by the coupling to the d-band alone. Considering the kind of linear relationships found in figure 3.1 it is reasonable to assume that the coupling of AH_x to the d-band is proportional to γ:

$$\Delta E_d^{AH_x} = \gamma(x)\Delta E_d^{A} \tag{3.4}$$

In terms of the d-band model this will lead directly to equation (3.1):

$$\begin{aligned}\Delta E^{AH_x} &= \Delta E_d^{AH_x} + \Delta E_{sp}^{AH_x} = \gamma(x)\Delta E_d^{A} + \Delta E_{sp}^{AH_x} \\ &= \gamma(x)\left(\Delta E^{A} - \Delta E_{sp}^{A}\right) + \Delta E_{sp}^{AH_x} \\ &= \gamma(x)\Delta E^{A} + \xi\end{aligned} \tag{3.5}$$

where $\xi = \Delta E_{sp}^{AH_x} - \gamma(x)\Delta E_{sp}^{A}$ only includes terms of sp-coupling, and therefore is independent of the given metal.

We still need to answer the question; Why does the adsorption d-coupling scale with the valency of the molecule? This can be justified with the help of the effective medium theory [60]. Within the effective medium theory, the bonding of an A atom to other atoms (surface and hydrogen atoms) is approximated by the interaction with an homogeneous electron gas. The homogeneous electron gas has the same density as the one given by the surrounding atoms at the location of the A atom. In general, the bond energy of an atom embedded in such a homogeneous electron gas has a minimum for a specific electron density, n_0, and the adsorption geometry will depend on where the atom experiences this optimal electron density. If a hydrogen atom is added to the A atom the electron of the hydrogen will be added to the electron density that the A atom is feeling. Therefore the A atom now needs a lower electron density from the surface, n_{surf}. This will be adjusted by changing the adsorption geometry, e.g. the adsorption site or bond length. Hydrogen atoms can be added to the central atom A until $x_{\max}$ hydrogen atoms is reached. In this case the molecule no longer binds to the surface (neglecting Van der Waals interactions), i.e. the density needed from the surface is $n_{\text{surf}} = 0$. Assuming that all hydrogen atoms contributes with the same amount to the electron density and that the optimal density for the A atom is n_0, the following is found for the electron density needed at the surface.

$$n_{\text{surf}} = \frac{x_{\max} - x}{x_{\max}} n_0 = \gamma(x) n_0 \tag{3.6}$$

The coupling between the molecular state and the metal states is proportional to n_{surf} and therefore also proportional to ΔE_d [12]. We get

$$\Delta E_d (\propto V_{ad}^2) \propto n_{\text{surf}} \propto \frac{x_{\max} - x}{x_{\max}} = \gamma(x) \tag{3.7}$$

which is in agreement with (3.1).

As the metal atoms in the compound surfaces also have very confined and localized *d*-states near the Fermi-level, similar arguments should hold for transition metal oxides, nitrides and sulfides [61, 62]. Therefore we observe the same behavior for the two classes of systems in figure 3.5.

In [Paper III] and [Paper IV] (Chapter 5) it is shown that scaling relations are not necessarily confined to apply for adsorption energies of molecules with the same central atoms. Here we present scaling relations between hydrogen and C, N and O on transition metal surfaces and the scaling between Cl, Br, I and OH on rutile oxides.

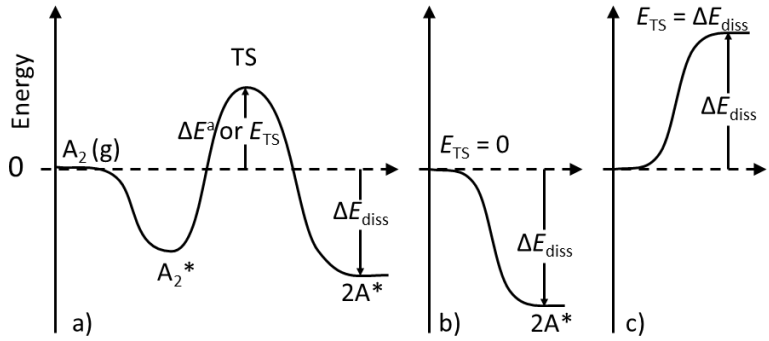

Figure 3.7: Schematic energy diagram of the dissociative chemisorption of a diatomic molecules. The energies relevant for the BEP lines are indicated in panel a). Panel b) and c) show the special cases for very reactive and very noble rutile surfaces, respectively.

3.1.3 Applying scaling

A part from providing an understanding of the physics underlying adsorption mechanisms, scaling relations are also a strong tool when searching for good catalysts. Having the appropriate scaling relations for a given reaction, it is quite easy to obtain reaction energies for large range of surfaces. If one has a calculated or an experimental adsorption energy of an adsorbate AH_x ($\Delta E_{\mathrm{M1}}^{\mathrm{AH}_x}$) for one transition metal, alloy or compound, M1, we can estimate the energy $\Delta E_{\mathrm{M2}}^{\mathrm{AH}_x}$ of the same intermediate on another system, M2, from the adsorption energies of atom A on the two systems by using the following equation.

$$\Delta E_{\mathrm{M2}}^{\mathrm{AH}_x} = \Delta E_{\mathrm{M1}}^{\mathrm{AH}_x} + \gamma(x)\left(\Delta E_{\mathrm{M2}}^{\mathrm{A}} - \Delta E_{\mathrm{M1}}^{\mathrm{A}}\right) \tag{3.8}$$

where $\gamma(x)$ is a rational number given by equation (3.2). If we have a database of atomic adsorption energies for a number of systems, we may then estimate the adsorption energy of a number of intermediates. This opens for the possibility of obtaining an overview of adsorption energies on oxides, sulfides, and nitride surfaces on the basis of a few calculations.

3.2 Brønsted-Evans-Polanyi Relations

In the field of heterogeneous catalysis or surface chemistry Brønsted-Evans-Polanyi (BEP) relations [14, 15] are linear energy relations between the

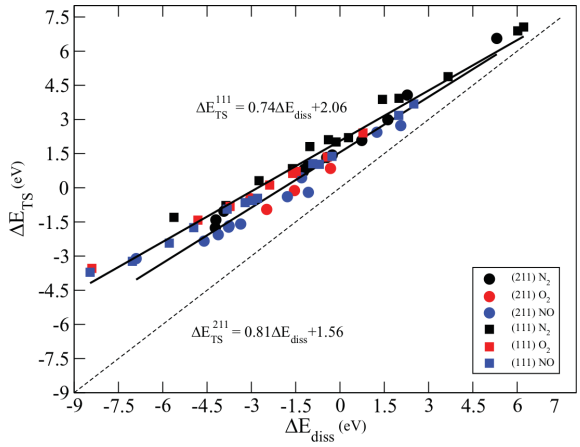

Figure 3.8: Calculated transition state energy as a function of dissociative chemisorption energy of diatomic molecules on (111) and (211) transition metal surfaces. The solid black line is a fit to the data points and the dashed indicates the dissociation line ($E_{\mathrm{TS}} = E_{\mathrm{diss}}$).

activation energy or transition state energy and the reaction energy of a surface reaction usually measured relative to the gas-phase energy of the reactant. The relation between the activation energy and the reaction energy are often found roughly to be a linear function of the form

$$E_{\mathrm{TS}} = \alpha \Delta E_{\mathrm{diss}} + \beta \tag{3.9}$$

where ΔEdiss is the dissociative adsorption energy of the reactant (See figure 3.7 a)). In equation (3.9) another notation have been given for the slope and intersection compared to scaling relations, because we are now looking at a different class of linear energy relations. However, it is the same physics that lies behind the adsorption of intermediate molecules and a transition state configuration. Therefore, the BEP lines can be regarded as a special category within the concept of scaling relations. This section is based on the included papers [Paper II] and [Paper III] both concerning BEP relations.

I figure 3.8 from [Paper II], the transition state energy for the dissociation of a number of diatomic molecules over close-packed and stepped transition metal surfaces has been plotted against the dissociative adsorption energy. Here the database of energies from [17] has been extended

by including surfaces in a boarder reactivity range, and slightly different expressions are found for the BEP relations. The conclusion is, however, the same. It it seen that not only do the transition state energy for each molecule fall on a line, but also that the transition-state energy for each type of surfaces falls on the same line for all the different molecules. This interesting finding, referred to as "universality" is due to the fact that all transition states strongly resemble the final state for this type of reaction. Furthermore, the transition states also resemble each other from one type of molecule to the next. This leads to the same relation for all the molecules seen in the figure. The different lines for stepped and closed-packed surfaces are a result of the different geometries of the transition states. Due to the geometry of a stepped surface the transition state can be stabilized by more surface atoms than on the close-packed surface. In the case of O_2, the slopes are a little lower than for the other molecules. This is due to the geometrical configuration of the transition state not being quite as final-state-like as the for the rest of the molecules.

This universality principle also exists for most oxide. In [Paper II] we have calculated transition state energies for the dissociation of a large number of small molecules over oxide surfaces. In the case of rutile (110) surfaces these are plotted in figure 3.9 as a function of dissociative chemisorption energies. In the top panel the BEP lines for dissociation of diatomic molecules over two cus (coordinative unsaturated) sites are shown. Very interestingly all points except very few fall on the dissociation line ($E_{\mathrm{TS}} = E_{\mathrm{diss}}$) meaning that the reaction happens with out an extra transition state barrier. Either the reaction path is uphill in potential energy all the way (figure 3.7 c)) or it is exclusively downhill, i.e. no saddle point is found in the potential energy surface along the path (figure 3.7 b)). For systems where dissociation of the reactant occurs without an barrier as in figure 3.7 b) the term transition state becomes completely undefined. In this case, the highest point along the reaction path i.e. the initial gas-phase energy, has been chosen in order to be able to show the result. This is the case for some of the halides that lies on the $E_{\mathrm{TS}} = 0$ in the upper panel of figure 3.9. For the reactive surfaces, it makes no difference in the activity whether, no barrier or a barrier with a negative energy respect to gas-phase, is found.

In the lower panel of figure 3.9 BEP lines are shown for dissociation of hydrogen containing molecules. Although, the reaction occur over different sites and the transition states are completely different in geometry, the trend is the same as for the reactions over two cus sites. Also perovskite

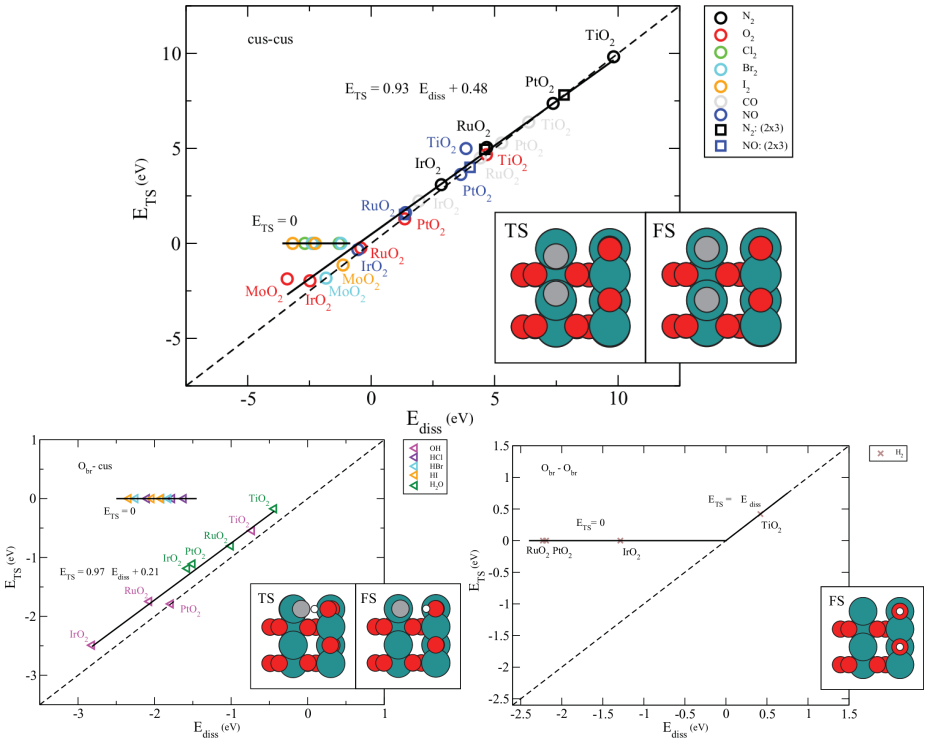

Figure 3.9: Calculated transition state energy as a function of dissociative chemisorption energy of diatomic molecules on rutile (110) surfaces. The solid black line is a fit to the data points and the dashed line indicate the dissociation line ($E_{\mathrm{TS}} = E_{\mathrm{diss}}$). Each plot represents one type of dissociation site, and a representative example of transition and final state structures is shown by the plot. The blue, red, gray and white spheres represent metal, oxygen, adsorbate and hydrogen atoms, respectively.

surfaces have been investigated in [Paper II]. The BEP lines in this case does not show as clear a trend as in the case of the rutiles. For very noble surfaces, however, the points fall precisely on the dissociation line. For less noble surfaces they deviate from the line such that the BEP lines for these points resembles the BEP line for stepped transition metal surfaces.

In [Paper III] we show that for dehydrogenation over transition metal surfaces a slightly different kind of universal transition state scaling applies besides the BEP relation described above. The analysis in the paper include different transition state energies for 249 dehydrogenation reactions of small hydrogen containing molecules over close-packed surfaces, stepped surfaces and nano-particles. The reactions include dehydrogenation steps of CH_4, NH_3, H_2O, C_2H_6, C_3H_8 and H_2O_2. In figure 3.10 the transition state energies of the dehydrogenation processes are plotted against the dehydrogenation energy. In this plot contrary to the other BEP relations shown in this section, the reference energies of all the energies are the gas-phase energies of CH_4, NH_3, H_2O and H_2 and not the gas-phase of the reactant. It turns out that all points lie on a single line with an acceptable mean average error (MAE) of 0.28 eV. When looking into a certain reaction or series of similar reactions the corresponding MAE is smaller. However, the main average transition state scaling is certainly good enough for a first approximation of the activation energy. Furthermore, there is no clear distinction between the different surface geometries as were the case for dissociation of diatomic molecules. This is because the transition state for hydrogenation on close-packed and stepped surfaces are very similar. Combined with another recent established universal BEP relation for C-C, C-O, C-N, N-O, N-N, and C-O dissociation of small hydrogen containing molecules over stepped transition metal surfaces [18], our results allow for a fast approximation of a the kinetics of large number of chemical reactions over a wide range of transition metal surfaces.

3.2.1 Sabatier principle and volcano curves

One of the implications of BEP relations is the concept of the optimal catalyst established by Sabatier [63]. He stated that if a very reactive surface would be used as a catalyst the catalytic activity would be limited by the slow desorption of the product molecules from the surface. On the other hand, if a more noble surface is used the activity will be limited by the activation barrier for the dissociation of the reactant. This means that

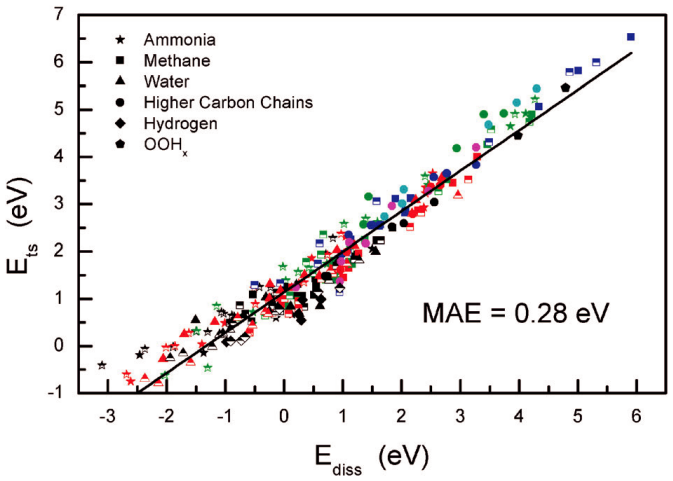

Figure 3.10: Transition state energies for dehydrogenation of different C, N and O containing molecules over transition metal surfaces plotted against the dissociation energy with respect to energies of the gas-phase molecules CH_4, NH_3, H_2O and H_2. The fully filled symbols refer to dissociation over close-packed surfaces, and the half-filled symbols refer to dissociation over stepped surfaces and OOH_x species have been dissociated on a M12 nanocluster. The colors represent the different hydrogen content in the molecules, where black is the first dehydrogenation step, red is the second step, green is the third step, and blue is the fourth dehydrogenation step.

the perfect catalyst is a compromise between the two. The optimal catalyst is therefore one that is sufficiently reactive to dissociate the reactant, and still bind the product very weakly. Applying this principle to BEP lines will result in a so called Sabatier volcano like the one shown in figure 3.11, where the catalytic activity is a function of the dissociative chemisorption energy of the reactant.

This means that for a specific BEP line there is limit to how good a catalyst we can obtain, because the dissociation energy is to a large extent confined to lie on the BEP line. Therefore it can be difficult to improve upon an already good catalyst. It will not help to find a similar material with a lower activation barrier for the process. The catalyst will then most likely bind the product equivalently stronger. The only way to make a substantially better catalyst is to move to a new and lower BEP line, which means changing the transition state geometry. The dashed lines in figure 3.11 correspond to a lower lying BEP line. Therefore, the rutile oxides with their BEP line almost equal to the dissociation line are extremely interesting as catalysts for reactions including dissociation of diatomic molecules. We have already seen that moving from close-packed to stepped-surface and further to rutile oxide surfaces stabilizes the transition state energy compared to dissociative chemisorption energy and thereby moves the line down, and enables the discovery of a potentially more active catalyst.

Due to the scaling relations between adsorption energies of different adsorbates explained in section 3.1 the volcano curve can also be applied for more complex reactions with a number of elementary steps. In this way a chemical reaction with a number of intermediates over a wide range of catalysts can often be described by one or two descriptors, which are often adsorption energies of the intermediates.

3.3 Summary

Various results regarding linear energy relations have been presented in this chapter. It has been shown that scaling relations also apply to compound surfaces, and that the physics of adsorption on these surfaces must be essentially the same as described by the *d*-band model for adsorption on transition metal surfaces. Furthermore, it has been established that oxides and in particular rutiles are a very interesting class of materials in the

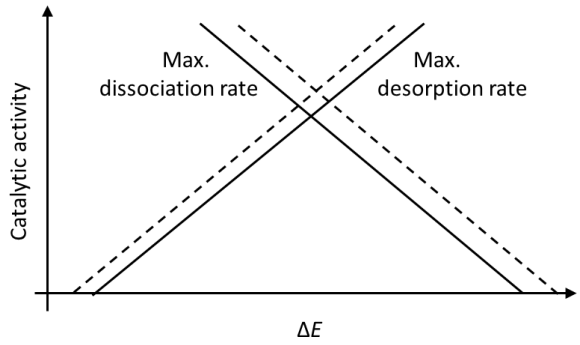

Figure 3.11: Schematic representation of a Sabatier volcano. The catalytic activity as a function of e.g. a reaction energy. The dashed lines correspond to lower lying BEP lines.

sense of heterogeneous catalysis. This has been done by showing that they essentially have no activation barrier for dissociation reactions for the interesting catalysts with dissociative chemisorption energies just below zero. Finally, a very universal transition state scaling relation has been found for dehydrogenation of small molecules.

Chapter 4

From energy scaling to reaction rates

From the scaling and BEP relations in chapter 3 it is possible to build micro-kinetic models showing trends in catalytic reactivity. In chapter 5 linear relations are used to analyze the trends of the oxidation process of HCl, HBr and HI over rutile oxide surfaces. Two different micro-kinetic methods are used to examine the rate and coverage of the surface species. First the steady state solution is found numerically and afterwords the resent developed analytical Sabatier-Gibbs analysis is employed. In this chapter, these two methods are presented and evaluated by applying them to a simple model reaction.

However, first we will go through some thermodynamic corrections. These are necessary in order to convert the potential energies from the energy scalings into free energies and reaction rates. Included in this is a discussion of how to apply these corrections to the transition state energies. This is followed by a small analysis on how small errors in DFT energies influences the calculated reaction rates.

In this chapter we will use the following simple reaction as an example

$$A_2 + 2B \rightleftharpoons 2AB \tag{4.1}$$

which includes the dissociation of a diatomic molecule, A_2, and the recombination of the product molecule AB. It is assumed that the reaction can be divided into the following two elementary reaction steps:

$$1) \quad A_2 + 2^* \rightleftharpoons 2A^* \tag{4.2}$$

$$2) \quad A^* + B \rightleftharpoons AB + * \tag{4.3}$$

where an asterisk, *, represents an active surface site and A* is A adsorbed at this site. In the first, step A_2 dissociates at the same time as it adsorbs on the surface and in the second step the adsorbed A atom reacts with the gas-phase reactant B and the product AB desorbs directly into the gas-phase.

4.1 Thermodynamic corrections

The Gibbs free energy of a gas-phase molecule can be calculated using standard formula for a classical ideal gas

$$G_{\text{gas}} = E_{\text{gas}} + \Delta H_{\text{gas}}^{0,T} - TS_{\text{gas}} \tag{4.4}$$

where the energy E_{gas} is the value calculated with DFT including the zero-point correction (equation (2.9)). $\Delta H_{\text{gas}}^{0,T}$ is the change in enthalpy when raising the temperature from 0 K to T and S_{gas} is the entropy at temperature T. The standard values for entropy will be used, as changes with temperature are negligible. Both the change in enthalpy and the entropy of gas-phase molecules can be obtained from standard tabulated values [64, 65].

When a species is adsorbed at a surface the pressure term of the enthalpy vanishes such that the enthalpy term of the free energy in (4.4) is substituted by the internal energy $\Delta U_{\text{ads}}^{0,T}$. The free energy of a surface species can then be calculated as

$$G_{\text{ads}} = E_{\text{ads}} + \Delta U_{\text{ads}}^{0,T} - TS_{\text{ads}}^{\text{vib}} \tag{4.5}$$

where the DFT energy, E_{ads}, of the adsorbate is calculated as the energy of the system with the adsorbate and the surface minus the energy of the clean surface ($E_{\text{ads}} = E(\text{ads} + \text{surf}) - E(\text{surf})$). As the species is adsorbed the rotational degrees of freedom are converted into vibrations at the surface, and consequently the change in internal energy, $\Delta U_{\text{vib}}^{0,T}$, and the entropy term TS_{ads} only include vibrational components. In the harmonic approximation these terms are given by

$$TS_{\text{ads}}^{T} = \sum_i \frac{h\nu_i}{e^{h\nu_i/(k_{\text{B}}T)} - 1} - k_{\text{B}}T \sum_i \ln(1 - e^{h\nu_i/(k_{\text{B}}T)}) \tag{4.6}$$

and

$$U_{\text{ads}}^{0,T} = \sum_i \frac{h\nu_i}{e^{h\nu_i/(k_{\text{B}}T)} - 1} \tag{4.7}$$

where h is Planck's constant and the i vibrational frequencies, ν_i, are found in harmonic approximation by displacement of the atoms.

One should be cautious when calculating the entropy and internal energies, using the harmonic approximation, especially if very low modes are present. These give very large contributions to the total values and therefore often lead to incorrect results. Therefore, and because of their small values the entropy and change in internal energies of surface species are often neglected [19, 8]. However, at higher temperatures these terms become significant and leaving them out will undoubtedly be a source of error [66]. Furthermore, a part of these erroneous contributions is reduced as the first term of entropy is canceled by the internal energy leaving only the logarithmic part of the entropy term.

From 4.4 and 4.5 we can now calculate the free energy ΔG_i of a reaction, which in case of reaction step 1) equation (4.2) is

$$\begin{aligned}\Delta G_1 &= 2G_{\text{A}*} - G_{\text{A}_2} \\ &= 2E_{\text{A}*} + 2\Delta U_{\text{A}*}^{0,T} - 2TS_{\text{A}*}^{\text{vib}} - E_{\text{A}_2} - \Delta H_{\text{A}_2}^{0,T} + TS_{\text{A}_2}^{T}\end{aligned} \tag{4.8}$$

and in general it becomes

$$\Delta G_i = \Delta E_i + \Delta H_i - T\Delta S_i \tag{4.9}$$

Here i refers to the reaction step number and K_i is the equilibrium constant of reaction step i. k_{B} is Boltzman's constant.

4.1.1 The transition state barrier

The forward rate r_i of reaction step i is proportional to the reaction constant k_i given by

$$r_i \propto k_i = \frac{k_{\text{B}}T}{h} e^{\frac{-\Delta G_i^{\text{a}}}{k_{\text{B}}T}} \tag{4.10}$$

where ΔG_i^{a} is the free energy activation barrier. The relation to the equilibrium constant is

$$\frac{k_i}{k_{-i}} = K_i = e^{\frac{-\Delta G_i}{k_{\text{B}}T}} \tag{4.11}$$

where k_{-i} is the rate constant for the backward rate. The activation barriers are usually found using transition state theory where it is assumed that an activated complex exists at the transition state on top of the energy barrier in a saddle point on the potential energy surface. The activation barrier ΔG_1^{a} of reaction step 1) from previous section will in this case be given by

$$\begin{aligned}\Delta G_1^{\mathrm{a}} &= G^{\ddagger} - G_{\mathrm{A}_2} \\ &= E^{\ddagger} + \Delta U^{\ddagger 0,T} - TS^{\ddagger \mathrm{vib}} - E_{\mathrm{A}_2} - \Delta H_{\mathrm{A}_2}^{0,T} + TS_{\mathrm{A}_2}^{T}\end{aligned} \tag{4.12}$$

where the ‡ notation refers to the values of the activated complex. In general this is

$$\Delta G_i^{\mathrm{a}} = \Delta E_i^{\mathrm{a}} + \Delta H_i^{\mathrm{a}} - T\Delta S_i^{\mathrm{a}} \tag{4.13}$$

The activated complex can be found by searching through the reaction coordinate in small steps. The two most widely use methods are the nudged elastic band method [52, **?**] or as employed in [Paper II] and [Paper III] fixed bong length method. When the transition state is found a vibrational analysis of the activated complex can be carried out and the entropy and change in internal energy can be calculated using equation (4.6) and (4.7).

Sometimes, especially for dissociative adsorption on oxides, the reactions do not go through a saddle point, but are decreasing in potential energy all the way from reactant to product. This is illustrated as the dashed line denoted by E in figure 4.1. In these cases it is not obvious what the value of ΔG_i^{a} in (4.10) should be. For an exothermic reaction step without a barrier the transition state value $E^{\ddagger}$ is usually set equal to the potential energy of the reactants, i.e. $\Delta E_i^{\mathrm{a}} = 0$ for $\Delta E_i < 0$. In order to use transition state theory, we need to choose transition-state values for ΔH^{a} and ΔS^{a}. We do, however, not know how and where along the reaction path the vibrational modes are changed.

One possible solution is to set $\Delta G_i^{\mathrm{a}} = 0$ for $\Delta G_i < 0$. However, having an activation barrier of 0 eV will at standard conditions result in a turnover frequency (TOF) of $k_{\mathrm{B}}T/h = 6.2 \cdot 10^{12}\mathrm{s}^{-1}$ per surface site. This is much higher than the flux F to the surface, which at the same conditions is of the order of 10^8 s^{-1}. This leads us to another way of defining the transition state values, which is to choose the value of ΔG^{a} to be the one corresponding to $k_i = F$. This must be the lowest possible value ΔG^{a} can take.

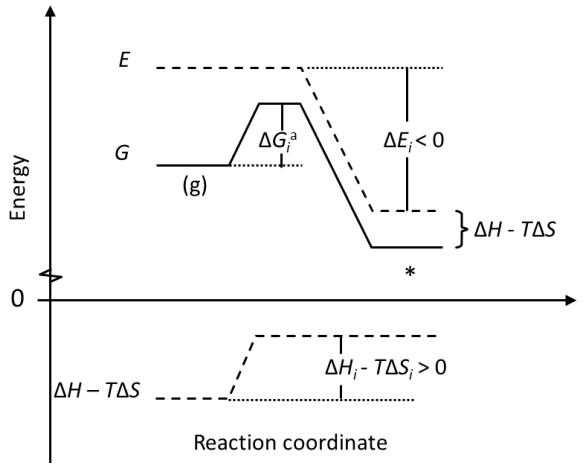

Figure 4.1: Energy diagram of an adsorption reaction, with an effective activation barrier found by using equation (4.14) and (4.16).

A reaction constant equal to the flux would still in many cases result in unreasonable high reaction rates. The highest possible value ΔG^{a} can take is given by the following equations.

$$\Delta E_i^{\mathrm{a}} = 0 \quad \text{for} \quad \Delta E_i < 0 \quad \text{and} \quad \Delta E_i^{\mathrm{a}} = \Delta E_i \quad \text{for} \quad \Delta E_i > 0 \tag{4.14}$$

and

$$\begin{aligned} &\Delta H_i^{\mathrm{a}} - T\Delta S_i^{\mathrm{a}} = 0 \quad \text{for} \quad \Delta H_i - T\Delta S_i < 0 \quad \text{and} \\ &\Delta H_i^{\mathrm{a}} - T\Delta S_i^{\mathrm{a}} = \Delta H_i - T\Delta S_i \quad \text{for} \quad \Delta H_i - T\Delta S_i > 0 \end{aligned} \tag{4.15}$$

An example of this is shown in figure 4.1 as a free energy diagram of an adsorption process. This method is employed in chapter **??** for the oxidation process of hydrogen halides.

In summary, we have an upper and a lower boundary for the effective activation barrier of an exothermic elementary reaction with no transition state saddle point. It would be reasonable to believe that the value of the "true" effective barrier is somewhere in between the two. This could be investigated in each case of reaction by performing vibrational analyses for complexes along the reaction path.

4.2 Micro-kinetic methods

For well studied chemical reactions it is often well known which one or two reaction steps are rate determining for the best catalysts. In this case an analytical solution can often be found for rate equations in steady state by assuming that the other reaction steps are in equilibrium. In other cases it is not obvious which steps are rate determining and it can be necessary to find the exact solution to the rate equation numerically, e.g. when the reaction is complex and includes many competing elementary reaction steps.

Finding a numerical solution is, however, not always straight forward. If a single or few catalysts are to be investigated, it is doable. On the other hand, in chapter 4 we found that a few parameters, such as the adsorption energy of specific species, can describe the activity of a range of catalysts. If we would like to investigate these parameters systematically, we would have to solve the rate equations for a large number of theoretical catalysts. Furthermore, without analytical expressions, we cannot get the insight we need to get a good understanding of the complex reaction mechanisms. Choosing rate determining reaction steps in order to reach an analytical solution can, however be problematic, because as we vary the parameters the steps which are determining the over all rate will also change. Therefore, the Sabatier [17, 19] and Sabatier-Gibbs analysis presented [67, 68] in this section are useful analytical tools.

With the Sabatier analysis it is very simple and fast to get a qualitative overview of the reaction mechanisms. Furthermore, it gives an exact upper bound to the reaction rate. This means that it can give an indication of where the model with predeterment rate determining steps breaks down. The Sabatier-Gibbs analysis, which also gives an upper bound to the rate, is a little more complex, but in change gives considerably improved results.

The simple model reaction (4.1) from previously, with the two elementary reaction steps 1) (4.2) and 2) (4.3) will be used to present the different methods.

The rates of reaction step 1) and 2) can be written as

$$r_1 = k_1 p_{\mathrm{A}_2} \theta_*^2 - k_{-1} \theta_{\mathrm{A}}^2 \tag{4.16}$$

$$r_2 = k_2 p_{\mathrm{B}} \theta_{\mathrm{A}} - k_{-2} p_{\mathrm{AB}} \theta_* \tag{4.17}$$

where p_{A_2}, p_{B} and p_{AB} are dimensionless partial pressures of the gas-phase molecules. θ_A and θ_* are the surface coverage of A and the fraction of

free sites, respectively. The mean-field approximation is used, where it is assumed that the surface species are distributed randomly over the surface. The reaction constants k_i and k_{-i} are given in (4.10) and (4.11).

4.2.1 Numerical steady state solution

One way to find the exact steady state solution to the rate equation is to set up differential equations describing the change in coverage of all species over time. For the simple model reaction above this would result in a single equation

$$\frac{d\theta_{\mathrm{A}}}{dt} = 2r_1 - r_2 \tag{4.18}$$

plus the following criteria for the coverage

$$\theta_{\mathrm{A}} + \theta_* = 1 \tag{4.19}$$

$$0 \leq \theta_{\mathrm{A}} \leq 1 \quad \text{and} \quad 0 \leq \theta_* \leq 1 \tag{4.20}$$

In implementing this, it can be useful to apply the following transformation

$$a_{\mathrm{X}} = \sqrt{\theta_{\mathrm{X}}}, \quad (\mathrm{X} = \mathrm{A}, *) \tag{4.21}$$

After choosing realistic initial values for the coverage the equation is then integrated in time until steady state is obtained. These differential equations are, however, often problematic to solve. The coverages can vary rapidly in time, which easily leads to instability, and since we are usually only interested in the solution at steady state $\frac{d\theta_{\mathrm{A}}}{dt} = 0$ we can use a root finder method to solve following set of equations

$$2r_1 = r_2 \quad \text{and} \quad \theta_{\mathrm{A}} + \theta_* = 1 \tag{4.22}$$

where (4.20) still applies. However, numerical problems still exists. The different parameters in the equations often differ by many orders of magnitude, which makes the usual computer accuracy insufficient. Additionally, the complexity of the set of equations grows rapidly with the number of elementary steps, and it is becomes difficult, but extremely important to find a good initial guess.

In chapter 5, a numerical solution to large range of parameters for the catalytic oxidation reaction of hydrogen halides was found solving a set of steady state equations equivalent to (4.22). The highest rate of success in

finding a solution, was obtained when the initial guess was found by solving the system of differential equations in a short period of time. Additionally it was necessary increase the computer accuracy from the usual 16 to 80 significant digits. Also patience and a little bit of good luck seemed to be useful.

4.2.2 Sabatier analysis

The model here referred to as Sabatier analysis [17] is a micro-kinetic tool inspired by the Sabatier principle explained in the previous chapter. The energy barriers are all calculated from BEP relations and the surface coverage of each species is assumed to be optimal. Even though the reaction kinetics in this model are simplified considerably, the overall trends in catalytic activity are recovered impressively well.

We are assuming net forward rates for each elementary reaction step, i.e. $r_i \geq 0$ and $\Delta G_i^{\text{tot}} \leq 0$, where ΔG_i^{tot} is the total change in free energy of the entire system upon reaction step i. For our little model reaction this results in following bounds on the chemical potential $\mu_{\text{A}*}$ of intermediate A*

$$\Delta G_1^{\text{tot}} = 2\mu_{\text{A}*} - \mu_{\text{A}_2} \leq 0 \quad \Leftrightarrow \quad 2\mu_{\text{A}*} \leq \mu_{\text{A}_2} \tag{4.23}$$

$$\Delta G_2^{\text{tot}} =\leq 0 \quad \Leftrightarrow \quad \mu_{\text{AB}} - \mu_{\text{B}} \leq \mu_{\text{A}*} \tag{4.24}$$

This applies in general. The chemical potentials of the intermediates of a reaction are limited by the chemical potentials of the reactant and product molecules. Since $\mu_{\text{A}_2} = \mu^0_{\text{A}_2} - k_{\text{B}}T\ln(p_{\text{A}_2})$ and $\mu_{\text{A}*} = \mu^0_{\text{A}*} - k_{\text{B}}T\ln\left(\theta_{\text{A}}/\theta_*\right)$ where μ^0_{X} is the standard chemical potential of species X, equation (4.23) and (4.24) can be rewritten into

$$\Delta G_1 + k_{\text{B}}T\ln\left(\frac{\theta_{\text{A}}^2}{p_{\text{A}_2}\theta_*^2}\right) \leq 0 \quad \Leftrightarrow \quad \frac{\theta_{\text{A}}^2}{p_{\text{A}_2}\theta_*^2} \leq e^{\frac{-\Delta G_1}{k_{\text{B}}T}} = K_1 \tag{4.25}$$

$$\Delta G_2 + k_{\text{B}}T\ln\left(\frac{p_{\text{AB}}\theta_*}{p_{\text{B}}\theta_{\text{A}}}\right) \leq 0 \quad \Leftrightarrow \quad \frac{p_{\text{AB}}\theta_*}{p_{\text{B}}\theta_{\text{A}}} \leq e^{\frac{-\Delta G_2}{k_{\text{B}}T}} = K_2 \tag{4.26}$$

and further into

$$1 \geq= \frac{\theta_{\text{A}}^2}{K_1 p_{\text{A}_2}\theta_*^2} = \gamma_1 \quad \text{and} \quad 1 \geq \frac{p_{\text{AB}}\theta_*}{K_2 p_{\text{B}}\theta_{\text{A}}} = \gamma_2 \tag{4.27}$$

where we have introduced the approach to equilibrium γ_i. The rate equations (4.16) and (4.17) can know be written as

$$r_1 = 2k_1 p_{\mathrm{A}_2} \theta_*^2 (1 - \gamma_1) \tag{4.28}$$

$$r_2 = k_2 p_{\mathrm{B}} \theta_{\mathrm{A}} (1 - \gamma_2) \tag{4.29}$$

γ_i is, as the name reveals, a measure for how far reaction step i is from equilibrium. For $\gamma_i = 1$ the reaction step is in equilibrium and for low values of γ_i the reaction step is far from equilibrium. An upper bound to r_i is obtained for $\gamma_i = 0$. We get a more strict upper bound, however, from following relation for the approach to equilibrium for the overall reaction

$$\gamma = \gamma_1 \gamma_2^2 = \frac{p_{\mathrm{AB}}^2}{K_1 K_2^2 p_{\mathrm{A}_2} p_{\mathrm{B}}^2}, \quad 0 \leq \gamma \leq 1 \tag{4.30}$$

In general this is

$$\gamma = \prod_i \gamma_i^{n_i} \tag{4.31}$$

where n_i is the stoichiometric coefficient for reaction step i. This means that $\gamma_i^{n_i}$ cannot be lower than the overall approach to equilibrium γ

$$0 \leq \gamma \leq \gamma_i^{n_i} \leq 1 \tag{4.32}$$

For each elementary reaction step we can now write the optimal reaction rate within the framework of the Sabatier analysis. For the first elementary reaction step this is obtained when setting $\gamma_1 = \gamma$ and $\theta_* = 1$:

$$r_1^{\max} = 2k_1 p_{\mathrm{A}_2} (1 - \gamma) \tag{4.33}$$

The Sabatier rate for the second elementary reaction step can be found by the same means. $\gamma_2 = \sqrt{\gamma}$ and $\theta_{\mathrm{A}} = 1$:

$$r_2^{\max} = 2k_2 p_{\mathrm{B}} (1 - \sqrt{\gamma}) \tag{4.34}$$

The overall Sabatier reaction rate is bound by the lower of $r_1^{\max}$ and $r_2^{\max}$.

$$R_{\mathrm{Sabatier}} = \min \{r_1^{\max}, r_2^{\max}\} \tag{4.35}$$

An example is given in section 4.2.4.

4.2.3 Sabatier-Gibbs analysis

As Sabatier analysis is based on optimal coverages for the forward rate of each elementary reaction it fails quantitatively in cases where coverage of a species is much smaller than optimal. The Sabatier-Gibbs analysis is improving this by introducing stricter upper bounds to the coverages of the forward reactions rates. Since γ_i are functions of coverages, the constraints on γ_i equation (4.32) can be used in finding maximum values for the different coverages.

It is convenient to introduce the coverage activities of surface species A $\lambda_{\mathrm{A}} = \theta_{\mathrm{A}}/\theta_*$. Then γ_1 from equation (4.27) can be written as

$$\gamma_1 = \frac{\theta_{\mathrm{A}}^2}{K_1 p_{\mathrm{A}_2} \theta_*^2} = \frac{\lambda_{\mathrm{A}}^2}{K_1 p_{\mathrm{A}_2}} \tag{4.36}$$

and by using that $\gamma \leq \gamma_1 \leq 1$, an upper and lower boundary of λ_A can be found

$$\lambda_{\mathrm{A}}^{\min} = \sqrt{\gamma p_{\mathrm{A}_2} K_1} \quad \text{and} \quad \lambda_{\mathrm{A}}^{\max} = \sqrt{p_{\mathrm{A}_2} K_1} \tag{4.37}$$

From the site conservation $\theta_* + \theta_{\mathrm{A}}$ we can find the maximum fraction of free sites

$$\theta_*^{\max} = \frac{1}{\lambda_{\mathrm{A}}^{\min} + 1} \tag{4.38}$$

and the maximum coverage of species A

$$\theta_{\mathrm{A}}^{\max} = \frac{\lambda_{\mathrm{A}}^{\max}}{\lambda_{\mathrm{A}}^{\max} + 1} \tag{4.39}$$

The net forward rate of the two elementary reactions can then be found as for the Sabatier analysis. However, here the θ_{A} and θ_* are substituted by (4.40) and (4.41).

$$r_1^{\max} = 2k_1 p_{\mathrm{A}_2} \theta_*^{\max} (1 - \gamma) \tag{4.40}$$

$$r_2^{\max} = k_2 p_{\mathrm{B}} \theta_{\mathrm{A}}^{\max} (1 - \sqrt{\gamma}) \tag{4.41}$$

The overall Sabatier-Gibbs rate of the model system is

$$R_{\mathrm{SG}} = \min \{r_1^{\max}, r_2^{\max})\} \tag{4.42}$$

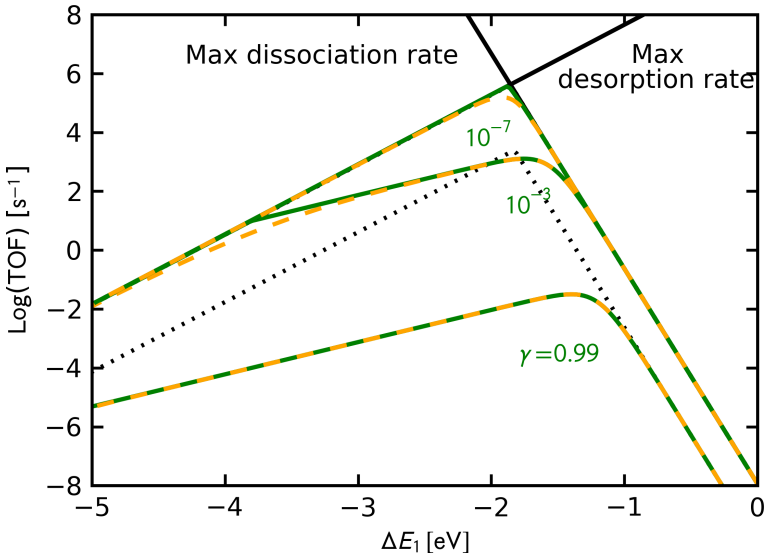

Figure 4.2: Turnover frequencies (TOF) for the model system described in the previous sections for varies values of γ. The magenta dashed line is the exact numerical solution, the green line is the Sabatier-Gibbs rates and the dotted line is the Sabatier solution at $\gamma = 0.99$. The Sabatier lines for $\gamma = 10^{-3}$ and $\gamma = 10^{-7}$ are not distinguishable from the lines for maximal dissociation and desorption.

4.2.4 Volcano curves

In this section turnover frequencies (TOF) are determined for our simple model reaction (4.2) and (4.3). This is done by employing both the Sabatier and the Sabatier-Gibbs analyses and by finding the steady state solution numerically. The performance of the two simple approximations can the be compared with the exact solution. The results are shown in figure 4.2 for different values of γ.

In order to calculate the rate and equilibrium constants we have to make some further assumptions. First of all, the activation barrier are calculated using the universal BEP relation from section 3.2 for dissociative adsorption of diatomic molecules on transition metal surfaces. The gas-phase entropy of A_2 is set to 0.002 eV, which is close to the value of many diatomic molecules [65]. The entropy of the product AB is assumed to be equal to the entropy of reactant B and the changes in enthalpy and the entropy of

surface species A is neglected. The exact numbers are not important in order to compare the performances of the different models.

For $\gamma \to 0$ far from equilibrium the Sabatier volcano is in good agreement with the numerical solution. Only in the small range at the top where neither of the coverages, θ_* and θ_A are optimal the Sabatier volcano deviates a little. However when the reaction approaches equilibrium, for $\gamma \to 1$, the TOF calculated with the Sabatier analysis differs by many orders of magnitude. Qualitatively, however, the two volcanoes are still in good agreement. For the more noble surface to the right in the figure reaction step 1) is strongly rate limiting, $\gamma_1 \approx \gamma$ and the Sabatier analysis is exact in that limit. For the very reactive surfaces the opposite applies.

From (4.37) we see that the Sabatier-Gibbs analysis is exact for $\gamma \to 1$, which figure 4.2 also indicates, but also for all other values of γ the Sabatier-Gibbs analysis performs surprisingly well for this simple system. For more complex reactions with more elementary steps and more intermediate surface species the Sabatier-Gibbs analysis cannot be expected to perform equally well. Moreover, for more complex systems the analytical derivation gets considerably more complex compare to the Sabatier analysis. In chapter 5 the Sabatier-Gibbs analysis is tested on a more complex catalytic reaction, namely the oxidation of hydrogen-halides on rutile oxides.

In general, the small changes applied in the Sabatier-Gibbs analysis compared to the Sabatier description improves the performance considerably. However, even though the precision of the Sabatier-Gibbs analysis by far exceeds the one of the Sabatier analysis, the Sabatier analysis has a great advantage in its simplicity.

4.3 Sensitivity analysis

The standard error of an adsorption energy in calculated in DFT is approximately 0.2 eV. In this section, a simple analysis is given, of how precise we can expect to be able to valuate the rate of a given reaction taking this error in DFT into account. First, we will apply an error to an energy barrier in order to estimate the influence on the onset temperature for a reaction, i.e. the lowest temperature at which the products of the reaction can be measured.

We consider a reaction where the association of a diatomic molecule is

rate determining.

$$2\mathrm{A}^* \rightarrow \mathrm{A}_2 + 2^*$$

This is the case of the oxidation process of HCl over RuO_2 (A=Cl). See chapter 5. Furthermore, we assume and that the coverage of species A, θ_A, is constant and equal to one. Then the rate then becomes

$$r = \frac{k_\mathrm{B}T}{h} e^{\frac{-\Delta E^\mathrm{a}}{k_\mathrm{B}T}} = \frac{k_\mathrm{B}T}{h} e^{\frac{-2\Delta E^\mathrm{A}_\mathrm{ads}}{k_\mathrm{B}T}} \tag{4.43}$$

where $\Delta E^\mathrm{a} = \Delta E^{\mathrm{A}_2}_\mathrm{diss} = 2\Delta E^\mathrm{A}_\mathrm{ads} > 0$ is the effective energy barrier and $\Delta E^\mathrm{A}_\mathrm{ads}$ is the adsorption energy of A. As in the cases described in section 4.1.1 there is no additional transition state barrier.

Applying an error δ to the effective barrier results in a shift in onset temperature ΔT and the following expression is valid.

$$r = \frac{k_\mathrm{B}T}{h} e^{\frac{-\Delta E^\mathrm{a}}{k_\mathrm{B}T}} = \frac{k_\mathrm{B}T}{h} e^{\frac{-\Delta E^\mathrm{a}+\delta}{k_\mathrm{B}(T+\Delta T)}} \tag{4.44}$$

We get

$$\Delta T = \frac{\delta T}{\Delta E} \tag{4.45}$$

Shifting $\Delta E^\mathrm{A}_\mathrm{ads}$ by -0.2 eV from -0.65 eV ($\Delta E^\mathrm{Cl}_\mathrm{ads}$ on RuO_2) to -0.85 eV, i.e. $\delta = 0.4$ eV, and choosing $T = 473$ K (approximate onset temperature of the oxidation process of HCl over RuO_2), we get a shift $\Delta T = 146$ K in temperature. Note that for lower barriers or higher temperatures this shift will be even larger.

Similarly the sensitivity of the reaction rate can be estimated by

$$\frac{k_\mathrm{B}T}{h} e^{\frac{-(\Delta E+\delta)}{k_\mathrm{B}T}} = r e^{\frac{-\delta}{k_\mathrm{B}T}} \tag{4.46}$$

which means that if we apply an error, δ, to the effective barrier the rate will change with a factor of $e^{-\delta/(kT)}$. If we set $\delta = 0.4$ eV and $T = 573$ K (the temperature at which the volcano plots in chapter 5 are calculated) this factor is as much as 3.0×10^{-4}.

Chapter 5

Oxidation of hydrogen halides

In this chapter the tools explained in the previous chapters have been employed in order to investigate the heterogeneous catalytic oxidation of hydrogen halide (HCl, HBr and HI) over rutile oxide (110) surfaces. The chapter is based on the results presented in [Paper IV], where an analysis of the the reactions are given based on a numerical solution to a micro-kinetic model. Furthermore, an analytical analysis is given based on the newly developed Sabatier-Gibbs analysis. This is done in order to contribute to the understanding of the reaction mechanisms and equally important to validate our new micro-kinetic tool the Sabatier-Gibbs analysis. The reactions considered are the following.

$$4HCl + O_2 \rightleftharpoons 2Cl_2 + 2H_2O \tag{5.1}$$

$$4HBr + O_2 \rightleftharpoons 2Br_2 + 2H_2O \tag{5.2}$$

$$4HI + O_2 \rightleftharpoons 2I_2 + 2H_2O \tag{5.3}$$

5.1 The rutile (110) surface

The rutile (110) surface have presented shortly previously in chapter 3, where they where found be to promising as catalyst. Actually, RuO_2 have recently been shown experimentally to be a good oxidation catalyst in general [20] and also (supported on TiO_2) specifically for the Deacon process equation (5.1) [25].

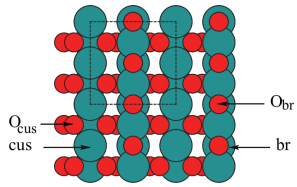

Figure 5.1: Schematic view of the (110) rutile surface. Blue and red spheres represents transition metal and oxygen atoms, respectively.

The chemistry on the rutile oxide (110) surfaces is primarily taking place on the coordinative unsaturated (cus) sites. These cus sites are situated between rows of oxygen atoms that are strongly bound at the bridge sites between two metal atoms (see figure 5.1). Experimental and theoretical work on the RuO_2 surface shows that under reaction conditions of the Deacon process most of these bridging oxygen atoms will be replaced by chlorine [8, 28, 29]. Bridging oxygen atoms of TiO_2 and IrO_2 surfaces on the other hand are not predicted to be replaced [8]. Similar calculations predict that RuO_2 and PtO_2 exposed to HBr and HI will have the bridging oxygen atoms replaced by Br and I, respectively. Phase diagrams are shown in supplementary materials to [Paper IV].

Replacing bridged oxygen by halides has been shown to have a rather small effect to adsorption energies on cus sites in the case of chlorine [8] and we assume that the same is true for bromine and iodine. We therefore limit this first analysis to surfaces with oxygen in the bridge site only. Since bridge oxygen is very strong bound compared to adsorbates on cus sites the reaction is occurring along the cus sites only.

5.2 The micro-kinetic model

In our micro-kinetic model we are assuming that the oxidation reactions of hydrogen halides reaction (5.1) to (5.3) can be divided into following elementary reaction steps, where X=Cl, Br or I.

$$\text{(R1)} \quad O_2 + 2* \rightleftharpoons O_2** \tag{5.4}$$

$$\text{(R2)} \quad O_2** \rightleftharpoons 2O* \tag{5.5}$$

$$\text{(R3)} \quad O* + * + HX \rightleftharpoons OH* + X* \tag{5.6}$$

$$\text{(R4)} \quad 2\text{X}^* \rightleftharpoons 2^* + \text{X}_2 \tag{5.7}$$

$$\text{(R5)} \quad 2\text{OH}^* \rightleftharpoons \text{O}^* + ^* + \text{H}_2\text{O} \tag{5.8}$$

where * denotes an empty site on the surface and O_2** is refers to the fact that O_2 is covering two sites. The reaction rates for each elementary reaction step can be written as

$$r_1 = k_1 p_{\text{O}_2} \theta_*^2 - k_{-1} \theta_{\text{O}_2} = k_1 p_{\text{O}_2} \theta_*^2 (1 - \gamma_1) \tag{5.9}$$

$$r_2 = \frac{1}{2} k_2 \theta_{\text{O}_2} - k_{-2} \theta_{\text{O}}^2 = \frac{1}{2} k_2 \theta_{\text{O}_2} (1 - \gamma_2) \tag{5.10}$$

$$r_3 = k_3 p_{\text{HX}} \theta_{\text{O}} \theta_* - k_{-3} \theta_{\text{OH}} \theta_{\text{X}} = k_3 p_{\text{HX}} \theta_{\text{O}} \theta_* (1 - \gamma_3) \tag{5.11}$$

$$r_4 = k_4 \theta_{\text{X}_2} - k_{-4} p_{\text{X}_2} \theta_*^2 = k_4 \theta_{\text{X}_2} (1 - \gamma_4) \tag{5.12}$$

$$r_5 = k_5 \theta_{\text{OH}}^2 - k_{-5} p_{\text{H}_2\text{O}} \theta_{\text{O}} \theta_* = k_5 \theta_{\text{OH}}^2 (1 - \gamma_5) \tag{5.13}$$

where p_{HX}, p_{O_2}, p_{X_2} and $p_{\text{H}_2\text{O}}$ are the partial pressures of the gas-phase species and θ_{O_2}, θ_{O}, θ_{OH} and θ_{X} are the coverages of the surface species and θ_* is the remaining fraction of free sites. The forward and backward rate constants k_i and k_{-i} are given by the equations (4.10) and (4.11) and the activation barriers are calculated as described in section 4.1.1.

In a recent study a similar analysis of the Deacon process was performed where reaction step 2) and 4) were chosen to be rate determining [8]. This assumption was made on the basis of the thermodynamics. In [Paper IV] we did not make any assumptions about rate determining step. The turnover frequencies in the first part of this chapter are found by solving following system of equations numerically as described in section 4.2.1.

$$r_1 = r_2, \quad r_2 = 4r_3, \quad 2r_3 = r_4, \quad r_4 = r_5 \tag{5.14}$$

and

$$\theta_{\text{O}_2} + \theta_{\text{O}} + \theta_{\text{OH}} + \theta_{\text{X}} + \theta_* = 1 \tag{5.15}$$

In the last part of the chapter a Sabatier-Gibbs analysis is performed. This kind of analysis is explained in section 4.2.3.

In our micro-kinetic analyses we are considering two coverage regimes. One, which simulates that halides cover 50% or less of the surface and

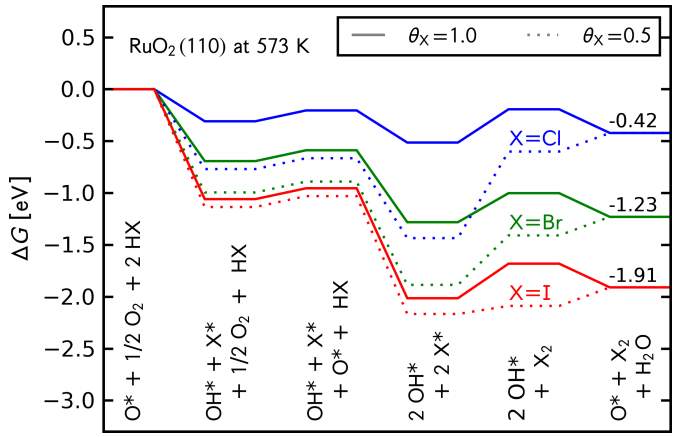

Figure 5.2: Gibbs free energy diagram for the oxidation of HCl, HBr, and HI on RuO2(110) at 573K as obtained from DFT calculations. Solid and dotted lines represent high and low coverages, respectively. X denotes a halide (Cl, Br, or I) and * denotes an adsorbed atom or molecule.

one simulating coverage of halides close to 100%. These correspond to two distinct models. The difference between the two model lies exclusively in the atomic configurations in the DFT calculations for the adsorption energies. In the high coverage model the adsorption energy of OH and X have been calculated by adsorbing them next to an X atom in a 2×1 unit cell. In the low coverage model OH and X are adsorbed next to a free in an equivalent unit cell. Both the energy of adsorbed oxygen atoms and the energy of adsorbed O_2 are calculated alone in the cell. The coverage of O_2 is thus equal to one as it covers two sites.

5.3 The RuO_2 catalyst

In figure 5.2 free energy diagrams are shown for the reactions over RuO_2 at 573 K. The Gibbs free energies are calculated as described in section 4.1. In the figure the energies for the high coverage model and for the low coverages model are shown as solid and dotted lines, respectively. As seen, the oxidation of the hydrogen halides becomes more exothermic from chlorine to bromine to iodine. The reaction cycle starts with the dissociative adsorption of the hydrogen halide on the cus site of an oxygen pre-covered

surface. Adsorption proceeds via dissociation of hydrogen halide where the hydrogen atom binds ontop the oxygen and the halide atom binds directly to the free cus site. The next step is the dissociative adsorption of O_2. After adsorption of a second hydrogen halide the two OH groups recombine to give H_2O and on adsorbed oxygen atom. The two adsorbed halide atom then recombine to Cl_2, Br_2 or I_2.

For HCl at 573 K, the recombination of two Cl atoms represents the most difficult step of the catalytic cycle. Moreover, it can be seen that this step is only feasible in the high coverage regime as recombination becomes prohibitively endothermic at low chlorine coverages, in agreement with earlier theoretical studies [8, 27]. Also for HBr this is the most energy demanding step in HBr oxidation at 573 K. As for HCl oxidation, this step is more facile at high coverages, though the difference to the low coverage regime is not as large. Interestingly, recombination of two iodine atoms to form I_2 is similarly uphill as the recombination of two Cl and two Br at high coverages. Recombination of two iodine atoms at low coverages on the other hand is only slightly endothermic by 0.08 eV. This is due to interactions between iodine atoms that increase overall iodine binding at high coverages. HI oxidation will thus be more active at low coverages whereas HCl and HBr oxidation will occur in the high coverage regime.

Figure 5.3 shows the turnover frequencies (TOF) as a function of temperature for both, for the high and low coverage regimes. Inspection of the figure what one would expect from the energetics shown in figure 5.2. As recombination of two halide to form either Cl_2, Br_2 or I_2 is very similar for all three processes at high coverages, their onset activities for X_2 production are also very similar. All three halides start the production around 500K. Similar results was found for HCl oxidation over $RuO_2(110)$ from theoretical [8] as well as experimental work [27]. The activity for chlorine and bromine in the low coverage regime, is much lower whereas a higher activity is predicted for iodine at low coverages in the same regime, i.e. I_2 production at low coverages is starting already around 400 K. The oxidation of HI is known to be a fast process compared to the Deacon process [69].

The sensitivity analysis in section 4.3 showed that applying an error of 0.2 eV to the adsorption energy of chlorine shifted the onset temperature calculated with our model by as much as 150 K. The rates given in figure 5.3 should therefore be considered with caution and we see this more as a trend study rather than being able to predict the magnitude of total rates.

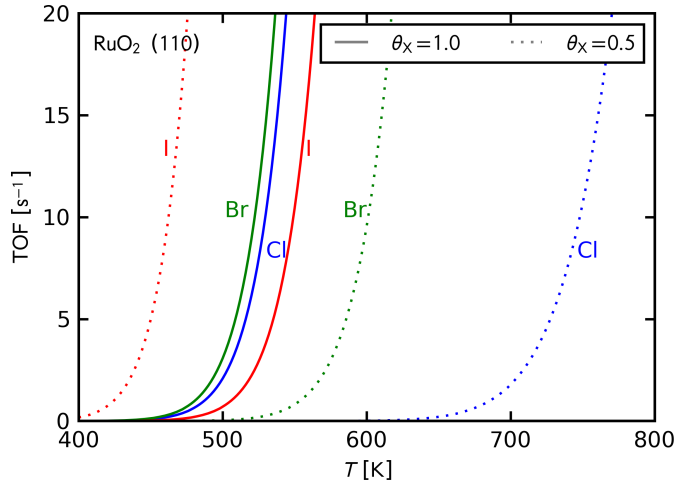

Figure 5.3: Turnover frequencies (TOFs) as a function of temperature for HCl, HBr, and HI oxidation over RuO_2(110) as obtained from the solvation of the microkinetic model described above. Results for high (solid lines) and low (dotted lines) coverages are shown.

5.4 Applying scaling relations

In order to extend this model to other rutile (110) surfaces, we applied scaling relations, which are explained in section 3.1. In general BEP relations (section 3.2) are also needed in order to estimate the activation barrier. However, as shown in section 3.2 the BEP lines for rutile (110) surfaces are equal to the dissociation line. Therefore, the activation energy can be calculated directly from the scaling relations.

In order to describe the overall processes, the adsorption energies of the six different surface species, O_2**, O*, OH*, Cl*, Br*, and I* are considered. In earlier studies O* was used to describe the adsorption of OH* [8, 5] and in [Paper I]. Later models, however, differentiate between O* and OH* adsorption energies [70] since their scaling behaviour is not always perfect. This can also be seen in figure 5.4 where the relation between OH* and O* is shown. While the overall trend between OH* and O* is clearly observed, a mean absolute error (MEA) of 0.74 eV suggests that one has to take care when using this scaling relation.

Interestingly, a few outliers, e.g. IrO_2 and VO_2, cause the large MEA.

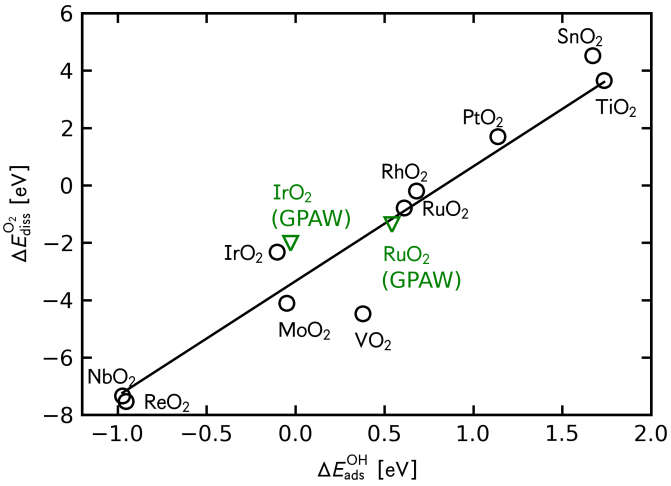

Figure 5.4: Dissociative chemisorption energy of O_2 ($\Delta E^{O_2}_{\text{diss}}$) plotted as a function of the adsorption energy of OH ($\Delta E^{OH}_{\text{ads}}$) on a variety of rutile(110) surfaces as obtained from DFT calculations. Gas-phase O_2 and H_2O are used as a reference, respectively.

We tested the values obtained for IrO_2 and RuO_2 with the all electron DFT code GPAW [71] using the RPBE functional[**?**], and obtained similar results, which are show as green triangles in the figure. This may indicate that the deviations originate from differences in the underlying physics of the systems that are not described by the scaling relations. We have therefore chosen to invoke OH* as a second descriptor in our model. It turns out that this is a better descriptor for the adsorption energies of the remaining species.

Figure 5.5 a) and b) show the scaling of intermediates as a function of OH* for the low and high coverage regimes, respectively. As can be seen in figure 5.5 a) the adsorption energies of the halides scale with the OH binding energy. A slope of 1 has been fitted through the binding energies of the halides giving reasonable correlations. The error does, however, increase when going from chlorine to bromine and is largest for iodine. The adsorption energy of O_2 has been found to scale best with the adsorption energy of OH as well. A slope of 1.42 is obtained when fitting through the O_2 adsorption values.

Figure 5.5 b) shows the scaling of the adsorption energies of chlorine,

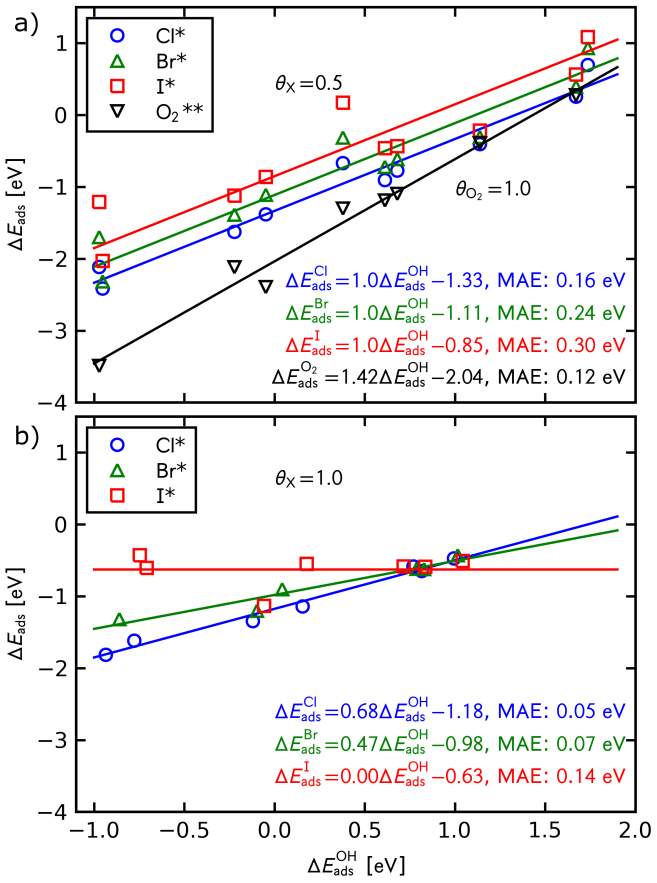

Figure 5.5: a) Adsorption energies of Cl, Br, and I at a coverage of 0.5 and adsorption energies of O_2 at a coverage of 1.0 plotted as a function of the chemisorption energy of OH at a coverage of 0.5 on a variety of rutile(110) surfaces as obtained from DFT calculations. b) Adsorption energies of Cl, Br, and I, at a coverage of 1.0 plotted as a function of the chemisorption energies of OH at a coverage of 1.0. OH coverage of 1.0 is achieved by adsorbing an OH in a 2x1 unit cell next to a Cl, Br, and I for the Cl, Br, and I scaling, respectively. Gas-phase Cl_2, Br_2, I_2, O_2, and H_2O are used as a reference, respectively.

bromine and iodine atoms in the high coverage regime. The slopes are less than those obtained for the low coverage and are decreasing from chlorine to bromine and iodine, with scaling relation for iodine having a slope of zero. This is due to an extensive interaction between two halides that are adsorbed next to each other. This interaction increases from chlorine to bromine and iodine so that the effect is largest for iodine. The interaction between halides can be seen as decreasing this scaling due to a decrease in interaction between the halides and the oxide surfaces.

5.5 Activity volcanoes

The scaling relations in figure 5.5 are used in order to establish volcano relations for the activity of the three different oxidation processes. The volcanoes are shown in figure 5.6. We have treated the case of high and low coverage as two separate models. Figure 5.6 combines these two models, where the more active one of the two is shown. Accordingly, O_2 dissociation energies and OH adsorption energies are shown for the respective cases of high and low coverage. For all three processes, RuO_2 is the oxide that is closest to the top of the volcano.

When moving along the diagonals of the volcano plots from lower left to upper right corner, we are going from the very reactive rutile surfaces to the most noble. Along this path we are also moving from a region where the high coverage model are shoving more activity to a region where the low coverage model are dominating. In the case of Cl_2 production the two models are shifting near the RuO_2 point and for Br_2 and I_2 it further to the left. All of this make good sense, however, it is not given that by the implementation of the model that e.g. the low coverage model should dominate in the actual low coverage regime (noble surfaces). Therefore as we move away from diagonal, the analysis of this combined models for high and low coverages of the halides should be used with caution. Another, more systematic but also more computational demanding way of introducing interactions between adsorbates in micro-kinetic models has been presented recently [72].

Furthermore, it should be noted that the volcano is quite steep and that the errorbars of materials that are located at the edges stretch over three orders of magnitude. This stresses again that our analysis is more of a trend study rather than a quantitative prediction of reaction rates.

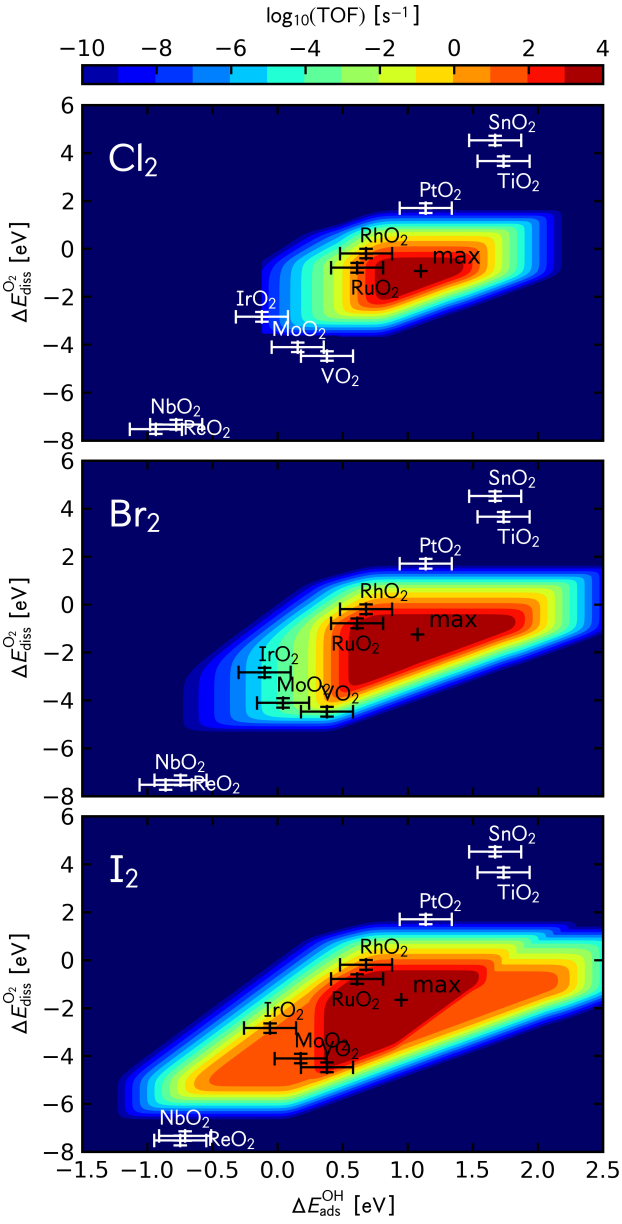

Figure 5.6: Volcano curves (turnover frequencies (TOFs) plotted as a function of $\Delta E_{\mathrm{ads}}^{\mathrm{OH}}$ and $\Delta E_{\mathrm{diss}}^{\mathrm{O_2}}$) for HCl, HBr, and HI oxidation. The TOFs are based on a combination of high and low coverage regimes, where the highest rate of these two is plotted. Accordingly, O_2 and OH binding energies of metal oxides employed in this study at high and low coverages are depicted with an error bar of 0.2 eV. Reaction conditions are: 573 K, ($p_{\mathrm{O_2}}$=0.6 bar, p_{OH}=0.3 bar, $p_{\mathrm{H_2O}}$=0.05 bar, and $p_{\mathrm{X_2}}$=0.05 bar)

5.6 Sabatier-Gibbs analysis

In this section the Sabatier-Gibbs analysis is performed on the reaction scheme (5.4) to (5.8). This is done both in order to get a deeper understanding of the reaction mechanism underlying the process and equally important to test the method on a real process. We will follow the procedure outlined in section 4.2.2 and 4.2.3.

The approaches to equilibrium γ_i in the rate equations are

$$\gamma_1 = \frac{\theta_{O_2}}{2K_1 p_{O_2} \theta_*^2} = \frac{\lambda_{O_2}}{K_1'}, \quad K_1' = 2K_1 p_{O_2} \tag{5.16}$$

$$\gamma_2 = \frac{2\theta_O^2}{K_2 \theta_{O_2}} = \frac{\lambda_O^2}{K_2' \lambda_{O_2}}, \quad K_2' = \frac{K_2}{2} \tag{5.17}$$

$$\gamma_3 = \frac{\theta_{OH}\theta_X}{K_3 p_{HX} \theta_O \theta_*} = \frac{\lambda_{OH}\lambda_X}{K_3' \lambda_O}, \quad K_3' = K_3 p_{HX} \tag{5.18}$$

$$\gamma_4 = \frac{p_{X_2}\theta_*^2}{K_4 \theta_{X_2}} = \frac{1}{K_4' \lambda_X}, \quad K_4' = \frac{K_4}{p_{X_2}} \tag{5.19}$$

$$\gamma_5 = \frac{p_{H_2O}\theta_O \theta_*}{K_5 \theta_{OH}^2} = \frac{\lambda_O}{K_5' \lambda_{OH}^2}, \quad K_5' = \frac{K_4}{p_{H_2O}} \tag{5.20}$$

where we have introduced the notation K_i' in order to simplicity the notation. The surface activities are:

$$\lambda_{O_2} = \frac{\theta_{O_2}}{\theta_*^2}, \quad \lambda_O = \frac{\theta_O}{\theta_*}, \quad \lambda_{OH} = \frac{\theta_{OH}}{\theta_*}, \quad \lambda_X = \frac{\theta_X}{\theta_*} \tag{5.21}$$

The overall approach to equilibrium γ i given by

$$\gamma = \frac{1}{K_1 K_2 K_3^4 K_4^2 K_5^2} \frac{p_{X_2}^2 p_{H_2O}^2}{p_{HX}^4 p_{O_2}} \tag{5.22}$$

Using equation (5.16) to (5.20) these can be written in terms of K_i' and γ_i

$$\lambda_{O_2} = \gamma_1 K_1' \tag{5.23}$$

$$\lambda_O = \sqrt{\gamma_1 K_1' \gamma_2 K_2'} \tag{5.24}$$

$$\lambda_{\mathrm{X}} = \frac{1}{\sqrt{\gamma_4 K_4'}} \tag{5.25}$$

$$\lambda_{\mathrm{OH}} = \gamma_3 K_3' \sqrt{\gamma_1 K_1' \gamma_2 K_2' \gamma_4 K_4'} \tag{5.26}$$

From equation (4.31) and (4.32) we recall that $\gamma = \gamma_1\gamma_2\gamma_3^4\gamma_4^2\gamma_5^2$ and $0 \leq \gamma \leq \gamma_i^{n_i} \leq 1$ which we can use in order to set upper and lower boundaries on the surface activities (5.23) to (5.26):

$$\lambda_{\mathrm{O_2}}^{\min} = \gamma K_1', \quad \lambda_{\mathrm{O_2}}^{\max} = K_1' \tag{5.27}$$

$$\lambda_{\mathrm{O}}^{\min} = \sqrt{\gamma K_1' K_2'}, \quad \lambda_{\mathrm{O}}^{\max} = \sqrt{K_1' K_2'} \tag{5.28}$$

$$\lambda_{\mathrm{X}}^{\min} = \frac{1}{\sqrt{K_4'}}, \quad \lambda_{\mathrm{X}}^{\max} = \frac{1}{\gamma^{\frac{1}{4}}\sqrt{K_4'}} \tag{5.29}$$

$$\lambda_{\mathrm{OH}}^{\min} = K_3' \sqrt{\gamma K_1' K_2' K_4'}, \quad \lambda_{\mathrm{OH}}^{\max} = K_3' \sqrt{K_1' K_2' K_4'} \tag{5.30}$$

From the coverage sum rule (5.15) we can find an expression for the fraction of free sites, θ_*, as function of the surface activities.

$$\theta_*^2 \lambda_{\mathrm{O_2}} + \theta_*(1 + \lambda_{\mathrm{O}} + \lambda_{\mathrm{OH}} + \lambda_{\mathrm{X}}) - 1 = 0 \quad \Leftrightarrow$$

$$\theta_*(\lambda_{\mathrm{O_2}}, \lambda_{\mathrm{O}}, \lambda_{\mathrm{X}}, \lambda_{\mathrm{OH}}) = \frac{-(1 + \lambda_{\mathrm{O}} + \lambda_{\mathrm{OH}} + \lambda_{\mathrm{X}}) + \sqrt{(1 + \lambda_{\mathrm{O}} + \lambda_{\mathrm{OH}} + \lambda_{\mathrm{X}})^2 + 4\lambda_{\mathrm{O_2}}}}{2\lambda_{\mathrm{O_2}}} \tag{5.31}$$

The maximum fraction of free sites are found when the surface activity of all species are at a minimum:

$$\theta_*^{\max} = \theta_*(\lambda_{\mathrm{O_2}}^{\min}, \lambda_{\mathrm{O}}^{\min}, \lambda_{\mathrm{X}}^{\min}, \lambda_{\mathrm{OH}}^{\min}) \tag{5.32}$$

where the surface activities are given by equation (5.23) to (5.26). The maximum coverage of $\mathrm{O_2}$, $\theta_{\mathrm{O_2}}^{\max}$, is found when the surface activity of $\mathrm{O_2}$are maximal and the other surface activities are in minimum. $\theta_{\mathrm{O_2}}$ is isolated from 5.15 while (5.31) is used for θ_*.

$$\theta_{\mathrm{O_2}}^{\max} = 1 - \theta_*(\lambda_{\mathrm{O_2}}^{\max}, \lambda_{\mathrm{O}}^{\min}, \lambda_{\mathrm{X}}^{\min}, \lambda_{\mathrm{OH}}^{\min}) \left(1 + \lambda_{\mathrm{O}}^{\min} + \lambda_{\mathrm{OH}}^{\min} + \lambda_{\mathrm{X}}^{\min}\right) \tag{5.33}$$

The maximal surface coverages are found in the same manner. For O* this becomes

$$\begin{aligned}\theta_{\mathrm{O}}^{\max} = 1 - \theta_*(\lambda_{\mathrm{O}_2}^{\min}, \lambda_{\mathrm{O}}^{\max}, \lambda_{\mathrm{X}}^{\min}, \lambda_{\mathrm{OH}}^{\min})^2 \\ -\theta_*(\lambda_{\mathrm{O}_2}^{\min}, \lambda_{\mathrm{O}}^{\max}, \lambda_{\mathrm{X}}^{\min}, \lambda_{\mathrm{OH}}^{\min}) \left(1 + \lambda_{\mathrm{OH}}^{\min} + \lambda_{\mathrm{X}}^{\min}\right)\end{aligned} \tag{5.34}$$

Now we can find the expressions for the maximal coverages, which we can use to find the maximal rates for each individual elementary steps:

$$r_1^{\max} = k_1 p_{\mathrm{O}_2} \theta_*^{\max 2} (1 - \gamma) \tag{5.35}$$

$$r_2^{\max} = \frac{1}{2} k_2 \theta_{\mathrm{O}_2}^{\max} (1 - \gamma) \tag{5.36}$$

$$r_3^{\max} = 4 k_3 p_{\mathrm{HX}} \theta_{\mathrm{O}}^{\max} \theta_*^{\max} (1 - \gamma^{\frac{1}{4}}) \tag{5.37}$$

$$r_4^{\max} = 2 k_4 \theta_{\mathrm{X}}^{\max} (1 - \gamma^{\frac{1}{2}}) \tag{5.38}$$

$$r_5^{\max} = 2 k_5 \theta_{\mathrm{OH}}^{\max 2} (1 - \gamma^{\frac{1}{2}}) \tag{5.39}$$

The Sabatier-Gibbs rate for the oxidation of hydrogen halides are then bound by $r_i^{\max}$ for the elementary steps:

$$R_{\mathrm{SG}} = \min\{r_1^{\max}, r_2^{\max}, r_3^{\max}, r_4^{\max}, r_5^{\max}\} \tag{5.40}$$

In figure 5.7, the resulting Sabatier-Gibbs rates are shown as dashed lines for Cl_2, Br_2 and I_2 production. The filled contour plot is the exact steady state solution. When comparing the to volcanoes it can be seen that the Sabatier-Gibbs analysis is given a result very close to the numerical solution in most of the area of the plot. Especially where the O_2 dissociation seems to be limiting, i.e. horizontal lines in the plot, the Sabatier-Gibbs analysis is very precise. Also in the area of weak binding of O and OH (upper right quarter) the agreement is perfect. For strong binding of OH there is a slightly disagreement corresponding to approximately a factor of three, and also at the top of the volcano where non of the coverages are optimal, the Sabatier-Gibbs analysis predicts a somewhat higher rate.

In the lower right quarter, however, the Sabatier-Gibbs analysis fails quantitatively. This deviation becomes large as we go down through the halides. This is because the reactions become more exothermic and we move away further away from equilibrium when we go from Cl and Br to

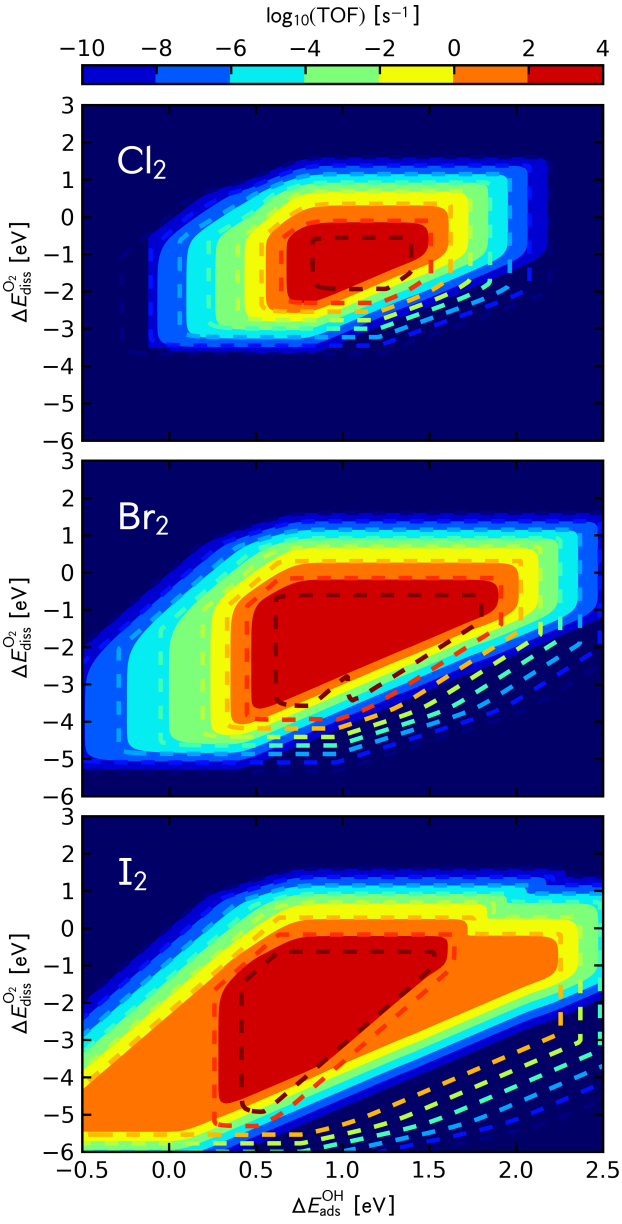

Figure 5.7: Numerical steady state solution to the rate equations ??? as in figure 5.6 compared to the Sabatier-Gibbs rate (5.40) shown by the dashed contour plot. The approaches to equilibrium are as follows; Cl: $\gamma = 6.4 \cdot 10^{-10}$, Br: $\gamma = 8.6 \cdot 10^{-13}$, I: $\gamma = 2.6 \cdot 10^{-36}$.

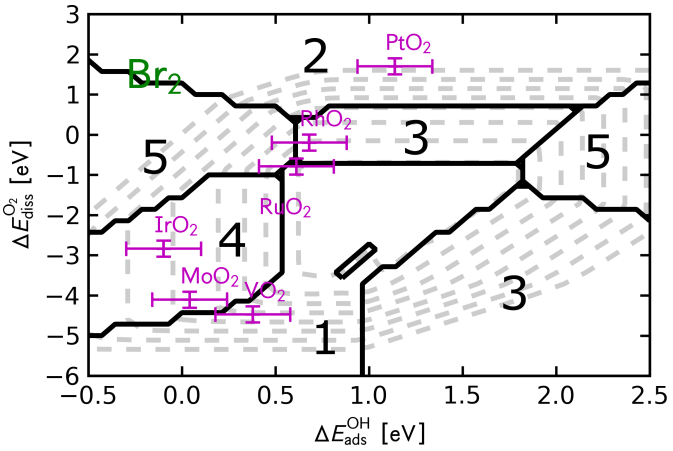

Figure 5.8: The numbers indicate which of the five rates (5.35) to (5.39) that are rate determining in the Sabatier-Gibbs analysis of the oxidation process of HBr. Gray dashed lines indicate the Sabatier-Gibbs volcano.

I, and as we recall from section 4.2.3 and 4.2.4 the Sabatier-Gibbs analysis becomes exact when the reaction is in equilibrium ($\gamma = 1$).

One of strengths of an analytical analysis is as mentioned before that we can get a more detailed understanding of the reaction mechanisms. As an example the predicted rate determining steps for the oxidation of bromine are shown in figure 5.8. The corresponding plots for chlorine and iodine are very similar. We can here see that for catalyst like RuO_2 and RhO_2 there are not only two, but three or four competing reaction steps at 573 K. In an earlier study reaction step 2) and 4) was chosen to be rate determining on the basis of the thermodynamics. Figure 5.8 shows that this is only half the truth and care should therefore be taking when making assumptions about rate determining steps. Sabatier-Gibbs could be good tool for finding which steps are rate determining.

5.7 Summary

We investigated the heterogeneously catalysed oxidation of the three halides HCl, HBr, and HI with molecular oxygen over rutile oxide (110) surfaces. We used the previously established reaction mechanism for HCl oxidation and assume that the HBr and HI oxidation follow a similar reaction mech-

anism. By employing a full micro-kinetic model without any presumptions on rate determining steps we were able to show that HCl and HBr oxidation over the $RuO_2(110)$ surface are starting at about 500 K while HI oxidation already starts at about 400 K. Interestingly, HI oxidation was found to occur at low I coverages, whereas high coverages of Cl and Br are needed to facilitate Cl_2 and Br_2 desorption.

We have extended earlier developed scaling relations between different adsorbates on rutile oxide surfaces and were able to describe all three reactions by only two parameters, $\Delta E_{\mathrm{ads}}^{\mathrm{OH}}$ and $\Delta E_{\mathrm{diss}}^{\mathrm{O_2}}$. These linear energy relations were combined with the micro-kinetic modelling leading to volcano-shaped relationships for HX oxidation. It was found that HX oxidation occurs at high coverages on the strong binding site whereas low coverages yield higher turnovers for the weaker binding oxides. RuO_2 was found to be close to the top of all three oxidation volcanoes. The rate over RuO_2 is observed to increase from chlorine to bromine to iodine. Having established these volcano relationships new catalytic materials could now in principle be screened using simple DFT calculations of adsorption energies of O and OH.

Furthermore, a Sabatier-Gibbs analysis was performed for the same processes and showed good agreement with the numerical solution. The rate limiting elementary reaction steps was established for most regions in the activity plot, by looking at the Sabatier-Gibbs rates. This means that Sabatier-Gibbs is a good tool to determine rate limiting steps.

It should be noted that HBr and HI oxidation is analysed under the presumption that the reaction mechanism is similar to that established for HCl. Importantly, further oxidation of Br_2 (I_2) to BrO_x species is neglected in this study. Inclusion of further oxidation products might, however, be an important part of the analysis and calls for a treatment on selectivity. In addition, the stability of the catalytic materials and their active surface is not treated in this study and needs to be taken into account in the search for HX oxidation catalysts due to the extremely harsh reaction conditions present.

Chapter 6

Kinetics of larger molecules

In chapter 5 about oxidation of hydrogen halides over rutile oxide surfaces, the adsorbed O_2 molecule is lying down on the surface and covers two active sites on the rutile (110) surface. Wondering about how to write up the kinetics correctly in this case let us into a scientific sidetrack. The result of this is presented in this chapter.

In the micro-kinetics described previously in chapter 4.2 the so called mean-field approximation has been assumed to apply. In the mean-field approximation it is assumed that all adsorbed species are distributed randomly over the surface, and that there are no interactions between adsorbates and that each adsorbate covers exactly one site.

If we consider a surface partly covered with two species that will react with each other. Within the mean-field approximation the rate of this reaction will be proportional to the product of the coverage of the two species. If one of the species is clustering on the surface due to attractive interactions the mean-field approximation will break down. The rate will decrease with the size of the clusters, because the reaction only takes place on the edges.

Another case where the mean-field approximation may not be as the good as desired, is when a large part of the surface is covered with large molecules blocking more than one site and the reaction considered depends on further adsorption of large molecules. The reason the mean-field approximation does not necessarily apply in this case is due to the fact that the large molecules occupies x sites next to each other on the surface. The occupied sites are therefore grouped together x by x, and x adjacent free sites are easier to find on a surface where the occupied sites are grouped

than if they are randomly spread. Because if the occupied sites are grouped so will the free sites be. How large effect this will have on the reaction rate is not obvious. In this section, we will address this question by looking at the adsorption of linear molecules.

$$\mathrm{A(g)} + x* \rightarrow \mathrm{A}^{(x*)} \tag{6.1}$$

Here $^{(x*)}$ means that surface species A occupies x sites. In the mean-field approximation we would write the rate of this reaction as

$$r = r_+ - r_- = k_+ p_\mathrm{A} (1-\theta)^x - k_- \frac{\theta}{x} \tag{6.2}$$

Here θ is defined as how large a fraction of the surface is covered with A molecules, i.e. $\theta = \frac{xj}{N}$ where j is the number of molecules and N is the total number of surface sites. In the first part of the equation, considering the forward going reaction, $(1-\theta)^x$ is the probability of finding x empty sites.

The configurational entropy within the mean-field approximation can be calculated to be

$$\Delta S_\mathrm{config} = k_\mathrm{B} \ln \frac{(1-\theta)^x}{\frac{\theta}{x}} \tag{6.3}$$

and we get

$$e^{\frac{\Delta S_\mathrm{config}}{k_\mathrm{B}}} = \frac{(1-\theta)^x}{\frac{\theta}{x}} \propto \frac{1}{\gamma} = \frac{r_+}{r_-} \tag{6.4}$$

In (6.2) it is neglected that the two sites has to be next to each other and that the free sites are not equally distributed over the surface. In the following we find the correct probability assuming that A_x is the only type of species on the surface.

We will consider a surface (or a lattice structures of any dimension) with N sites that each have z sites as nearest neighbors. The surface is decorated with j linear molecules each occupying x sites in a row. We will assume that $N >> x$. The number of free sites is $N - xj$ and the number of ways to choose two adjacent sites of which the first is free is $z(N - xj)$. This system is similar to the ones described by Guggenheim in 1944 [73, 74] and Dimarzio in 1961 [75] and we will adapt the same way of counting.

Each adsorbed molecule has $(zx - 2x + 2)$ neighbor sites. From this follows that the number of ways to choose two sites where the fist one is

occupied and the second is either free or occupied by another molecule than the first site is $(zx-2x+2)j$. If P denotes the probability that a neighbor site to either a molecule or a free site is free, then $(zx-2x+2)jP$ is the number of combinations of two adjacent sites where one is free and the other is occupied.

When we have realized the above reasoning we can write the probability that a neighbor site to a free site is occupied $(1-P)$ as the number of ways to choose two sites where the first is free and the second occupied over the total number of ways to choose two sites where the first one is free.

$$1-P=\frac{(zx-2x+2)jP}{z(N-xj)} \tag{6.5}$$

This gives an expression for the probability that a given neighbor site to a free site is also free

$$P=\frac{z(N-xj)}{z(N-xj)+(zx-2x+2)j}=\frac{N-xj}{N-\frac{2}{z}(x-1)j} \tag{6.6}$$

Now we can start putting molecule number $j+1$ onto the surface segment by segment. The first segment has $(N-xj)$ site to choose from and when the first segment of the molecule is placed the next one has an expected number of zP free sites to choose from. As we are only looking at straight and linear molecules the rest of the segments are placed in the same direction as the second with the probability P that the given site is free. Now we can write up the total number of ways to place the $(j+1)$th molecule onto the surface.

$$\nu_{j+1}=\frac{z}{2}(N-xj)P^{x-1}=\frac{z(N-xj)^x}{2\left(N-\frac{2}{z}\left(x-1\right)j\right)^{x-1}} \tag{6.7}$$

$$=\frac{\left(\frac{z}{2}\right)^x x^x}{(x-1)^{x-1}}\frac{(\frac{N}{x}-j)^x}{\left(\frac{zN}{2(x-1)}-j\right)^{x-1}} \tag{6.8}$$

We have divided by 2 in order not to double count. The number of combinations in which we can place n molecules onto the surface is

$$g=\frac{1}{n!}\prod_{j=0}^{n-1}\nu_{j+1} \quad = \quad \frac{\left(\frac{z}{2}\right)^{xn}x^{xn}}{(x-1)^{(x-1)n}}\frac{\left(\frac{N}{x}\right)!^x\left(\frac{zN}{2(x-1)}-n\right)!^{x-1}}{\left(\frac{N}{x}-n\right)!^x\left(\frac{zN}{2(x-1)}\right)!^{x-1}n!} \tag{6.9}$$

$$\approx \quad \frac{\left(\frac{z}{2}\right)^{xn}N!\left(\frac{z}{2}N-n(x-1)\right)!}{(N-xn)!\left(\frac{z}{2}N\right)!n!} \tag{6.10}$$

Where it in the last term has been used that we from Stirling's approximation, $\ln(N!) \approx N \ln N - N$, can write $\frac{N}{x}!^x \approx \frac{N!}{x^N}$.

The configurational entropy, S, is given by

$$S_{\text{config}} = k_B \ln(g) \tag{6.11}$$

Using Stirling's approximation again this gives

$$\begin{aligned}\frac{S_{\text{config}}(n,N)}{k_B} &= nx \ln \frac{z}{2} + N \ln N \\ &\quad + \left(\frac{z}{2}N - n(x-1)\right) \ln \left(\frac{z}{2}N - n(x-1)\right) \\ &\quad -(N - xn) \ln(N - xn) - \frac{z}{2} N \ln(\frac{z}{2}N) - n \ln n \end{aligned} \tag{6.12}$$

which can be rewritten into

$$\begin{aligned}\frac{S_{\text{config}}(\theta)}{N k_B} &= \frac{z}{2}\left(1 - \frac{2x-2}{zx}\theta\right) \ln \left(1 - \frac{2x-2}{zx}\theta\right) \\ &\quad -(1-\theta)\ln(1-\theta) - \frac{\theta}{x}\ln\frac{\theta}{x} + \frac{\theta}{x}\ln\frac{z}{2}\end{aligned} \tag{6.13}$$

where the substitution $\theta = \frac{xn}{N}$ has been made.

In order to find the change in configurational entropy S_{config} has to be differentiated with respect to n:

$$\Delta S_{\text{config}} = \frac{dS_{\text{config}}}{d\theta}\frac{d\theta}{dn} = k_B \ln\left(\frac{(1-\theta)^x}{\frac{\theta}{x}(1 - \frac{2x-2}{zx}\theta)^{x-1}}\right) \tag{6.14}$$

r_+/r_- is proportional to the fraction inside the natural logarithm:

$$\frac{r_+}{r_-} \propto \frac{(1-\theta)^x}{\frac{\theta}{x}(1 - \frac{2x-2}{zx}\theta)^{x-1}} \tag{6.15}$$

From this it is not apparent which part of the fraction that belongs to the forward and the backward rate. However, the backward rate has to be proportional to the number of molecules on the surface

$$r_- \propto \frac{\theta}{x} \tag{6.16}$$

which leaves the following for the forward rate

$$r_+ \propto \frac{(1-\theta)^x}{(1 - \frac{2x-2}{zx}\theta)^{x-1}} \tag{6.17}$$

Because there is no interaction between the molecules, we imagine that when the gas-phase molecule approaches the surface it has a pre-determent direction against x specific sites in a straight line. The factor in (6.17) should be the probability that the x given sites are all free, i.e. the number of combination for a set of x free sites (6.7) divided by the total number of combinations free or not

$$r_+ \propto \frac{\nu_{j+1}}{\frac{z}{2}N} \tag{6.18}$$

This gives the same factor as in (6.17). The total rate equation becomes

$$r = r_+ - r_- = k_+ p \frac{(1-\theta)^x}{(1-\frac{2x-2}{zx}\theta)^{x-1}} - k_- \frac{\theta}{x} \tag{6.19}$$

Equation (6.19) is derived under the assumption that only molecules of the type A_x are populating the surface. However, during a catalytic reaction more than one species are usually adsorbed on the surface. The equation is therefore only true in the limit where the coverage of A, θ, is much larger than the coverage of all other species. In the other limit where $\theta \to 0$, (6.2) is a more accurate rate equation.

The two different expressions for the rate (6.2) and (6.19) differ from each other by a factor of

$$\frac{1}{(1-\frac{2x-2}{zx}\theta)^{x-1}} \tag{6.20}$$

In figure 6 the logarithm of this factor is plotted as a function of θ for two lengths of molecules, $x = 2$ and $x = 5$, on two different types of surfaces. A surface with $z = 6$ could be a closed packed surface and $z = 2$ could be the coordination of the reactive sites along a step edge or the rows of metal atoms on a rutile oxide (110) surface (see figure 3.3 c)). When looking at the figure we get an idea of how important this correction to the mean-field approximation is. For the three cases with the lowest values the correction will be of no importance. In these cases the rate might be up to a factor of three larger. A factor of three in the turn over frequency is of cause important in an industrial process, however in DFT based micro-kinetic modeling this number is much smaller than e.g. errors introduced by uncertainty in the calculated energy barrier (section 4.3). The correction do become important when we look at large molecules on low coordinated surfaces, and the mean-field approximation might be

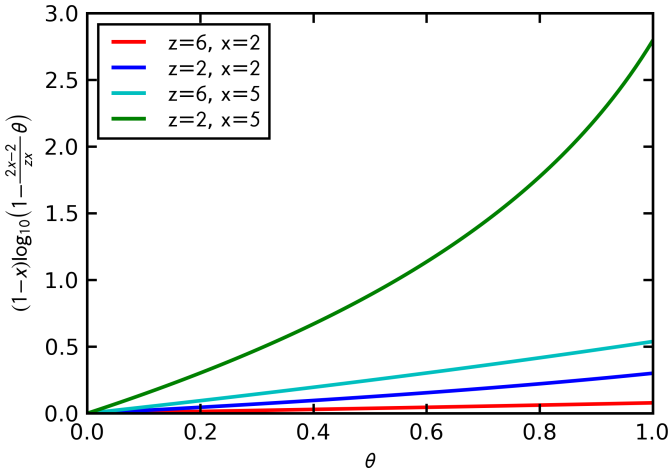

Figure 6.1: Additional factor (6.20) to the forward rate of (6.2) due to the difference in configurational entropy between the mean-field approximation and the case where the surface is covered with linear noninteracting molecules occupying x sites each plotted as a function of surface coverage. z is the coordination of the surface.

insufficient to describe the kinetics. The Langmuir isotherms in figure 6 shows in the same four cases, for which combined values of p_{A}, the equilibrium constant K and θ the reaction will obtain equilibrium. The isotherms for the mean-field approximation is plotted (dotted lines) for comparison. The same conclusions can be drawn from this figure. Only for very large molecules the deviations from the mean-field approximation becomes important. For diatomic molecules we can neglect the influence of the small change in surface entropy on the reaction rate.

This analysis could be extended to also include other shapes of molecules. However, although the equation would be different, the overall conclusion would most likely be the same.

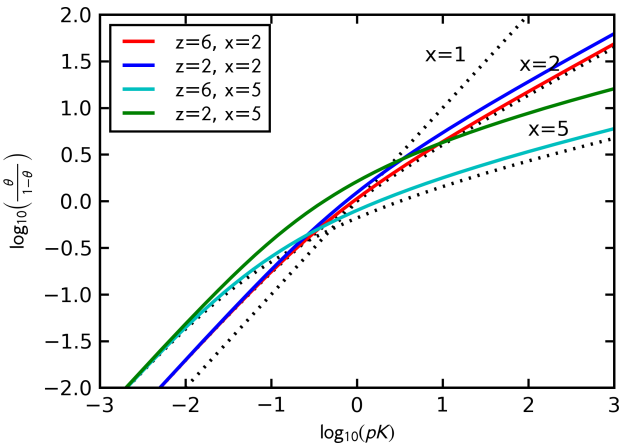

Figure 6.2: Langmuir isotherms. A transformed coverage as a function of $p_{\mathrm{A}}K$ for reaction (**??**) in four different cases of linear molecules covering x sites each on a z coordinated surface. The black dotted lines are examples of the same in the mean-field approximation.

Chapter 7

Trends in zeolite activity

Zeolites are an important class of materials for use in industrial catalytic processes. They are basically composed of SiO_4 tetrahedral units, which are connected to each other by sharing the oxygen atoms in the tetrahedral corners. The units can be assembled in many different ways, giving a large variety of micro porous crystalline framework structures containing channels and cages. Some zeolites structures are found in nature while others are only produced synthetically. When a tetrahedral framework Si^{4+} ion is replaced by an element in the 3+ oxidation state, usually Al^{3+}, cations will be present to compensate for the framework charge. If the compensating cation is a proton H^+ a bridging hydroxyl group (Al-(OH)-Si) is formed. This gives rise to a Brønsted acidity. The zeolite can then act as a solid acid. Other elements, such as B, Ge, Zn, P and transition metals can also be incorporated in the frame work [76, 77, 78, 79, 80].

Acid zeolites are very important for hydrocarbon conversion reactions including cracking and isomerization. This is not only due to their property as solid acids, but also because of their very uniform cavities with small diameters of approximately 6-13 Å. This means they can act shape selective with respect to reactants, product and transition states species [31]. However, herein we are only concerned with the active Brönsted acidic site of zeolites. This chapter includes a small collection of unpublished results, including a contribution to answer the question of what is controlling the distribution of aluminium centers, some simple comparisons to experimental values, and finally a study showing that scaling relations (section 3.1) also apply to transition metal substituted zeolites.

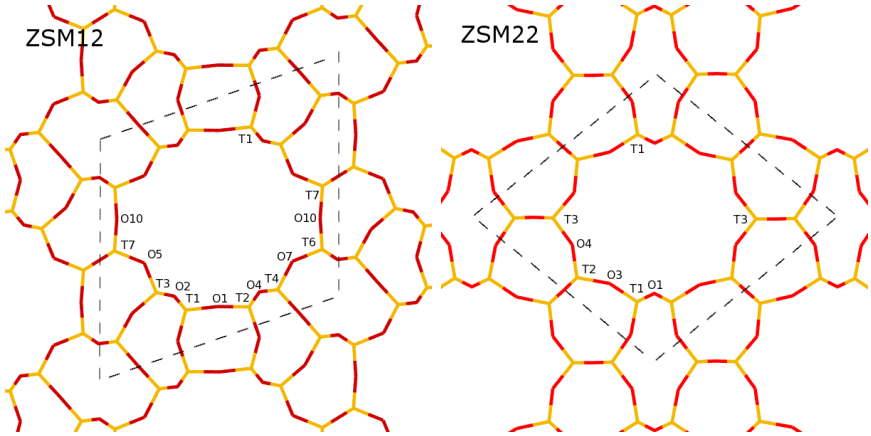

Figure 7.1: Schematic representation of the structures of the two zeolites ZSM12 and ZSM22. The cross sections is perpendicular to the direction along the channel. Yellow lines represent the T-atoms (Si or Al) and red lines are oxygen atoms. Each T- and oxygen atom in a unique local configuration is denoted with a T or an O and a number. The dashed line indicates the size of the unit-cell.

7.1 Calculated structures

The two different zeolite structures ZSM12 and ZSM22 have been used in the calculations in this chapter, and are shown schematically in figure 7.1. They are both one dimensional, which means that they have straight channels going through the zeolite in only one direction. These two zeolites are chosen because they both (especially ZSM12) despite their small unit cells have large numbers of geometrically different tetrahedral center atoms (T-atoms) in the channel per unit cell. In ZSM12 we have the possibility to create 22 geometrically different hydroxyl groups, whereof 12 have direct access to the channel. Similar in ZMS22 there are 10 different groups and 5 of them are accessible from the channel. It was the hope that investigation of these different acid sites would be able to provide a large enough dataset to get general information about the Brønsted type of acidity in zeolites.

The main difference between the two zeolite structures is that the main channel in ZSM12 consists of rings with 12 T-atoms whereas the one in ZSM22 is a 10 ring channel. They both have 6 and 5 membered rings in the structure and ZSM12 also have a 4 membered ring.

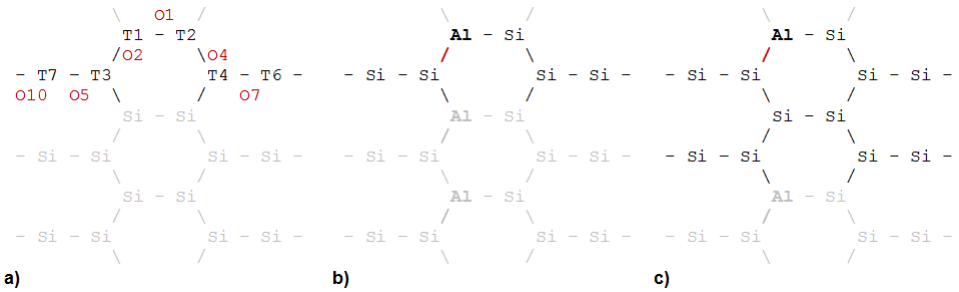

Figure 7.2: Very schematic representation of the configuration of half a channel of ZSM12. The view is from inside the channel toward the channel wall. a) is showing the position of the different T-atoms and notation of the oxygen in between. b) and c) are both showing systems with the local configuration denoted T1O2. In b) Al are sitting as next nearest neighbors (NNN) (Al-Si-Al) and in c) there are three Si between each Al. The black part of the drawings indicates the atoms included in the unit-cell and the red line shows the position of the hydroxyl group.

In the calculations the unit cells of both zeolites have been reduced to the primitive unit cells. This means that they have been reduced to half the size of the conventional unit cell. In some of the calculations the unit cell have been doubled in the direction along the channel. This has been done in order to reduce interaction between adjacent hydroxyl groups or adsorbates, and to increase the Si/Al ratio. In this way we have the possibility of varying the Si/Al ratio of ZSM12 from 13 for the small unit cell to 27 for the large unit cell. In the case of ZSM22, the ratio can be varied from 11 to 23. The unit cell dimensions are relaxed for the pure SiO_2 crystal.

7.2 Stability of the active sites

The siting of Al in zeolite structures has been the cause of an intensive debate. Different rules have been set up in order to explain why the Al content of a zeolite is limited to a specific value. The rule of Löwenstein [81] forbids Al-O-Al links. This has been shown experimentally by NMR [82, 83, 84, 85] and small cluster calculations [86, 87] to apply to at least many zeolites. Furthermore, Dempsey's rule states that Al-O-Si-O-Al links

where Al atoms are next nearest neighbors (NNN) are unfavorable. The argument is based on the electrostatic considerations that the negatively charged Al would sit as far from each other as possible. Also, this has been validated by experiments to apply for many zeolites [88, 89]. However, Schröder and Sauer [90] found through theoretical calculations that clusters, where two Al sit as NNN in a ring of four T-atoms have a lower lattice energy than configurations with Al sitting far from each other in the cluster. They only found this minimum for NNN if the Al-(OH)-Si bridges were located opposite each other in the ring. This finding was shortly thereafter confirmed by experiments [91]. This section does not include a comprehensive study of the siting of aluminum in zeolites but an observation in line with the previous studies.

All the different combinations of hydroxyl groups are calculated for H-ZSM12 and H-ZSM22 in two different sizes of unit cells, which gives rise to two different types of longer ranging geometries. In the smaller unit cell the Al atoms are sitting as NNN (i.e. Al-O-Si-O-Al). In the larger unit cell, which is double the size of the small one in the direction along the channel, there are three Si atoms between each Al (i.e. Al-O-Si-O-Si-O-Si-O-Al). Figure 7.2 shows an example of the two different types of geometries. In figure 7.2 b), the hydroxyl group is located in the same local geometry (i.e. Al and H at the same T and O sites) as in figure 7.2 c) but the distance between the Al is different. In figure 7.3, the total energy of the two different types of geometries are plotted against each other for each local combination of the hydroxyl group. Each local structure has been given a notation, which is a combination of the name of the T-atom where Al has been substituted and the name of the oxygen on which H is adsorbed. This results in notations like T1O2 and T3O4 for the different local geometries. Figure 7.1 and 7.2 a) show the name of each of the T- and oxygen atom.

In figure 7.3 we can compare the stability of the different configurations in the two zeolites. There is a larger difference between the least and the most stable configuration in H-ZSM12 than in H-ZSM22. Moreover, almost all sites are lower in energy in H-ZSM22 compared to the sites in H-ZSM12, which means that ZSM22 in general is stabilized more (or less unstabilized) by substitution of Al. The most stable Al sites in H-ZSM22 seems to be T4, which is in agreement with the references [92, 93] where both experiments and calculations predicts that 60% of the Al in ZSM22 are located at the T4 site. It should however be noted that energy differences in this study

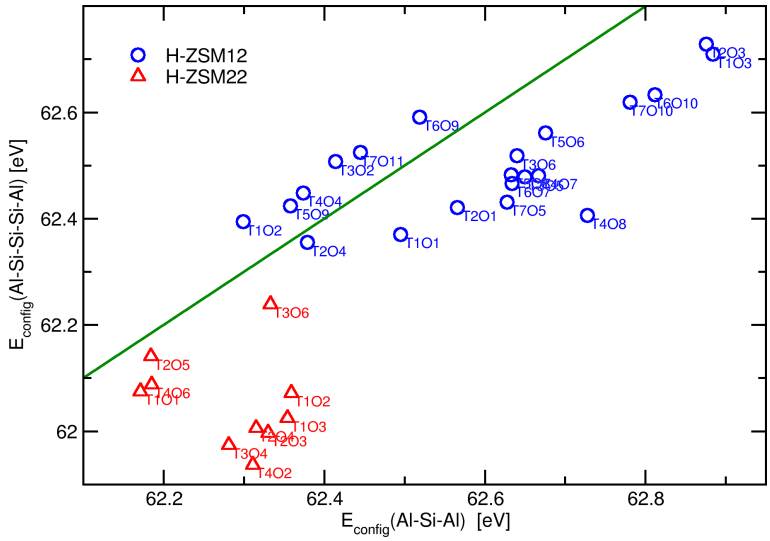

Figure 7.3: Energies of the different configurational combinations of the position of the substituted Al and the OH-group next to it in H-ZSM12 and H-ZSM22. The energies of structures with the same local configurations are plotted against each other. On the x-axis are the energies of configurations with Al as NNN (Al-Si-Al) and on the y-axis the energies of configurations with three Si between the Al (Al-Si-Si-Si-Al). The green line indicates x=y. The energy scales on the x- and y-axis have the same arbitrary reference energy. The label at each point denotes at which T-site the Al is sitting and at which oxygen the hydrogen is adsorbed.

are way to small to give a certain prediction of this. Moreover, it may not be the most energy favorable structures that are produced during synthesis.

The main observation in figure 7.3 is that in the case of H-ZSM12 the points fall into two groups. Each with an apparent linear relation with an approximate slope of 1. Although the energy difference between the two lines is comparable to the error within DFT, the two distinct groups are to evident to be ignored. One group is above the green x=y line, i.e. the site are more stable in the small unit cell, and one group is below the x=y line meaning the sites are more stable in the larger unit cell. The same trend is seen in H-ZSM22, although both groups fall into the regime below the x=y line meaning the sites are more stable in the larger unit cell. On average, the points lie lower than the x=y line also for H-ZSM12. Substituting

Al introduces some strain in the framework. In the larger unit cell, this strain will have a larger distance to even out, which will lower the energies in general compared to the small unit cell. This effect seems to be much larger in H-ZSM22, which might be due to the smaller size of the unit-cell.

In all the configurations in the group that lies above the x=y line in H-ZSM12 and the corresponding highest lying group in H-ZSM22 the proton is placed next to the Si that has two Al as nearest neighbors in the small unit cell. In all these configurations the Al-(OH)-Si link is pointing more or less along the channel. This means that the dipole moments created by negatively charged Al atoms and the positive H atoms also are pointing along the channel. The structures with short distance between the Al centers will therefore be stabilized by the aligned dipoles. The other group corresponding to the low lying points in figure 7.3 Have configurations with Al-(OH)-Si links perpendicular to the direction of the channel. The dipoles are therefore parallel and will repel each other in the structures with short distances between the Al centers. This will make these structures less stable.

This study shows that each local configuration in H-ZSM12 will prefer to be part of a Al-O-Si-O-Al configuration (contrary to Dempsey's rule) only if it can be stabilized by the dipole moments of the Al-OH groups. This is in line with Schröder and Sauer's [**?**] finding. When Al and the proton sit opposite each other in a four membered ring the dipoles are parallel but pointing in opposite directions and therefore stabilizing each other. It also shows that the strain introduced by the substituted Al can be larger than the stabilization of dipole moments as in the calculated configurations of H-ZSM22 and Dempsey's rule will apply.

The configurations here are unnatural as the Al are substituted in a straight line. This will introduce strain across the entire zeolite. Moreover, the unit-cell is not relaxed in the strained direction. Therefore, we cannot conclude anything from these calculation about how Al is distributed in the zeolite, only come with a suggestion to which mechanisms that are controlling it.

7.3 Acidity measures

Measuring the acidity of zeolites is of great interest but not straight forward. The most frequently used method to measure the acidity is simply

to measure the catalytic activity. However, this method is unreliable as it does not give a qualitative result. Some sites may not be accessible to the reactants and some may be less active in some reactions than in others. Methods that provide information about the strength and number of the acid sites are of great importance in understanding the catalytic activity and behavior of zeolites. Other methods used to characterize the acidity include NMR, TPD of small molecules and IR spectroscopy of small molecules. In this section, it is shown that calculated quantities fit well with experiments. First, calculations of vibrational frequencies of CO adsorbed on an acid site are compared to IR studies, and second, it is shown that the calculated adsorption energies of NH_3 are in agreement with TPD measurements.

7.3.1 OH and CO vibrational frequencies

Carbon monoxide is a common probe molecule for IR studies. It has a clearly observable stretching mode that shifts when the molecule is adsorbed, and it influences the OH stretch through a weak hydrogen bond interaction. Both of these shifts can easily be seen in experimental data. The shift, $\Delta\nu_{\mathrm{OH}}$, in the OH vibrational frequencies when CO is adsorbed in the zeolite is an indication of the strength of the OH bond, and consequently it is an indication of the acidity of the zeolite.

Here the vibrational frequencies of CO and OH stretching modes have been calculated with the CO adsorbed in the zeolites and without. This has been done using the harmonic normal mode approximation. This enables us to perform calculations of the relative shifts $\Delta\nu_{\mathrm{CO}}$ and $\Delta\nu_{\mathrm{OH}}$, which should be reasonably accurate, while the calculated absolute values of the vibrational frequencies are unreliable. In table 7.3.1 these shifts are compared to the ones found experimentally by IR [94]. The calculations for H-ZSM12 fit surprisingly well with the experimental data.

	DFT	Exp.
	H-ZSM12	H-ZSM12
$\Delta\nu_{\mathrm{OH}}$	-343	-321
$\Delta\nu_{\mathrm{CO}}$	39	37

Table 7.1: Calculated shifts in CO and OH vibrational frequencies [cm^{-1}] compared to experimentally found values [94].

7.3.2 Desorption temperature of NH_3

TPD of ammonia is a widely use method for obtaining the densities of Brönsted acid sites. Here calculated adsorption energies are compared to the peaks shown in TPD spectra. The calculated desorption temperatures are the temperatures at which NH_3 becomes more stable (i.e. lower free energy) in the gas phase than adsorbed at a Brönsted site in the zeolite channel. The free energy has been calculated using equations (4.4) and (4.5). There are usually two peaks in a TPD spectra of a zeolite. One at high temperature associated with the highly reactive Brönsted sites and another at lower temperature, which is associated with the less reactive Lewis acids, which are primarily extra-framework ions in the channels. The calculated temperatures are compared to the high temperature peak in table 7.3.2

	DFT	TPD
H-ZSM12	560	658
H-ZSM22	620	723

Table 7.2: Calculated desorption temperatures of NH_3 in Kelvin compared to TPD measurements for H-ZSM12 [95, 96] and H-ZSM22 [97, 98].

The calculated temperatures are shifted down by a constant of $\sim$100 K compared to the TPD peaks. This is reasonably satisfactory, as the theoretically calculated temperatures are very sensitive to small errors, and also the peaks in the TPD spectra can vary with respect to the experimental conditions [99]. Furthermore, the diffusion out of the channel has not been taken into account in the calculations.

7.4 Trends in transition metal exchanged zeolites

In this section, the study has been extended to also concern substitution of a wide range of elements other than Al into ZSM12. These elements include 3d, 4d and 5d transition metals. It is shown that the scaling relations addressed in section 3.1 are also valid for these transition metal substituted zeolites.

In Figure 7.4, the hydrogen binding energy is plotted as a function of the group number of the substituted element. In addition to the transition

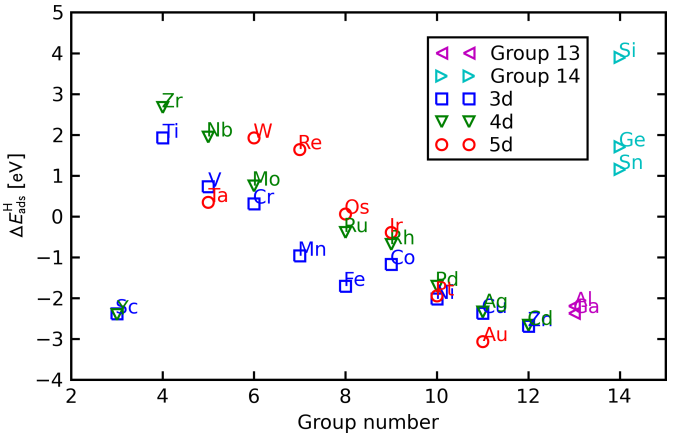

Figure 7.4: Hydrogen binding energy of each substituted zeolite relative to H_2 in the gas-phase plotted as a function of the group number of the dopant.

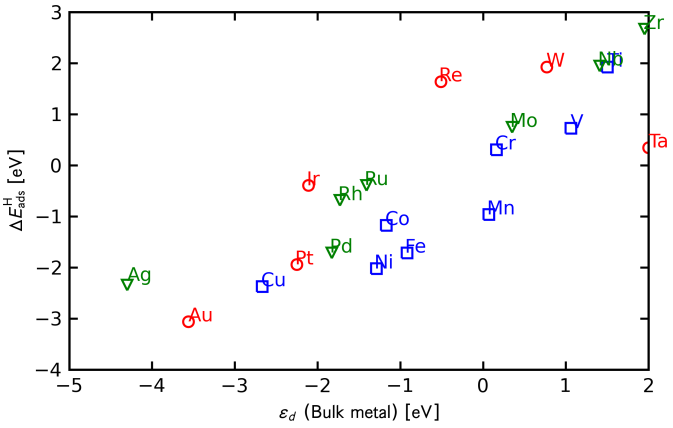

Figure 7.5: Hydrogen binding energy as a function of the d-band center relative to the fermi-level for the dopant in the bulk state. Legends as in figure 7.4

metals, group 3 and group 4 elements are included in the figure. The group 3 elements Al and Ga are included because they are the most commonly used dopants in zeolites. Si, Ge, Sn from group 4 are less interesting as they, as expected, do not bind the hydrogen at all due to their stable +4 oxidation state. They are included as a control group. Al and Ga binds hydrogen with almost same strength, and we see that Sc and Y behave very much the same. This is because they like the group 3 elements have 3 valence electrons. Looking at the other transition metals we see a trend of increased binding energy for increasing number of electrons in the valence shell. Consequently, we expect the acidity to be reduced for the strongly binding doped zeolites.

The trend in figure 7.4 can be explained by the electronic structure of the transition metal substituted in to the zeolite. Figure 7.5 illustrates the hydrogen binding in the doped zeolite versus the d-band center of the bulk metal. Here it can be seen that there is an almost linear dependency. This picture is opposite the correlation with respect to the transition metal elements as it was seen in the scaling relations section 3.1, for adsorption on transition metal and compound surfaces. There the general trend was weaker bonds to the surface when moving toward the right in the periodic table with the decreasing level of the *d*-band, e.g. the zeolites with the more noble metals substituted are more reactive. This is due to the difference in adsorption sites in the two cases. In section 3.1 the adsorbents bind directly to metal atoms, whereas, in this case the hydrogen is sitting on an oxygen atom next to the metal atom. The adsorption of hydrogen is therefore more directly influenced by the electronic structure of the oxygen atom. In figure 7.6, the hydrogen bonding energy is therefore shown as a function of the p-band center of the oxygen atom at which the hydrogen binds. The p-band center is calculated from the system without hydrogen adsorbed. Again, we see a linear correlation and the 3d and 4d metal substituted zeolites fall almost exactly on the same line while the hydrogen adsorption on 5d metal substituted zeolites is about 1 eV lower in energy.

The relations in figure 7.5 and 7.6 indicate that there exists a relation between the electronic structure of the bulk metal and the oxygen atoms next to the metal atom in the zeolite. This is verified in figure 7.7, which shows clear relations between the oxygen p-band center and the d-band center of the 3d, 4d and 5d the bulk metal, respectively. This implies that as the oxygen to metal interaction is strengthened the oxygen to hydrogen interaction is weakened.

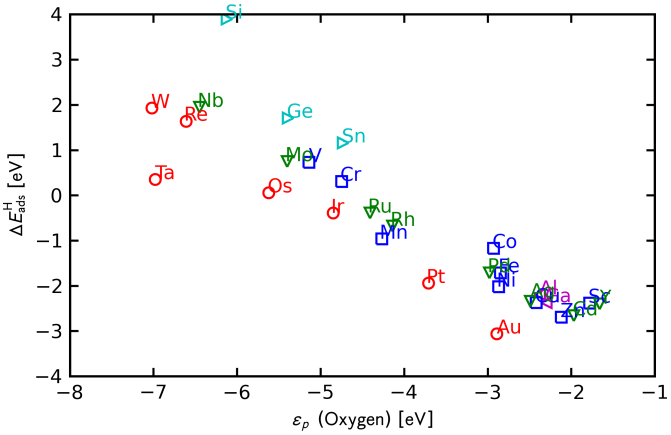

Figure 7.6: Hydrogen binding energy as a function of the p-band center relative to the fermi-level for the oxygen atom to which hydrogen adsorbs. The p-band center are found before H is adsorbed. Legends as in figure 7.4

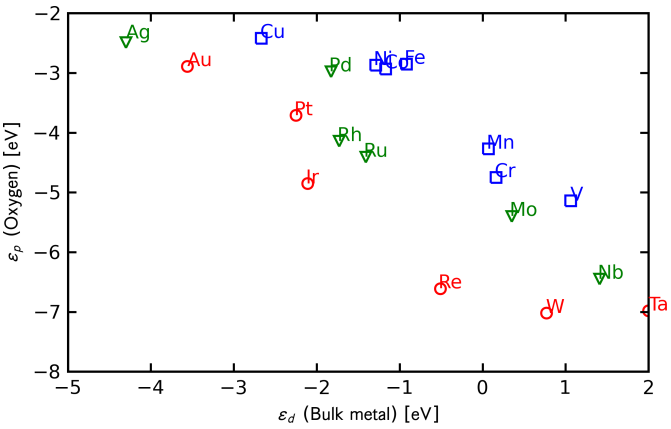

Figure 7.7: Relation between the d-band center of the bulk dopant and the p-band center of the oxygen to which H adsorbs. Legends as in figure 7.4

7.5 Conclusion

It has been shown that we calculate the zeolite structures precisely enough to observe the small effects due to strain and dipole moments introduced by Al-(OH)-Si groups in the zeolite. And the effects found are in good agreement with earlier investigations [90]. Furthermore, the calculations gives good results compared with experiments.

The main conclusion of this chapter is that the scaling relations [12, 55] can be extended to also include transition metal exchanged zeolites. It has been shown that the electronic structure of the p-orbitals on oxygen serves as a descriptor for the reactivity of the zeolite as the d-band does for the reactivity on transition metals. Furthermore, it has been shown that the p-band center of the oxygen atom is directly related to the d-band center of the dopant in the bulk state.

Chapter 8

Summary

Various results regarding linear energy relations have been presented throughout this thesis. It has been shown that scaling relations also apply to compound surfaces, and that the physics of adsorption on these surfaces must be essentially the same as described by the *d*-band model for adsorption on transition metal surfaces. Furthermore, it has been established that oxides and in particular rutiles are a very interesting class of materials in the sense of heterogeneous catalysis. This has been done by showing that they essentially have no activation barrier for dissociation reactions for the interesting catalysts with dissociative chemisorption energies just below zero.

The heterogeneously catalyzed oxidation of the three halides HCl, HBr, and HI with molecular oxygen over rutile oxide (110) surfaces was investigated. A previously established reaction mechanism for HCl oxidation was used and it was assumed that the HBr and HI oxidation follow a similar reaction mechanism. By employing a full micro-kinetic model without any presumptions on rate determining steps it was shown that HCl and HBr oxidation over the $RuO_2(110)$ surface are starting at about 500 K while HI oxidation already starts at about 400 K. Interestingly, HI oxidation was found to occur at low I coverages, whereas high coverages of Cl and Br are needed to facilitate Cl_2 and Br_2 desorption.

Linear energy relations were combined with the micro-kinetic modeling leading to volcano-shaped relationships for hydrogen halide oxidation and all three reactions was described by only two parameters, $\Delta E_{\mathrm{ads}}^{\mathrm{OH}}$ and $\Delta E_{\mathrm{diss}}^{\mathrm{O_2}}$. It was found that hydrogen halide oxidation occurs at high coverages on the strong binding site whereas low coverages yield higher turnovers for the weaker binding oxides. RuO_2 was found to be close to the top of

all three oxidation volcanoes. The rate over RuO_2 is observed to increase from chlorine to bromine to iodine. Having established these volcano relationships new catalytic materials could now in principle be screened using simple DFT calculations of adsorption energies of O and OH.

Finally calculations of transition metal substituted zeolite showed that the same type of scaling relations obtained for metals and compound materials, can be extended to also include transition metal exchanged zeolites. It has been shown that the electronic structure of the p-orbitals on oxygen serves as a descriptor for the reactivity of the zeolite as the d-band does for the reactivity on transition metals. Furthermore, it has been shown that the p-band center of the oxygen atom is directly related to the d-band center of the dopant transition metal in the bulk state.

Bibliography

[1] I. E. Maxwell. Driving forces for innovation in applied catalysis. *11th International Congress on Catalysis - 40th Anniversary, Pts a and B*, 101:1–9, 1996.

[2] S. Wendt, R. Schaub, J. Matthiesen, E. K. Vestergaard, E. Wahlstrom, M. D. Rasmussen, P. Thostrup, L. M. Molina, E. Laegsgaard, I. Stensgaard, B. Hammer, and F. Besenbacher. Oxygen vacancies on tio2(110) and their interaction with h2o and o-2: A combined high-resolution stm and dft study. *Surface Science*, 598(1-3):226–245, December 2005.

[3] K. Reuter, D. Frenkel, and M. Scheffler. The steady state of heterogeneous catalysis, studied by first-principles statistical mechanics. *Physical Review Letters*, 93(11):4, 2004.

[4] M. D. Rasmussen, L. M. Molina, and B. Hammer. Adsorption, diffusion, and dissociation of molecular oxygen at defected tio2(110): A density functional theory study. *Journal of Chemical Physics*, 120(2):988–997, 2004.

[5] J. Rossmeisl, Z. W. Qu, H. Zhu, G. J. Kroes, and J. K. Norskov. Electrolysis of water on oxide surfaces. *Journal of Electroanalytical Chemistry*, 607(1-2):83–89, 2007.

[6] S. Chretien and H. Metiu. Density functional study of the co oxidation on a doped rutile tio2(110): Effect of ionic au in catalysis. *Catalysis Letters*, 107(3-4):143–147, 2006.

[7] G. Pacchioni. Modeling doped and defective oxides in catalysis with density functional theory methods: Room for improvements. *Journal of Chemical Physics*, 128(18):10, 2008.

[8] Felix Studt, Frank Abild-Pedersen, Heine A. Hansen, Isabela C. Man, Jan Rossmeisl, and Thomas Bligaard. Volcano relation for the deacon process over transition-metal oxides. *CHEMCATCHEM*, 2(1):98–102, 2010.

[9] J. K. Norskov, T. Bligaard, J. Rossmeisl, and C. H. Christensen. Towards the computational design of solid catalysts. *Nature Chemistry*, 1(1):37–46, April 2009.

[10] Jens K. Norskov, Frank Abild-Pedersen, Felix Studt, and Thomas Bligaard. Density functional theory in surface chemistry and catalysis. *Proceedings of the National Academy of Sciences of the United States of America*, 108(3):937–943, January 2011.

[11] Matthew Neurock. Engineering molecular transformations for sustainable energy conversion. *Industrial & Engineering Chemistry Research*, 49(21):10183–10199, 2010.

[12] F. Abild-Pedersen, J. Greeley, F. Studt, J. Rossmeisl, T. R. Munter, P. G. Moses, E. Skulason, T. Bligaard, and J. K. Norskov. Scaling properties of adsorption energies for hydrogen-containing molecules on transition-metal surfaces rid a-5714-2011 rid a-6161-2011. *Physical Review Letters*, 99(1):016105, July 2007.

[13] G. Jones, T. Bligaard, F. Abild-Pedersen, and J. K. Norskov. Using scaling relations to understand trends in the catalytic activity of transition metals. *Journal of Physics-Condensed Matter*, 20(6), 2008.

[14] J. N. Bronsted. Acid and basic catalysis. *Chemical Reviews*, 5(3):231–338, September 1928.

[15] M. G. Evans and M. Polanyi. Inertia and driving force of chemical reactions. *Transactions of the Faraday Society*, 34(1):0011–0023, 1938.

[16] A. Logadottir, T. H. Rod, J. K. Norskov, B. Hammer, S. Dahl, and C. J. H. Jacobsen. The bronsted-evans-polanyi relation and the volcano plot for ammonia synthesis over transition metal catalysts. *Journal of Catalysis*, 197(2):229–231, January 2001.

[17] J. K. Norskov, T. Bligaard, A. Logadottir, S. Bahn, L. B. Hansen, M. Bollinger, H. Bengaard, B. Hammer, Z. Sljivancanin,

M. Mavrikakis, Y. Xu, S. Dahl, and C. J. H. Jacobsen. Universality in heterogeneous catalysis. *Journal of Catalysis*, 209(2):275–278, July 2002.

[18] Shengguang Wang, Burcin Temel, Juan Shen, Glenn Jones, Lars C. Grabow, Felix Studt, Thomas Bligaard, Frank Abild-Pedersen, Claus H. Christensen, and Jens K. Norskov. Universal bronsted-evans-polanyi relations for c-c, c-o, c-n, n-o, n-n, and o-o dissociation reactions. *Catalysis Letters*, 141(3):370–373, March 2011.

[19] T. Bligaard, J. K. Norskov, S. Dahl, J. Matthiesen, C. H. Christensen, and J. Sehested. The bronsted-evans-polanyi relation and the volcano curve in heterogeneous catalysis. *Journal of Catalysis*, 224(1):206–217, May 2004.

[20] H. Over, Y. D. Kim, A. P. Seitsonen, S. Wendt, E. Lundgren, M. Schmid, P. Varga, A. Morgante, and G. Ertl. Atomic-scale structure and catalytic reactivity of the ruo2(110) surface. *Science*, 287(5457):1474–1476, 2000.

[21] I. M. Lorkovic, A. Yilmaz, G. A. Yilmaz, X. P. Zhou, L. E. Laverman, S. L. Sun, D. J. Schaefer, M. Weiss, M. L. Noy, C. I. Cutler, J. H. Sherman, E. W. McFarland, G. D. Stucky, and P. C. Ford. A novel integrated process for the functionalization of methane and ethane: bromine as mediator. *Catalysis Today*, 98(1-2):317–322, 2004.

[22] A Breed, MF Doherty, S Gadewar, P Grosso, IM Lorkovic, EW McFarland, and MJ Weiss. Natural gas conversion to liquid fuels in a zone reactor. *CATALYSIS TODAY*, 106(1-4):301–304, OCT 15 2005.

[23] K.H. Büchel, H.-H. Moretto, and P. Woditsch, editors. *Industrial Inorganic Chemistry, 2nd Ed.* Wiley-VCH, 2000.

[24] H. Deacon. Us patent 165 802. 1875.

[25] K. Iwanaga, K. Seki, Y. Hibi, K. Issoh, T. Suzuta, M. Nakada, Y. Mori, and T. Abe. *Sumitomo Kagaku*, 1:4, 2004.

[26] Kohei Seki. Development of ruo(2)/rutile-tio(2) catalyst for industrial hcl oxidation process. *Catalysis Surveys from Asia*, 14(3-4):168–175, 2010.

[27] Nuria Lopez, Jordi Gomez-Segura, Raimon P. Marin, and Javier Perez-Ramirez. Mechanism of hcl oxidation (deacon process) over ruo2. *Journal of Catalysis*, 255(1):29–39, April 2008.

[28] Daniela Crihan, Marcus Knapp, Stefan Zweidingey, Edvin Lundgren, Cornelis J. Weststrate, Jesper N. Andersen, Ari P. Seitsonen, and Herbert Over. Stable deacon process for hcl oxidation over ruo2. *Angewandte Chemie-international Edition*, 47(11):2131–2134, 2008.

[29] S. Zweidinger, D. Crihan, M. Knapp, J. P. Hofmann, A. P. Seitsonen, C. J. Weststrate, E. Lundgren, J. N. Andersen, and H. Over. Reaction mechanism of the oxidation of hcl over ruo2(110). *Journal of Physical Chemistry C*, 112(27):9966–9969, July 2008.

[30] A. P. Seitsonen and H. Over. Oxidation of hcl over tio(2)-supported ruo(2): A density functional theory study. *Journal of Physical Chemistry C*, 114(51):22624–22629, 2010.

[31] Scott M. Auerbach. *Handbook of Zeolite Science and Technology*. CRC, 2003.

[32] R. Shah, J. D. Gale, and M. C. Payne. Methanol adsorption in zeolites - a first-principles study. *Journal of Physical Chemistry*, 100(28):11688–11697, 1996.

[33] J. Hafner, L. Benco, and T. Bucko. Acid-based catalysis in zeolites investigated by density-functional methods. *Topics in Catalysis*, 37(1):41–54, 2006.

[34] L. Benco, T. Bucko, J. Hafner, and H. Toulhoat. Periodic dft calculations of the stability of al/si substitutions and extraframework zn2+ cations in mordenite and reaction pathway for the dissociation of h-2 and ch4. *Journal of Physical Chemistry B*, 109(43):20361–20369, 2005.

[35] S. Svelle, C. Tuma, X. Rozanska, T. Kerber, and J. Sauer. Quantum chemical modeling of zeolite-catalyzed methylation reactions: Toward chemical accuracy for barriers. *Journal of the American Chemical Society*, 131(2):816–825, 2009.

[36] T. Bucko, L. Benco, and J. Hafner. Ab initio vibrational spectroscopy of molecular adsorbates in mordenite, 2005 2005.

[37] P. W. Atkins. *The elements of Physiscal Chemestry, Second edition.* Oxford University Press, 1996.

[38] M. C. Payne, M. P. Teter, D. C. Allan, T. A. Arias, and J. D. Joannopoulos. Iterative minimization techniques for *ab initio* total-energy calculations: molecular dynamics and conjugate gradients. *Reviews of Modern Physics*, 64:1045, 1992.

[39] W. Kohn. Nobel Lecture: Electronic structure of matter—wave functions and density functionals. *Reviews of Modern Physics*, 71:1253, 1999.

[40] F. Nogueira, A. Castro, and M. A. L. Marques. *A Tutorial on Density Functional Theory* in *A Primer in Density-Functional Theory.* Springer-Verlag Berlin Heidelberg, 2003.

[41] R. G. Parr and W. Yang. *Density-Functional Theory of Atoms and Molecules.* Oxford University Press, 1989.

[42] P. Hohenberg and W. kohn. Inhomogeneous Electron Gas. *Physical Review*, 136:B864, 1964.

[43] W. Kohn and L. J. Sham. Self-Consistent Equations Including Exchange and Correlation Effects. *Physical Review*, 140:A1133, 1965.

[44] R. O. Jones and O. Gunnarsson. The density functional formalism, its applications and prospects. *Reviews of Modern Physics*, 61:689, 1989.

[45] D. M. Ceperly and B. J. Alder. Ground state of the electron gas by a stochastic method. *Physical Review Letters*, 45:566, 1980.

[46] John P. Perdew, Kieron Burke, and Yue Wang. Generalized gradient approximation for the exchange-correlation hole of a many-electron system. *Physical Review B*, 54:16533, 1996.

[47] B. Hammer, L. B. Hansen, and J. K. Nørskov. Improved adsorption energetics within density-functional theory using revised Perdew-Burke-Ernzerhof functionals. *Physical Review B*, 59:7413, 1999.

[48] E.H. Lieb and S. Oxford. Improved lower bound on the indirect Coulomb energy. *International Journal of Quantum Chemistry*, 19:427, 1981.

[49] The dacapo plane wave/pseudopotential code is available as open source software at http://wiki.fysik.dtu.dk/dacapo.

[50] H. J. MONKHORST and J. D. PACK. Special points for brillouin-zone integrations. *Physical Review B*, 13(12):5188–5192, 1976.

[51] D. VANDERBILT. Soft self-consistent pseudopotentials in a generalized eigenvalue formalism. *Physical Review B*, 41(11):7892–7895, April 1990.

[52] G. Henkelman and H. Jónsson. Improved tangent estimate in the nudged elastic band method for finding minimum energy paths and saddle points. *Journal of Chemical Physics*, 113(22):2000, 2000.

[53] G. Henkelman, B. P. Uberuaga, and H. Jónsson. A climbing image nudged elastic band method for finding saddle points and minimum energy paths. *Journal of Chemical Physics*, 113(22):9901, 2000.

[54] M. P. Andersson, E. Abild-Pedersen, I. N. Remediakis, T. Bligaard, G. Jones, J. Engbwk, O. Lytken, S. Horch, J. H. Nielsen, J. Sehested, J. R. Rostrup-Nielsen, J. K. Norskov, and I. Chorkendorff. Structure sensitivity of the methanation reaction: H-2-induced co dissociation on nickel surfaces. *Journal of Catalysis*, 255(1):6–19, 2008.

[55] Eva M. Fernandez, Poul G. Moses, Anja Toftelund, Heine A. Hansen, Jose I. Martinez, Frank Abild-Pedersen, Jesper Kleis, Berit Hinnemann, Jan Rossmeisl, Thomas Bligaard, and Jens K. Norskov. Scaling relationships for adsorption energies on transition metal oxide, sulfide, and nitride surfaces. *Angewandte Chemie-international Edition*, 47(25):4683–4686, 2008.

[56] B. Hammer and J. K. Norskov. Why gold is the noblest of all the metals. *Nature*, 376(6537):238–240, 1995.

[57] B. Hammer and J. K. Norskov. Electronic factors determining the reactivity of metal surfaces. *Surface Science*, 343(3):211–220, 1995.

[58] B. Hammer and J. K. Norskov. Theoretical surface science and catalysis - calculations and concepts. *Advances in Catalysis, Vol 45: Impact of Surface Science on Catalysis*, 45:71–129, 2000.

[59] T. Bligaard and J. K. Norskov. Ligand effects in heterogeneous catalysis and electrochemistry. *Electrochimica Acta*, 52(18):5512–5516, 2007.

[60] J. K. Norskov and N. D. Lang. Effective-medium theory of chemical-binding - application to chemisorption. *Physical Review B*, 21(6):2131–2136, 1980.

[61] A. Vojvodic, A. Hellman, C. Ruberto, and B. I. Lundqvist. From electronic structure to catalytic activity: A single descriptor for adsorption and reactivity on transition-metal carbides. *Physical Review Letters*, 103(14):146103, October 2009.

[62] A. Vojvodic, F. Calle-Vallejo, W. Guo, S. Wang, A. Toftelund, F. Studt, J. I. Martinez, J. Shen, I. C. Man, J. Rossmeisl, T. Bligaard, J. K. Noorskov, and F. Abild-Pedersen. On the behavior of bronsted-evans-polanyi relations for transition metal oxides. *The Journal of chemical physics*, 134(24):244509, June 2011.

[63] P. Sabatier. Announcement. hydrogenation and dehydrogenation for catalysis. *Berichte Der Deutschen Chemischen Gesellschaft*, 44:1984–2001, 1911.

[64] M.W. Jr. Chase. *NIST-JANAF Themochemical Tables, 4th Ed., J. Phys. Chem. Ref. Data.* Monograph 9, 1998.

[65] P.W. Atkins and Julio de Paula. *Physical Chemistry, 8th Ed.* Oxford University Press, 2006.

[66] Jesper Kleis, Glenn Jones, Frank Abild-Pedersen, Vladimir Tripkovic, Thomas Bligaard, and Jan Rossmeisl. Trends for methane oxidation at solid oxide fuel cell conditions. *Journal of the Electrochemical Society*, 156(12):B1447–B1456, 2009.

[67] Hanne Falsig, Thomas Bligaard, Jeppe Rass-Hansen, Arkady L. Kustov, Claus H. Christensen, and Jens K. Norskov. Trends in catalytic no decomposition over transition metal surfaces. *Topics in Catalysis*, 45(1-4):117–120, 2007.

[68] Hanne Falsig, Thomas Bligaard, Claus H. Christensen, and Jens K. Norskov. Direct no decomposition over stepped transition-metal surfaces. *Pure and Applied Chemistry*, 79(11):1895–1903, 2007.

[69] Egon Wiberg, Nils Wiberg, and Arnold Frederick Holleman. *Inorganic Chemestry*. Academic Press, 2001.

[70] Isabela C. Man, Hai-Yan Su, Federico Calle-Vallejo, Heine A. Hansen, Jose I. Martinez, Nilay G. Inoglu, John Kitchin, Thomas F. Jaramillo, Jens K. Norskov, and Jan Rossmeisl. Universality in oxygen evolution electrocatalysis on oxide surfaces. *Chemcatchem*, 3(7):1159–1165, 2011.

[71] Gpaw grid base projector augmented-wave method dft code is available as open source sofware at wiki.fysik.dtu.dk/gpaw.

[72] Lars C. Grabow, Britt Hvolbaek, and Jens K. Norskov. Understanding trends in catalytic activity: The effect of adsorbate-adsorbate interactions for co oxidation over transition metals. *Topics in Catalysis*, 53(5-6):298–310, 2010.

[73] E. A. Guggenheim. Statistical thermodynamics of mixtures with zero energies of mixing. *Proceedings of the Royal Society of London Series a-Mathematical and Physical Sciences*, 183(A993):0203–0212, 1944.

[74] E. A. Guggenheim. Number of configurations of molecules occupying several sites. *Nature*, 153:406–407, 1944.

[75] E. A. Dimarzio. Statistics of orientation effects in linear polymer molecules. *Journal of Chemical Physics*, 35(2):658–&, 1961.

[76] P. Fejes, J. B. Nagy, K. Kovacs, and G. Vanko. Synthesis of tin(iv) silicalites (mfi) and their characterization - a mossbauer and mas nmr spectroscopy study. *Applied Catalysis a-General*, 145(1-2):155–184, 1996.

[77] Masanao Kato, Takuji Ikeda, Tetsuya Kodaira, and Shio Takahashi. Synthesis of co-substituted zeolites in the presence of cobalt complex with edma. *Microporous and Mesoporous Materials*, 142(2-3):444–453, 2011.

[78] G. J. Kim and W. S. Ahn. Synthesis and characterization of iron-modified zsm-5. *Applied Catalysis*, 71(1):55–68, 1991.

[79] Xin-Chun Lue, Rong Zhao, Tai-Liu Wu, Yao-Jun Sun, and Yi Tang. Synthesis and characterization of a novel framework zinc-substituted

mfi zeolite. *Chemical Journal of Chinese Universities-Chinese*, 32(3):494–496, 2011.

[80] Abdolraouf Samadi-Maybodi, Seyed Naser Azizi, S. Masoomeh Pourali, and Salma Ehsani Tilami. Framework-substituted bismuth zeolite-p: Synthesis and characterization. *Zeitschrift Fur Anorganische Und Allgemeine Chemie*, 638(1):214–219, 2012.

[81] W. Loewenstein. The distribution of aluminum in the tetrahedra of silicates and aluminates. *American Mineralogist*, 39(1-2):92–96, 1954.

[82] G. Engelhardt, D. Zeigan, E. Lippmaa, and M. Magi. On the distribution of silicon and aluminum atoms in the crystal-lattice of zeolites - an alternative structure of naa-type zeolites. *Zeitschrift Fur Anorganische Und Allgemeine Chemie*, 468(9):35–38, 1980.

[83] A. V. McCormick, A. T. Bell, and C. J. Radke. Multinuclear nmr investigation of the formation of aluminosilicate anions. *Journal of Physical Chemistry*, 93(5):1741–1744, 1989.

[84] A. V. McCormick, A. T. Bell, and C. J. Radke. Evidence from alkali-metal nmr-spectroscopy for ion-pairing in alkaline silicate solutions. *Journal of Physical Chemistry*, 93(5):1733–1737, 1989.

[85] R. F. Mortlock, A. T. Bell, and C. J. Radke. Incorporation of aluminum into silicate anions in aqueous and methanolic solutions of tma silicates. *Journal of Physical Chemistry*, 95(20):7847–7851, 1991.

[86] C. R. A. Catlow, A. R. George, and C. M. Freeman. Ab initio and molecular-mechanics studies of aluminosilicate fragments, and the origin of lowenstein's rule. *Chemical Communications*, (11):1311–1312, 1996.

[87] S. Thayaparam, V. Heine, M. T. Dove, and K. D. Hammonds. A computational study of al/si ordering in cordierite. *Physics and Chemistry of Minerals*, 23(2):127–139, 1996.

[88] M. T. Melchior, D. E. W. Vaughan, and A. J. Jacobson. Characterization of the silicon aluminum distribution in synthetic faujasites by high-resolution solid-state si-29 nmr. *Journal of the American Chemical Society*, 104(18):4859–4864, 1982.

[89] B. K. Peterson. Simulated annealing method for determining atomic distributions from nmr data: Silicon and aluminum in faujasite. *Journal of Physical Chemistry B*, 103(16):3145–3150, 1999.

[90] K. P. Schroder and J. C. Sauer. Preferred stability of al-o-si-o-al linkages in high-silica zeolite catalysts - theoretical predictions contrary to dempseys rule. *Journal of Physical Chemistry*, 97(25):6579–6581, 1993.

[91] T. Takaishi, M. Kato, and K. Itabashi. Stability of the al-o-si-o-al linkage in a zeolitic framework. *Journal of Physical Chemistry*, 98(22):5742–5743, 1994.

[92] M. Derewinski, P. Sarv, and A. Mifsud. Thermal stability and siting of aluminum in isostructural zsm-22 and theta-1 zeolites. *Catalysis Today*, 114(2-3):197–204, 2006.

[93] Stepan Sklenak, Jiri Dedecek, Chengbin Li, Fei Gao, Bavornpon Jansang, Bundet Boekfa, Blanka Wichterlova, and Joachim Sauer. Aluminum siting in the zsm-22 and theta-1 zeolites revisited: A qm/mm study. *Collection of Czechoslovak Chemical Communications*, 73(6-7):909–920, 2008.

[94] By correspondence with morten björgen from univ oslo, dept chem.

[95] J. L. G. Dealmeida, M. Dufaux, Y. B. Taarit, and C. Naccache. Effect of pore-size and aluminum content on the production of linear alkylbenzenes over hy, h-zsm-5 and h-zsm-12 zeolites - alkylation of benzene with 1-dodocene. *Applied Catalysis a-General*, 114(1):141–159, 1994.

[96] S. Bessell. Investigation of bifunctional zeolite-supported cobalt fischer-tropsch catalysts. *Applied Catalysis a-General*, 126(2):235–244, 1995.

[97] M. W. Simon, S. L. Suib, and C. L. Oyoung. Synthesis and characterization of zsm-22 zeolites and their catalytic behavior in 1-butene isomerization-reactions. *Journal of Catalysis*, 147(2):484–493, 1994.

[98] N. Kumar, L. E. Lindfors, and R. Byggningsbacka. Synthesis and characterization of h-zsm-22, zn-h-zsm-22 and ga-h-zsm-22 zeolite catalysts and their catalytic activity in the aromatization of n-butane. *Applied Catalysis a-General*, 139(1-2):189–199, 1996.

[99] R. J. Gorte. What do we know about the acidity of solid acids ? *Catalysis Letters*, 62(1):1–13, 1999.

Paper I

Scaling Relationships for Adsorption Energies on Transition Metal Oxide, Sulfide, and Nitride Surfaces

Eva M. Fernández, Poul G. Moses, Anja Toftelund, Heine A. Hansen, José I. Martínez, Frank Abild-Pedersen, Jesper Kleis, Berit Hinnemann, Jan Rossmeisl, Thomas Bligaard, and Jens K. Nørskov

Angew. Chem. Int. Ed. 2008, 47, 4683-4686

DOI: 10.1002/anie.200705739

Scaling Relationships for Adsorption Energies on Transition Metal Oxide, Sulfide, and Nitride Surfaces**

*Eva M. Fernández, Poul G. Moses, Anja Toftelund, Heine A. Hansen, José I. Martínez, Frank Abild-Pedersen, Jesper Kleis, Berit Hinnemann, Jan Rossmeisl, Thomas Bligaard, and Jens K. Nørskov**

There has been substantial progress in the description of adsorption and chemical reactions of simple molecules on transition-metal surfaces. Adsorption energies and activation energies have been obtained for a number of systems, and complete catalytic reactions have been described in some detail.[1–7] Considerable progress has also been made in the theoretical description of the interaction of molecules with transition-metal oxides,[8–19] sulfides,[20–25] and nitrides,[26–29] but it is considerably more complicated to describe such complex systems theoretically. Complications arise from difficulties in describing the stoichiometry and structure of such surfaces, and from possible shortcomings in the use of ordinary generalized gradient approximation (GGA) type density functional theory (DFT).[30]

Herein we introduce a method that may facilitate the description of the bonding of gas molecules to transition-metal oxides, sulfides, and nitrides. It was recently found that there are a set of scaling relationhips between the adsorption energies of different partially hydrogenated intermediates on transition-metal surfaces.[31] We will show that similar scaling relationships exist for adsorption on transition metal oxide, sulfide, and nitride surfaces. This means that knowing the adsorption energy for one transition-metal complex will make it possible to quite easily generate data for a number of other complexes, and in this way obtain reactivity trends.

The results presented herein have been calculated using self-consistent DFT. Exchange and correlation effects are described using the revised Perdew–Burke–Ernzerhof (RPBE)[32] GGA functional. It is known that GGA functionals give adsorption energies with reasonable accuracy for transition metals.[32,33] It is not clear, however, whether a similar accuracy can be expected for the oxides, sulfides, and nitrides, although there are examples of excellent agreement between DFT calculations and experiments, for example, with RuO_2 surfaces.[9] In our study we focused entirely on variations in the adsorption energies from one system to another, and we expected that such results would be less dependent than the absolute adsorption energies on the description of exchange and correlation.

For the nitrides, a clean surface and a surface with a nitrogen vacancy were studied. For MX_2-type oxides or sulfides, an oxygen- or sulfur-covered surface with an oxygen or sulfur vacancy was studied. The structures of the clean surface considered in the present work and their unit cells are shown in Figure 1. The adsorption energies given below are for the adsorbed species in the most stable adsorption site on the surface.

By performing calculations for a large number of transition-metal surfaces of different orientations,[31] it was found that the adsorption energy of intermediates of the type AH_x is linearly correlated with the adsorption energy of atom A (N, O, S) according to Equation (1):

$$\Delta E^{AH_x} = \gamma(x)\Delta E^{A} + \xi \quad (1)$$

Here the scaling constant is given to a good approximation by Equation (2) where x_{max} is the maximum number of H atoms that can bond to the central atom A ($x_{max} = 3$ for A = N, and $x_{max} = 2$ for A = O, S), that is, the number of hydrogen atoms that the central atom A would bond to in order to form neutral gas-phase molecules.

$$\gamma(x) = (x_{max} - x)/x_{max} \quad (2)$$

We have performed similar calculations for the adsorption of oxygen, sulfur, and nitrogen on a series of transition metal oxide, sulfide, and nitride surfaces (Figure 2). We find that scaling relationhips also exist for these systems, which are considerably more complex than the transition-metal surfaces. Such a correlation between the adsorption energies of O and OH has previously been found for the MO_2 oxides.[12] Furthermore, it can be seen that the scaling constant $\gamma(x)$ is given to a good approximation by the same expression [Eq. (2)] as for adsorption on the transition metals. We find that the mean absolute error (MAE) is lower than 0.19 eV for all the species considered here. The nitride surfaces present a poorer correlation than the others, mainly because TiN(100) is a clear outlier.

[*] Dr. E. M. Fernández, P. G. Moses, A. Toftelund, H. A. Hansen, J. I. Martínez, Dr. F. Abild-Pedersen, Dr. J. Kleis, Prof. J. Rossmeisl, Prof. T. Bligaard, Prof. J. K. Nørskov
Center for Atomic-scale Materials Design
Department of Physics, Technical University of Denmark
DK-2800 Lyngby (Denmark)
Fax: (+45) 4593-2399
E-mail: norskov@fysik.dtu.dk
Dr. B. Hinnemann
Haldor Topsøe A/S, Nymøllevej 55, DK-2800 Lyngby (Denmark)

[**] The Center for Atomic-scale Materials Design is funded by the Lundbeck Foundation. We wish to acknowledge additional support from the Danish Research Agency through grant 26-04-0047 and the Danish Center for Scientific Computing through grant HDW-0107-07.

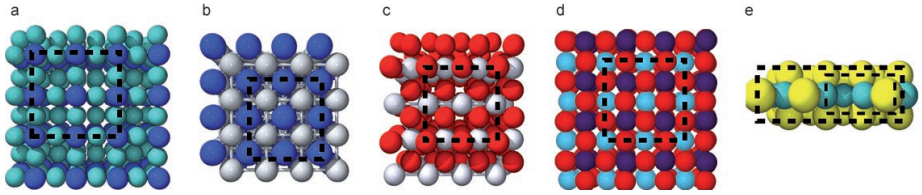

Figure 1. Structures used to describe the surfaces of the transition-metal nitrides, oxides and sulfides. a) Fcc-like structure for the M_2N (100) surface, M = Mo and W. Dark and light blue spheres represent metal and N atoms, respectively. b) Fcc-like rock-salt structure for the TiN (100) surface. Dark blue and gray spheres represent Ti and N atoms, respectively. c) Rutile-like (110) surface for the PtO_2 surface. Red and white spheres represent O and metal atoms, respectively. d) Perovskite structure for the $LaMO_3$ (100) surface, with M = Ti, Ni, Mn, Fe, and Co. Red, purple, and violet spheres represent O, La, and metal atoms, respectively. e) Hcp-like (−1010) surfaces for NbS_2, TaS_2, MoS_2, WS_2, Co-Mo-S, Ni-Mo-S, and Co-W-S. Yellow and green spheres represent S and metal atoms, respectively. The black dashed boxes indicate the unit cell.

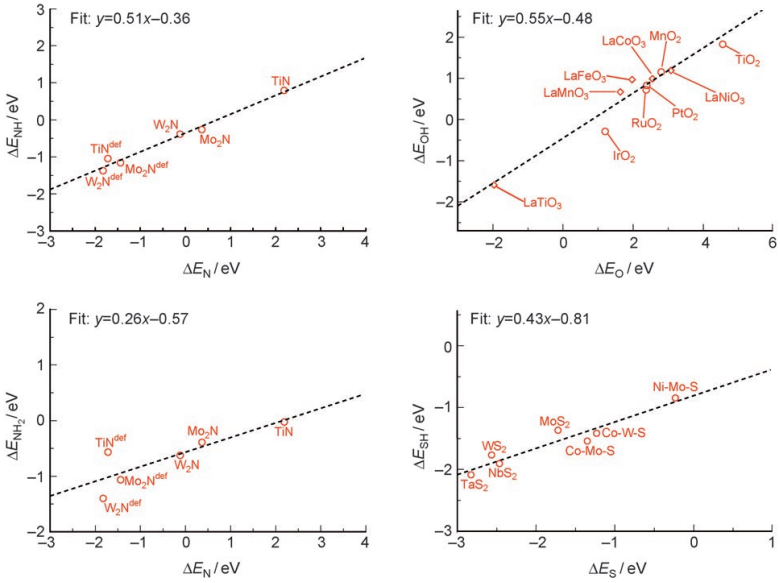

Figure 2. Adsorption energies of NH and NH_2 intermediates over nitrides, an OH intermediate over oxides, and an SH intermediate over sulfides plotted against adsorption energies of N over nitrides, O over oxides, and S over sulfides, respectively. The adsorption energy of AH_x is defined as: $\Delta E^{AH_x} = E(AH_x^*) + (x_{max} - x)/2\, E(H_2) - E(^*) - E(AH_{x_{max}})$ where $E(AH_x^*)$ is the total energy of an AH_x intermediate adsorbed on the most stable adsorption site, $E(^*)$ is the total energy of the surface without the A atom adsorbed, and $E(H_2)$ and $E(AH_{x_{max}})$ are the total energies of the hydrogen molecule and the $AH_{x_{max}}$ molecule in a vacuum, respectively.

It is interesting to compare the results of Figure 2 with the equivalent results for adsorption on the transition metals (Figure 3). It is found that the linear relationships for the nitrides are essentially the same for the two classes of systems. For the oxides, and partially for the sulfides, the results for the compounds are shifted from those on the transition metals. We trace this difference to a difference in the adsorption sites on the two kinds of systems. On the transition-metal surfaces, O and OH are generally found to coordinate with more than one metal neighbor. On the other hand, on the oxide surfaces the O atoms are generally coordinated to a single metal atom. If we use the adsorption energies for O and OH on the transition metals, where they are forced to adsorb in an on-top manner, the results now fall on the same line as for the oxides (Figure 3). For the sulfides, the S atom also adsorbs at a different site than on the transition metal. If the same adsorption site on the metal is considered the data agree, as for the oxides, with the results obtained for adsorption onto the sulfide surface.

The results of Figures 2 and 3 are remarkable and indicate that the nature of the adsorption bond is similar for the transition metals and the compounds. For the transition-metal surfaces, the scaling relationships can be understood within the d-band model.[34–39] The variation in adsorption energies for a given atom or molecule among the transition metals is mainly given by the variations in the strength of the coupling of the valence states of the adsorbate with the d states of the transition metal. The variations in the adsorption energy of an atom A from one transition-metal surface to the next reflect this. If H atoms are now added to atom A, the ability of A to couple to the metal d states decreases, either because the modified A states can couple to fewer d states or because the bonds become longer.[31] The principle of bond-order conservation would indicate that the weakening of the bond strength is proportional to the number of H atoms added, which corresponds to Equation (2).[31] The scaling behavior observed in Figures 2 and 3 indicates that similar arguments should hold for adsorption on transition-metal oxides, sulfides, and nitrides. The key to understanding this can be found in recent work by Ruberto and Lundqvist,[40] in which they show that a suitably modified d-band model can be used to understand trends in adsorption energies on transition-metal carbides and nitrides.

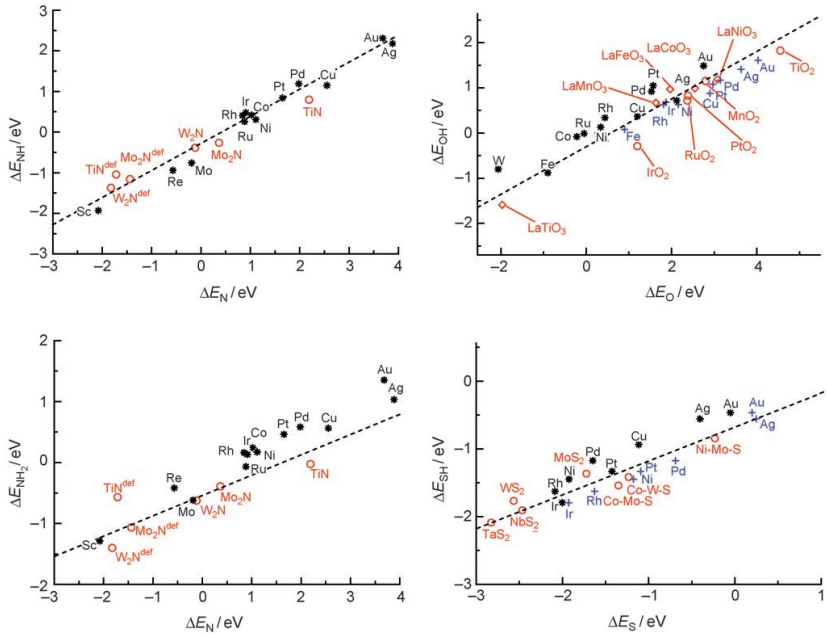

Figure 3. Adsorption energies of NH and NH_2 intermediates on transition metal nitride and transition-metal surfaces, the OH intermediate on transition metal oxide and transition metal surfaces, and the SH intermediate on transition metal sulfide and transition metal surfaces are plotted against the adsorption energies of N, O, and S, respectively. Close-packed surfaces for NH_x and OH_x intermediates, and the stepped surface for SH_x intermediates are considered. The adsorption energies for the OH intermediate on a top site and S intermediates on a bridge site over transition metal centers are included (blue points). The dashed line is the slope $\gamma(x)$ obtained from Equation (2).

The strength of the scaling relationships is shown by the following example. If one has a calculated or an experimental adsorption energy of an adsorbate AH_x ($\Delta E_{M1}^{AH_x}$) for one transition metal or transition-metal compound M1, we can estimate the energy $\Delta E_{M2}^{AH_x}$ of the same intermediate on another system M2 from the adsorption energies of atom A on the two systems, by using Equation (3).

$$\Delta E_{M2}^{AH_x} = \Delta E_{M1}^{AH_x} + \gamma(x)(\Delta E_{M2}^{A} - \Delta E_{M1}^{A}) \quad (3)$$

$\gamma(x)$ is a rational number given by Equation (2). If we have a database of atomic adsorption energies for a number of systems, we may then estimate the adsorption energy of a number of intermediates. This opens the possibility of obtaining an overview of adsorption energies on oxides, sulfides, and nitride surfaces on the basis of a few calculations.

In summary, density functional theory calculations on the adsorption of O, OH, S, SH, N, NH, and NH_2 on a range of transition metal oxide, sulfide, and nitride surfaces have been presented. It is shown that the adsorption energies ΔE^{AH_x} of AH_x intermediates scale with the adsorption energies ΔE^{A} of the A atoms according to the equation $\Delta E^{AH_x} = \gamma(x)\,\Delta E^{A} + \xi$, where the proportionality constant $\gamma(x)$ is independent of the metal and only depends on the number of H atoms in the molecule.

Experimental Section

The results presented herein were calculated using self-consistent DFT. The ionic cores and their interaction with the valence electrons are described by ultrasoft pseudopotentials (soft pseudopotential for S),[41] and the valence wave functions are expanded in a basis set of plane waves with a kinetic energy cut-off of 350–400 eV. The electron density of the valence states was obtained by a self-consistent iterative diagonalization of the Kohn–Sham Hamiltonian with Pulay mixing of the densities.[42] The occupation of the one-electron states was calculated using an electronic temperature of $k_B T = 0.1$ eV (0.01 eV for the molecules in a vacuum); all energies were extrapolated to $T = 0$ K. The ionic degrees of freedom were relaxed using the quasi-Newton minimization scheme, until the maximum force component was smaller than 0.05 eV Å^{-1}. Spin magnetic moments for the oxides, Co-Mo-S, Ni-Mo-S, and Co-W-S were taken into account. Exchange and correlation effects are described using the RPBE[32] GGA functional.

We used the periodic slab approximation, and the unit cells considered were modeled by a (2×2) unit cell for the nitrides and perovskite-type oxides, a (2×1) unit cell for PtO_2, a (2×1) unit cell for Co-W-S and MS_2 surfaces with M = Mo, Nb, Ta, and W, and a (4×1) unit cell for the M-Mo-S surface with M = Ni and Co. A four-layer slab for the nitrides and perovskite-type oxides, a four trilayer slab for PtO_2-type oxides, and an 8 or 12 layer slab for sulfides were employed in the calculations. Neighboring slabs were separated by more than 10 Å of vacuum. The results for the MO_2 surfaces with M = Ir, Mn, Ru, and Ti are taken from Refs. [12,15] The adsorbate together with the two topmost layers for the nitrides and perovskite-type oxides, the two topmost trilayers for MO_2 oxides, and all layers for the sulfides were allowed to fully relax. The Brillouin zone of the systems was sampled with a $4\times4\times1$ Monkhorst-Pack grid for the nitride and oxide surfaces and with a $6\times1\times1$ $(4\times1\times1)$ grid for the 2×1 (4×1) supercell of the sulfide surfaces.

Received: December 14, 2007
Revised: March 28, 2008
Published online: May 16, 2008

Keywords: adsorption · density functional calculations · surface chemistry · transition metals

[1] A. Alavi, P. Hu, T. Deutsch, P. L. Silvestrelli, J. Hutter, *Phys. Rev. Lett.* **1998**, *80*, 3650.
[2] A. Eichler, J. Hafner, *Phys. Rev.* **1999**, *59*, 5960.
[3] B. Hammer, *J. Catal.* **2001**, *199*, 171.

[4] A. Logadóttir, J. K. Nørskov, *J. Catal.* **2003**, *220*, 273.
[5] S. Linic, M. A. Barteau, *J. Am. Chem. Soc.* **2003**, *125*, 4034.
[6] S. Ovesson, B. I. Lundqvist, W. F. Schneider, A. Bogicevic, *Phys. Rev. B* **2005**, *71*, 115406.
[7] S. Kandoi, J. Greeley, M. A. Sanchez-Castillo, S. T. Evans, A. A. Gokhale, J. A. Dumesic, M. Mavrikakis, *Top. Catal.* **2006**, *37*, 17.
[8] S. Wendt, R. Schaub, J. Matthiesen, E. K. Vestergaard, E. Wahlström, M. D. Rasmussen, P. Thostrup, L. M. Molina, E. Lægsgaard, I. Stensgaard, B. Hammer, F. Besenbacher, *Surf. Sci.* **2005**, *598*, 226.
[9] K. Reuter K, D. Frenkel, M. Scheffler, *Phys. Rev. Lett.* **2004**, *93*, 116105.
[10] Y. Yanga, M. Sushchikha, G. Mills, H. Metiu, E. McFarland, *Appl. Surf. Sci.* **2004**, *229*, 346.
[11] S. Chrétien, H. Metiu, *Catal. Lett.* **2006**, *107*, 143.
[12] J. Rossmeisl, Z.-W. Qu, H. Zhu, G.-J. Kroes, J. K. Nørskov, *J. Electroanal. Chem.* **2007**, *607*, 83.
[13] M. D. Rasmussen, L. M. Molina, B. Hammer, *J. Chem. Phys.* **2004**, *120*, 988.
[14] Z. W. Qu, G. J. Kroes, *J. Phys. Chem. B* **2006**, *110*, 23306.
[15] J. Rossmeisl, K. Dimitrievski, P. Siegbahn, J. K. Nørskov, *J. Phys. Chem. C* **2007**, 111, 18821.
[16] T. Bredow, G. Pacchioni, *Chem. Phys. Lett.* **2002**, *79*, 753.
[17] M. Abu Halja, S. Guimond, Y. Romansyshyn, A. Uhi, H. Kulenbeck, T. K. Todorova, M. V. Ganduglia-Pirovano, J. Döbler, J. Sauer, H.-J. Freund, *Surf. Sci.* **2006**, *600*, 1497.
[18] G. Pacchioni, C. Di Valentini, D. Dominguez-Ariza, F. Illas, T. Bredow, T. Kluner, V. Staemmier, *J. Phys. Condens. Matter* **2004**, *16*, 2497.
[19] K. M. Neyman, S. P. Ruzankin, N. Rösch, *Chem. Phys. Lett.* **1995**, *246*, 546.
[20] M. Neurock, R. A. van Santen, *J. Am. Chem. Soc.* **1994**, *116*, 4427.
[21] S. Cristol, J.-F. Paul, E. Payen, D. Bougeard, S. Clémendot, F. Hutschka, *J. Phys. Chem. B* **2002**, *106*, 5659.
[22] M. Sun, A.-E. Nelson, J. Aadjaye, *J. Catal.* **2004**, *226*, 41.
[23] M. V. Bollinger, K. W. Jacobsen, J. K. Nørskov, *Phys. Rev. B* **2003**, *67*, 084310.
[24] H. Schweiger, P. Raybaud, H. Toulhat, *J. Catal.* **2002**, *212*, 33.
[25] T. Todorova, R. Prins, T. Weber, *J. Catal.* **2007**, *246*, 109.
[26] A. Vojvodic, C. Ruberto, B. I. Lundqvist, *Surf. Sci.* **2006**, *600*, 3619.
[27] P. Liu, J. A. Rodriguez, *Catal. Lett.* **2003**, *91*, 247.
[28] G. Frapper, M. Pélisser, *J. Phys. Chem. B* **2000**, *104*, 11972.
[29] J. Ren, C.-F. Huo, X.-D. Wen, Z. Cao, J. Wang, J.-W. Li, H. Jiao, *J. Phys. Chem. B* **2006**, *110*, 22563.
[30] O. Bengone, M. Alouani, P. Blöchl, J. Hugei, *Phys. Rev. B* **2000**, *62*, 16392.
[31] F. Abild-Pedersen, J. Greeley, F. Studt, J. Rossmeisl, T. R. Munter, P. G. Moses, E. Skúlason, T. Bligaard, J. K. Nørskov, *Phys. Rev. Lett.* **2007**, *99*, 016105.
[32] B. Hammer, L. B. Hansen, J. K. Nørskov, *Phys. Rev. B* **1999**, *59*, 7413.
[33] J. Greeley, M. Mavrikakis, *J. Phys. Chem. B* **2005**, *109*, 3460.
[34] B. Hammer, J. K. Nørskov, *Surf. Sci.* **1995**, *343*, 211.
[35] B. Hammer, J. K. Nørskov, *Nature* **1995**, *376*, 238 .
[36] B. Hammer, J. K. Nørskov, *Adv. Catal.* **2000**, *45*, 71.
[37] A. Eichler, F. Mittendorfer, J. Hafner, *Phys. Rev. B* **2000**, *62*, 4744.
[38] J. Greeley, M. Mavrikakis, *Nat. Mater.* **2004**, *3*, 810.
[39] A. Roudgar, A. Gross, *Phys. Rev. B* **2003**, *67*, 033409.
[40] C. Ruberto, B. I. Lundqvist, *Phys. Rev. B* **2007**, *75*, 235438.
[41] D. Vanderbilt, *Phys. Rev. B* **1990**, *41*, 1510.
[42] G. Kresse, J. Furthmuller, *Comput. Mater. Sci.* **1996**, *6*, 15.

Paper II

On the behavior of Brønsted-Evans-Polanyi relations for transition metal oxides

A. Vojvodic, F. Calle-Vallejo, W. Guo, S. Wang, A. Toftelund, F. Studt, J. I. Martínez, J. Shen, I. C. Man, J. Rossmeisl, T. Bligaard, J. K. Nørskov, and F. Abild-Pedersen

The Journal of Chemical Physics 134, 244509 (2011)

On the behavior of Brønsted-Evans-Polanyi relations for transition metal oxides

A. Vojvodic,[1,2] F. Calle-Vallejo,[2] W. Guo,[2] S. Wang,[2] A. Toftelund,[2] F. Studt,[1,2] J. I. Martínez,[2,3] J. Shen,[2] I. C. Man,[2] J. Rossmeisl,[2] T. Bligaard,[2] J. K. Nørskov,[1,2,4] and F. Abild-Pedersen[1,2,a)]

[1]*SUNCAT Center for Interface Science and Catalysis, SLAC National Accelerator Laboratory, 2575 Sand Hill Road, Menlo Park, California 94025, USA*

[2]*Center for Atomic-scale Materials Design, Department of Physics, Building 307, Technical University of Denmark, DK-2800 Kgs. Lyngby, Denmark*

[3]*Dpto. de Física Teórica de la Materia Condensada, Universidad Autónoma de Madrid, E-28049 Madrid, Spain*

[4]*Department of Chemical Engineering, Stanford University, Stanford, California 94305, USA*

(Received 15 March 2011; accepted 2 June 2011; published online 28 June 2011)

Versatile Brønsted-Evans-Polanyi (BEP) relations are found from density functional theory for a wide range of transition metal oxides including rutiles and perovskites. For oxides, the relation depends on the type of oxide, the active site, and the dissociating molecule. The slope of the BEP relation is strongly coupled to the adsorbate geometry in the transition state. If it is final state-like the dissociative chemisorption energy can be considered as a descriptor for the dissociation. If it is initial state-like, on the other hand, the dissociative chemisorption energy is not suitable as descriptor for the dissociation. Dissociation of molecules with strong intramolecular bonds belong to the former and molecules with weak intramolecular bonds to the latter group. We show, for the prototype system La-perovskites, that there is a "cyclic" behavior in the transition state characteristics upon change of the active transition metal of the oxide. © *2011 American Institute of Physics*. [doi:10.1063/1.3602323]

I. INTRODUCTION

Brønsted-Evans-Polanyi (BEP) relations[1,2] have recently been established quantitatively from density functional theory (DFT) calculations. Linear relations between activation energies and reaction energies or between transition state energies and dissociative chemisorption energies have been found for a number of surface reactions on different transition metal surfaces[3–11] and for a few transition metal compound systems.[12,13] Several reactions on transition metals are suggested to follow a universal BEP relation, that is, they obey a reactant independent but surface structure dependent linear relation.[4,6,10,14]

In spite of considerable progress,[15–22] theoretical understanding of the reactivity of transition metal oxides is less established than that of pure transition metals. The aim of this paper is to shed light on the reactivity of transition metal oxides. We will probe the reactivity of these materials by studying dissociation of small molecules on different oxide surfaces. First, we will investigate if the dissociative chemisorption energy can be used as a reactivity descriptor by searching for a correlation between this energy and the transition state energy, that is, if BEP relations exist for these classes of materials. When it comes to the reactivity of a surface, a more negative dissociative chemisorption energy corresponds to a more reactive system. For catalytic applications, the dissociative chemisorption energy should be neither too high nor too low, that is, the products should neither bind too strongly nor too weakly to the surface. Second, we will examine if a reactant independent BEP relation exists. When combined with scaling relations[23–25] the results of this paper will provide tools to establish activity and selectivity trends among oxide surfaces for heterogeneously catalyzed reaction as is currently established for a number of transition metal catalyzed reactions.[26] The main conclusions in this study are that BEP relations do exist for transition metal oxide surface reactions, and that they are strongly dependent on the bond properties of the dissociating molecules and the reactivity of the surface.

In the following we will show results for a number of different oxides. The oxides we have considered here can be divided in two subgroups: binary MO_2 oxides in the rutile structure and ternary oxides ABO_3 in the perovskite structure. In this study, the rutile surface under consideration is the (110) surface (see Fig. 1), which is found to be most stable.[27] For perovskites, the (001) surface can be either AO- or BO_2- terminated. Here, the BO_2-terminated perovskite surface is considered due to its higher stability.[28] Also, results on pure metal surfaces are presented for comparison. The different metal constituents in the oxides are M = Ti, Mo, Ru, Ir, Pt, and A = Sr, La, and B = Sc, Ti, V, Cr, Mn, Fe, Ru, Co, Ni, Cu. The chosen set of adsorbates is the homonuclear diatomic molecules H_2, N_2, O_2, Cl_2, Br_2, and I_2, the heteronuclear diatomic molecules and radicals NO, CO, HCl, HBr, HI, and OH, and the triatomic molecule H_2O. Dissociation is studied

a)Electronic mail: abild@slac.stanford.edu.

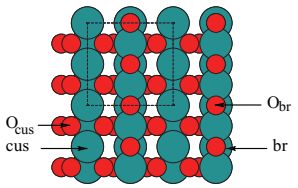

FIG. 1. Top view of the (110) rutile surface together with the different considered adsorption sites and the unit cell. Here, cus denotes the coordinately unsaturated site on top of a fivefold coordinated metal atom, the br denotes the bridge site between two fourfold coordinated metal atoms [note this corresponds to a (110) surface without O atoms], O_{br} denotes the site on top of a O in the bridge site, O_{cus} denotes the site on top of an O in the bridge site between two fivefold metal atoms.

not only on different oxide surfaces but also at different active sites for a given surface.

It should be noted, that while ordinary DFT calculations within the generalized gradient approximation (GGA) have proven to give reliable and reasonably accurate results for adsorption energies[29,30] on transition metals, similar calculations for oxides are fewer and not as well tested. However, there are several studies of oxides where a good agreement between DFT calculations and experiments exists.[27,31] Possible limitations and shortcomings of GGAs for oxides are a current research topic.[21,32–34] We caution that there may be cases where the DFT-GGA approach employed here is not sufficiently accurate but these issues will not be considered here. The present study is focusing on the variations in dissociation and transition state energies between different systems, and these will not be as sensitive to such accuracy issues as the absolute energies.

II. CALCULATION DETAILS

All calculations are performed using the plane wave DFT method as implemented in the DACAPO code.[29,35] The surfaces are modeled using slabs consisting of four stoichiometric layers in a 2×2 unit cell geometry. Repeated slabs are separated by a vacuum region of at least 15 Å (18 Å) for rutiles (perovskites). During structure relaxation, the topmost two layers are relaxed while the others are kept in the optimized bulk positions. The Kohn-Sham equations are solved using a basis set of plane waves with an energy (density) cutoff of 350–400 eV (500 eV) and the Brillouin zone is sampled with a $4\times4\times1$ Monkhorst-Pack grid. To describe the core electrons, the Vanderbilt ultrasoft pseudopotentials[36] are used. The exchange and correlation interactions are modeled with the RPBE functional[29] and the dipole correction is included according to the scheme in Ref. 37.

If not stated otherwise, both the dissociative chemisorption energies (ΔE_{diss}) and the transition state (TS) energies (ΔE_{TS}) are calculated relative to the gas phase diatomic molecule ($\Delta E_{diss} = E_{diss} - E_{surf} - E_{mol}$, $\Delta E_{TS} = E_{TS} - E_{surf} - E_{mol}$, where E_{diss} is the energy of the adsorbed dissociated molecule, E_{TS} is the energy of the adsorbed molecule in the transition state, E_{surf} is the energy of the clean surfaces, and E_{mol} is the energy of the molecule). The O_2 energy is calculated from H_2O and H_2[38] to avoid the well-known DFT error in the O_2 energy.[39] The transition state is determined by applying a fixed-bond length method, in which the energy at various bond lengths of the molecule are calculated while the remaining degrees of freedom of the system are completely relaxed. We note that for systems where the dissociation of the reactant occurs without an energy barrier the relations between ΔE_{TS} and ΔE_{diss} become undefined. To present the data for these systems we have chosen ΔE_{TS} as the highest energy point along the reaction pathway.

The adsorbate coverage in all systems is 1/4 ML relative to the number of metal atoms in the surface layer. In addition, the influence of the adsorbate–adsorbate interaction on the BEP relations is investigated by performing calculations of N_2 and NO on RuO_2 and PtO_2 in a 2×3 unit cell geometry corresponding to a 1/6 ML coverage. The results show that the BEP relations are not significantly affected by coverage effects. The absolute ΔE_{diss} and ΔE_{TS} energies are seen to change slightly, but with the same amount, hence preserving the BEP relation.

To test the accuracy of our approach we have compared the BEP relations obtained using RPBE with other GGA methods (PW91 and PBE). The dissociation of O_2 on TiO_2, RuO_2, and IrO_2 have been studied and we find that the relations are identical in terms of the slopes whereas the intercepts are slightly different for the three GGA's PBE having the largest intercept and RPBE having the smallest. We find that the ΔE_{diss} and ΔE_{TS} values shift by approximately the same energy amount upon change of GGA.

To justify that the stationary points on our potential energy surface obtained using a grid procedure indeed represent transition state geometries we have performed a vibrational analysis of O_2 on TiO_2, RuO_2, and IrO_2. In each case we find a single imaginary frequency hence identifying the geometry as a first order saddle-point.

In general, we do not expect large differences between zero-point energies on transition state geometries and final state (FS) geometries. To substantiate this assumption we have calculated the zero-point energies for O_2 on TiO_2, RuO_2, and IrO_2. Indeed the zero-point energies in the TS and the FS differ by less than 0.02 eV hence, in the following we will disregard this.

The effect of spin has been tested also for the O_2 dissociation on TiO_2, RuO_2, and IrO_2. When spin is included in the calculations it reduces to zero except in the case where the transition state is weakly bonded to the oxide (TiO_2). In this case the transition state is already maximally final state-like and hence per definition on the dissociation line.

III. RESULTS AND DISCUSSION

The general conclusion is that there exists a characteristic correlation between ΔE_{TS} and ΔE_{diss} for each molecule on a given dissociation site of an oxide or a metal. It is, however, not given *a priori* that one should be able to describe this correlation by a single linear relation given by

$$\Delta E_{TS} = \alpha \Delta E_{diss} + \beta. \quad (1)$$

From now on we will refer to a relation of this type as the averaged BEP relation. A fine-structure analysis of the

correlation shows that it, at least to a first order approximation, can be viewed as a collection of piecewise linear BEP relations.

We also find that each molecule follows its own BEP relation. This directly implies that the "universal" BEP relation only is valid as a very crude zeroth order approximation. However, for certain molecules and surfaces in a narrow energy region, the individual BEP relations are similar. It is only under such circumstances that a universal BEP relation is observed.

The averaged piecewise linear BEP relations are shown in Figs. 2, 3, and 6 while the linear fits for individual molecules are given in Table I. To simplify the discussion we divide the BEP relations in the following classes: (I) a single BEP line or (II) a collection of piecewise linear BEP lines (see Fig. 2). The latter can in turn be divided into two subclasses, defined by whether the BEP relation is a single- or multi-valued function of ΔE_{diss}, denoted as IIa) and IIb), respectively. In the following, the versatile nature of these correlations is discussed for different materials individually and then compared with each other.

A. Rutiles

For rutiles, the calculations reveal (see Fig. 2) unique BEP lines for each of the considered dissociation sites: cus–cus, br–br, br–cus, O_{cus}–cus, O_{br}–cus, O_{cus}–O_{cus}, and O_{br}–O_{br}. The notation of the dissociation site follows the geometry of the final state, see Fig. 1. For example, O_{cus}–cus denotes that one of the two molecule fragments is adsorbed on a O_{cus} site and the other one on a cus site.

Class I: We find that the br–br site, br–cus site, and the O_{cus}–O_{cus} site (see the respective subfigures in Fig. 2) belong to class I with a simple averaged BEP relation consisting of only one line. The slopes of the BEP lines depend on the active site ($\alpha_{br-br} = 0.75$, $\alpha_{br-cus} = 0.84$, and $\alpha_{O_{cus}-O_{cus}} = 0.14$).

The adsorbate geometry in the TS differs between the active sites. For the br–cus site, the bond length between the two molecular fragments in the TS is considerably elongated, which means that the adsorbed molecule has lost its molecular identity, and the TS geometry resembles the geometry of the FS. The TS geometry has more FS character the closer the point is to the dissociation line, defined by $\Delta E_{TS} = \Delta E_{diss}$.

For the O_{cus}–O_{cus} site, the bond length in the TS is close to the bond length of the free molecule. The TS geometry in the br–br site is less FS-like than the one of the br–cus site, and therefore $\alpha_{br-br} < \alpha_{br-cus}$. Hence, having a FS-like TS geometry results in a BEP line with a slope close to unity. The more initial state (IS)- like the TS geometry is, the larger the deviation from the dissociation line is leading to $\alpha \ll 1$. This in turn indicates that ΔE_{TS} is very weakly dependent on ΔE_{diss}, if at all.

Class IIa: The BEP relation for dissociation of H_2 on the O_{br}–O_{br} site can be classified as IIa (see the O_{br}–O_{br} subfigure in Fig. 2). One part of the BEP relation coincides with the dissociation line while the other part coincides with the association line, which corresponds to $\Delta E_{TS} = 0$. For the oxides on the dissociation (association) line the TS geometry is FS-like (IS-like). This illustrates that ΔE_{diss} is not a suitable descriptor.

Class IIb: The cus–cus and the O_{br}–cus sites (see the respective subfigure in Fig. 2) belong to class IIb. The averaged BEP relation consists of two parts, with slopes that coincide either with the slope of the dissociation line or with the slope of the association line. For a given ΔE_{diss} value, the resulting ΔE_{TS} can fall on either the association or the dissociation line. This implies that different molecules follow significantly different BEP lines. For the molecules on the averaged BEP line with $\alpha \sim 0$, ΔE_{TS} is independent of the ΔE_{diss}. This supports the finding of case IIa, that ΔE_{diss} is not a good descriptor for dissociation. From the geometrical investigation, we again find that the slope of the BEP line depends on whether the adsorbates TS geometry is FS-like, resulting in an α-value close to unity, or if it is IS-like, resulting in an α-value close to zero.

From the above analysis, the molecules can be divided into two groups: molecules with quite strong or very strong intramolecular bonds, for example, N_2, and very reactive molecules, for example, the diatomic homogeneous halide based molecules or diatomic heteronuclear weakly bond molecules containing halide atoms. In conclusion, the BEP relation is strongly dependent on the dissociating molecule.

For the dissociation of H_2O into OH and H over the O_{cus}–cus site (see the O_{cus}–cus subfigure in Fig. 2), when fitting the points to a straight line we find a BEP slope that is larger than one. Since $\alpha > 1$ is unphysical it is likely that the barrier for H_2O dissociation is overestimated on TiO_2 and that all transition state energies exactly follow the final state behavior, note the small energy scale on the y-axis.

We find that many molecules prefer to dissociate over the symmetric cus–cus site on a stoichiometric non-reduced MO_2 surface. This is presumably because of the completion of the octahedral geometry of the under-coordinated metal surface atoms on the clean surface. Nevertheless, the heteronuclear diatomic molecules that contain H prefer the asymmetric O_{br}–cus site, where the H recombines with O.

Comparing sites where only surface metal atoms are involved in the dissociation, i.e., the cus–cus, br–br, br–cus site, one finds that for a given adsorbate, the magnitude of the slopes of the BEP relations can be ordered as $\alpha_{br-br} < \alpha_{br-cus} < \alpha_{cus-cus}$. This illustrates that the BEP slope depends on the active site and that the α-values can be extrapolated. On a bridge site each adsorbate atom interacts with two fourfold coordinated surface metal atoms, while on the cus site each adsorbate atom interacts only with one fivefold surface metal atom. Hence, the bridge site, which resembles a vacancy site, is highly under-coordinated and, therefore, substantially more reactive than the cus site. The BEP slope is smallest for br–br since the surface atoms are more reactive and the intramolecular bonds will break more easily, resulting in a TS geometry that is less FS-like. Hence, the dissociation is favorable on a reduced surface where the br-sites are free to take part in the reaction.

For some molecules, e.g., N_2 on metal surfaces it has been shown that there is a geometric effect influencing the form of the BEP relation.[6,40] One could talk about such an effect for the br–br site, which has a significantly different geometry than the rest of the considered active sites. Another

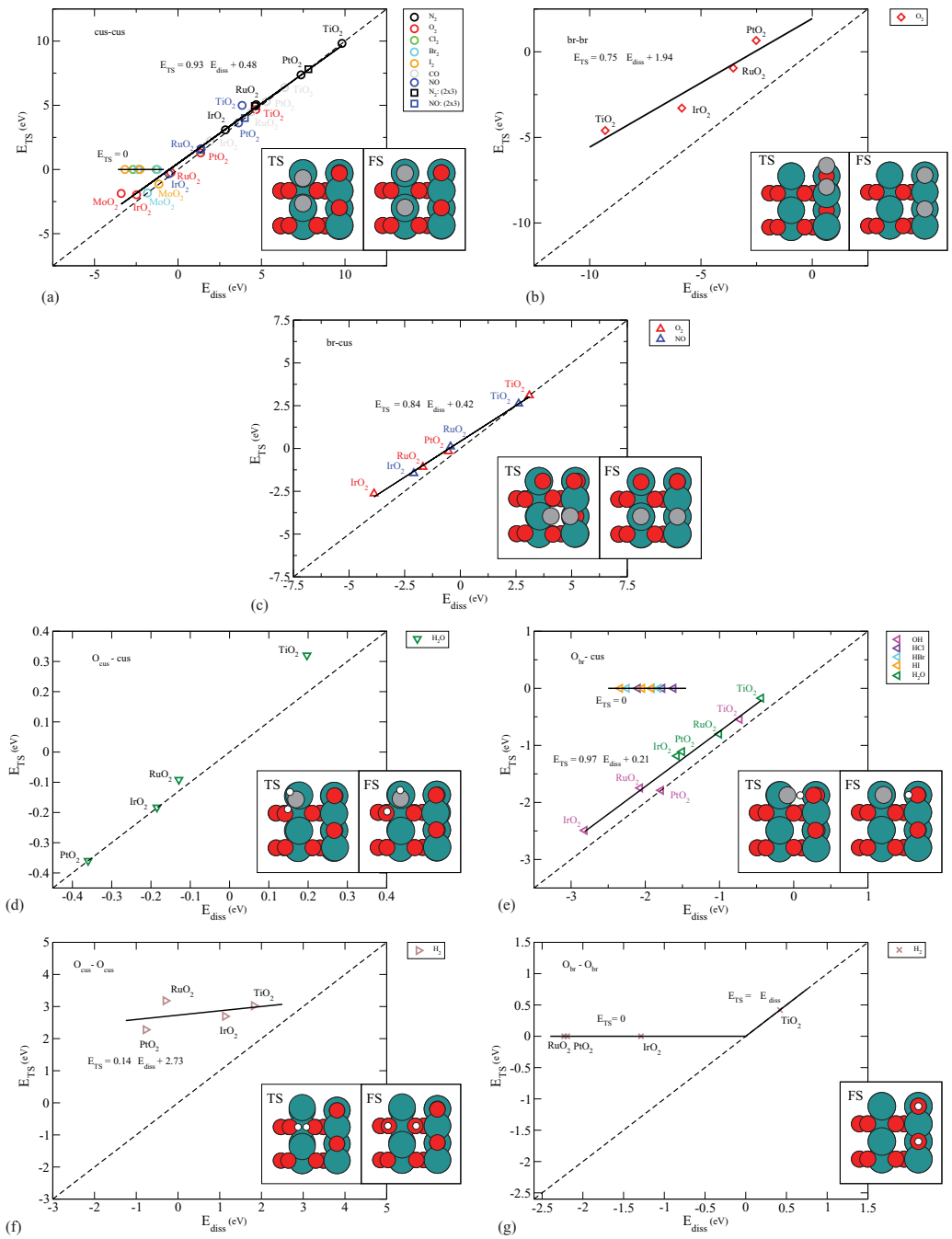

FIG. 2. Calculated transition state energy ΔE_{TS} as a function of dissociative chemisorption energy ΔE_{diss} of diatomic molecules on rutile (110) surfaces. The dissociation site is indicated in each panel. The solid black line represents the averaged BEP linear fit to the calculated data. The dashed line illustrates the dissociation line, i.e., $\Delta E_{TS} = \Delta E_{diss}$. Also, a top view of the structures for the TS and the dissociated state, that is, FS, are shown for a representative system. The blue, red, gray, and white spheres represent Ru, O, adsorbate O, and adsorbate H atoms, respectively.

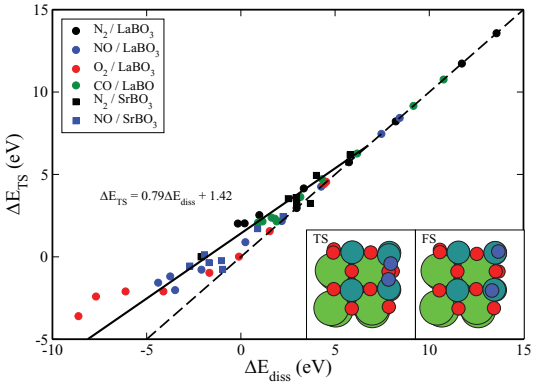

FIG. 3. Same as in Fig. 2 but for the (100) perovskite surfaces.

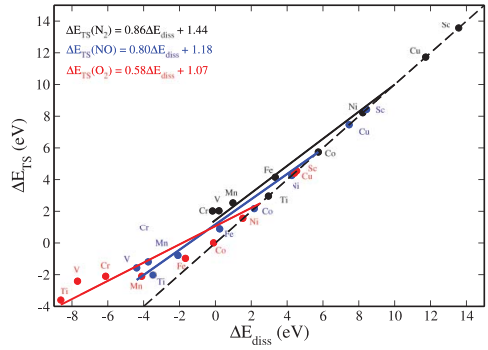

FIG. 4. Individual averaged BEP relations for N_2, NO, and O_2 on $LaBO_3$. The labels indicate the B metal of $LaBO_3$.

site where the BEP line experiences a rigid shift away from the dissociation line is the O_{br}–cus site. This should be compared with the cus–cus site. Dissociation over these two active sites involves the same amount of surface atoms, however, these surface atoms have different coordination and consist of different atomic species. Hence, there is no straightforward one-to-one correspondence between the geometry of the active site and the α-value for the oxides.

In conclusion, the BEP relations for rutiles show a delicate interplay between the type of molecule and the electronic structure of the active site in the conformation of the TS.

B. Perovskites

Figure 3 shows the results for the (100) surfaces of La- and Sr-perovskites. Also for this group of oxides BEP relations exist with an averaged relation given by $\Delta E_{TS} = 0.79\Delta E_{diss} + 1.42$ eV on a zoomed out level. However, the individual relations for each adsorbate and perovskite group (see Table I) show that different adsorbates obey their own BEP relations. In other words, the universal relation for perovskites is insufficient to describe the fine-structure behavior of the dissociation barriers.

The considered adsorption site on perovskites is atop of the surface B atoms, which leads to a locally fully coordinated structure around the surface B atom (see inset in Fig. 3). For the perovskites adopting or being very close to the ideal cubic symmetry, the relaxed adsorbate geometry is where the two atoms in the adsorbed molecule are positioned symmetrically atop of the B surface atoms. Otherwise, the adsorbate geometry gets skewed due to tilting of the octahedral framework.

When it comes to the transition state geometries, the perovskites on or in the close proximity of the dissociation line have FS-like geometries. In Sec. III C, the character of the TS will be discussed in more detail.

C. Transition state character: La-perovskites

To study the variations in character of the TS, we here consider dissociation of N_2, NO, and O_2 on $LaBO_3$ perovskites with different B metal atoms belonging to the 3*d* metals. First of all for each molecule the BEP relation (see Fig. 4) approaches the dissociation line for high ΔE_{diss} values and deviates from the dissociation line as the ΔE_{diss} becomes more negative. The α-values change as 0.86, 0.80, and 0.58 for N_2, NO, and O_2, respectively.

Second, if the reactivity of an oxide would depend solely on the position of the B metal atom constituent in the periodic table, the reactivity trend should be monotonous along a period. The situation is, however, more complicated, for example, the reactivity of the $LaBO_3$ perovskites for N_2 dissociation is $LaScO_3 < LaCuO_3 < LaNiO_3 < LaCoO_3 < LaFeO_3 < LaTiO_3 < LaMnO_3 < LaVO_3 < LaCrO_3$.

In Fig. 5, the calculated potential energy along the dissociation path is given for each adsorbate. For a given molecule, the character of the TS changes upon change of the substrate, in other words as the B constituent of ABO_3 changes. The TS character can be either IS-like, FS-like, or somewhere in-between. For N_2, the TS is FS-like on $LaCuO_3$, and it becomes less FS-like and more IS-like as the B metal is changed from Ni to Cr. The TS character has most IS-character when N_2 is dissociated on $LaCuO_3$. As the B metal is changed from V to Sc the TS character changes and becomes more FS-like. Similar results are found for NO and O_2, with the difference that the turning points are found for different B metals in the perovskites.

The conclusion is that when moving in the 3*d* series from Cu to Sc, the TS goes through a "cycle" from being FS-like (like B = Cu), where the points fall on the dissociation line, to IS-like (like B = Fe), and becoming FS-like (like B = Sc), falling back on the dissociation line. Compounds with the most IS-like character are located to the left of the BEP lines and, therefore, deviate the most from the dissociation line. There is no reason not to believe that this "cyclic" behavior should be valid for substrates with B metals with other group numbers outside the studied range. It is also this cyclic behavior that is responsible for non monotonous reactivity order of the La-perovskites.

D. Metals

In Fig. 6, we present some data for dissociation on the (211) and (111) metal surfaces for comparison. The BEP

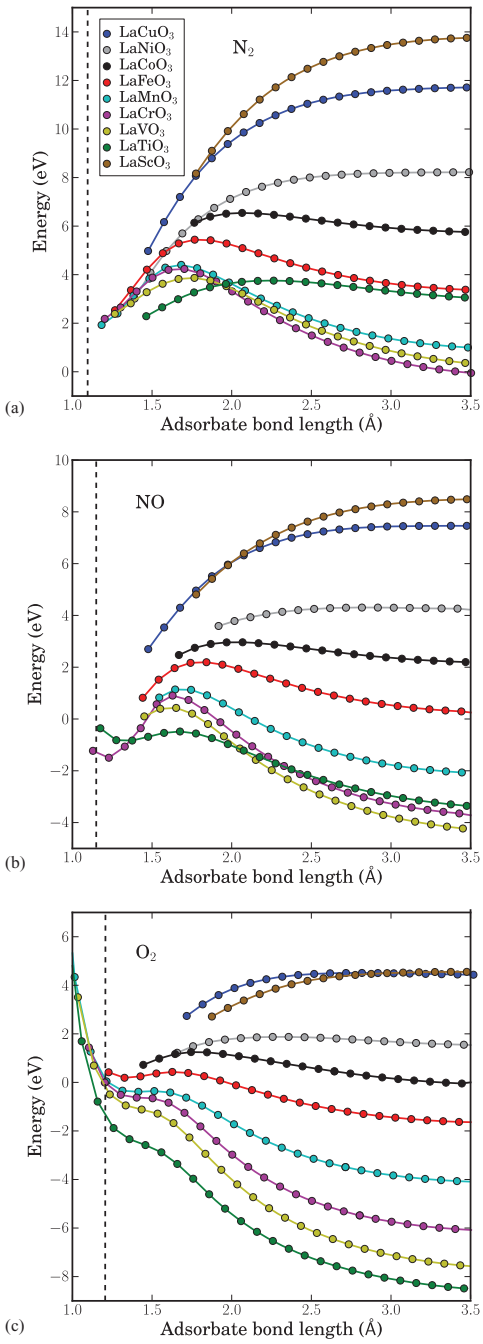

FIG. 5. Calculated adsorption energy of the molecule as a function of the molecular bond length for N_2, NO, and O_2 on La-perovskite (100) surfaces. The vertical dashed line indicates the bond length of the molecule in the gas phase.

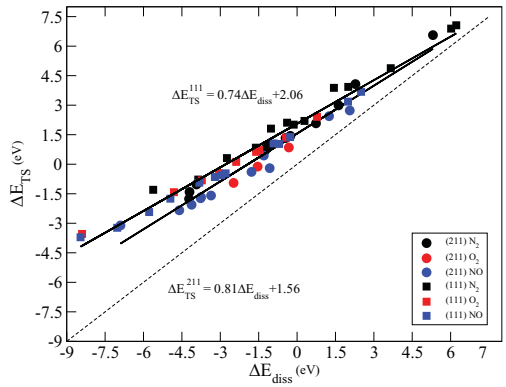

FIG. 6. Same as in Fig. 2 but for the (211) and the (111) transition metal surfaces.

relations for the lowest TS barriers can be characterized as class I, with the averaged relations given by $\Delta E_{TS} = 0.81\Delta E_{diss} + 1.56$ eV and $\Delta E_{TS} = 0.75\Delta E_{diss} + 2.06$ eV for the (211) and (111) surfaces, respectively. They are in agreement with the relations from Ref. 6, $\Delta E_{TS} = 0.87\Delta E_{diss} + 1.34$ eV and $\Delta E_{TS} = 0.90\Delta E_{diss} + 2.07$ eV, for the (211) and (111) surfaces, respectively. The difference in the relations found in the current study and the one in Ref. 6 is assigned to the somewhat different composition of the calculated data points on which the linear regressions are made. In the current study, metal surfaces in a broader reactivity range are included. Including more reactive metals, that is more negative ΔE_{diss}, results in a larger deviation from the dissociation line. The individual fits for each adsorbate on these surfaces are given in Table I. It is found that O_2 has an α-value that is substantially different from the averaged BEP α-value. This implies that there is a significant fine structure in the BEP relation for both transition metals as well as for oxides.

E. Oxides vs metals

When comparing the BEP relations associated with the lowest TS for metals and oxides, we find (considering the N_2, O_2, and NO molecules) that both groups of oxides obey relations that are closer to the dissociation line than the (111) and (211) metal surfaces. The rutiles have very low (if any) barriers with respect to the gas phase, while the perovskites exhibit more pronounced barriers. The averaged α-value for the perovskites is in-between the α-value of the (111) and the (211) surfaces, whereas the averaged β-value is closer to the β-value of the (211) surfaces. Hence, there is a major difference between the two types of oxides. The fact that molecules with strong or moderate intramolecular bonds dissociate without any substantial barriers on rutiles, make these oxides extremely interesting as catalysts for dissociation of diatomic molecules compared to the metals. In the energy region most relevant for catalysis, i.e., where $\Delta E_{diss} \sim 0$ eV, we find rutiles as RuO_2 and IrO_2.

TABLE I. Linear relations between ΔE_{TS} and ΔE_{diss} values for the considered systems. For each individual fit the α- and β-values (see Eq. (1)) are given together with the mean absolute error (MAE). Note that there are (to a zeroth order approximation) several BEP lines for some systems, see text for more details.

Rutile	Molecule	α	β (eV)	MAE (eV)
cus–cus	N_2	0.95	0.46	0.08
	O_2	0.84	0.42	0.35
	NO	1.10	0.18	0.32
	CO	0.93	0.42	0.03
	All	0.93	0.48	0.25
	Cl_2	0	0	0
	Br_2	0	0	0
		1.0	0	0
	I_2	0	0	0
		1.0	0	0
br–br	O_2	0.75	1.94	0.53
br–cus	O_2	0.83	0.40	0.13
	NO	0.86	0.40	0.06
	All	0.84	0.42	0.10
O_{cus}–cus	H_2O	1.30	0.07	0.02
O_{br}–cus	OH	0.92	0.06	0.10
	H_2O	0.87	0.16	0.05
	All	0.97	0.21	0.09
	HCl	0	0	0
	HBr	0	0	0
	HI	0	0	0
O_{cus}–O_{cus}	H_2	0.14	2.73	0.27
O_{br}–O_{br}	H_2	0	0	0
		1.0	0	0
Perovskite				
$LaBO_3$	N_2	0.86	1.44	0.46
	O_2	0.58	1.07	0.72
	NO	0.80	1.18	0.50
	CO	0.91	0.85	0.19
$SrBO_3$	N_2	0.75	1.40	0.39
	NO	0.65	0.82	0.40
	All	0.79	1.42	0.65
Metal				
(211)	N_2	0.83	1.85	0.20
	O_2	0.58	0.89	0.26
	NO	0.71	1.09	0.29
	All	0.81	1.56	0.36
(111)	N_2	0.74	2.36	0.23
	O_2	0.64	1.69	0.09
	NO	0.68	1.66	0.15
	All	0.74	2.06	0.31

IV. SUMMARY AND OUTLOOK

In summary, density functional theory calculations show that BEP relations also exist for oxides and that they have a richly detailed structure. Among the molecules and oxides investigated in this study, one finds the whole spectrum of BEP relations with slopes from one to almost zero. A slope equal to zero corresponds to a system with no activation barrier and hence the ΔE_{TS} by definition is not a well defined quantity. Surprisingly, we have found that the BEP relations for molecules with strong intramolecular bonds on the most stable site on rutiles follow a relation that almost coincides with the dissociation line. This suggests that these oxides are interesting as alternative catalysts for reactions involving the dissociation of diatomic molecules compared to transition metals. The perovskites could also be interesting for some reactions, since with respect to their dissociative abilities they intrinsically resemble the steps on transition metals.

Our results show that if the underlying nature of bonding in the TS and the dissociated state are similar, that is the TS is FS-like, these are correlated via a BEP relation with a slope close to unity. This is the case for molecules with strong intramolecular bonds. On the other hand, if the TS is more IS-like the BEP relations become FS-independent and the dissociative chemisorption energy becomes an invalid descriptor for the dissociation barrier. This is the case for very reactive surfaces or molecules with weak intramolecular bonds. We have identified a "cyclic" behavior in the TS character, that is it can change from being FS to IS and back to FS as the metal constituent of the oxide is varied through a period in the periodic table. This implies that on a detailed level the concept of universal BEP relation is an insufficient model unable to take into account the fine-structure observed in this study.

It is also found that, for a given molecule and active site, the BEP relation is a continuous function that depends on the strength of the bond formed between the surface and the molecule. At the moment we do not have a completely predictive approach of what the form of the BEP relation should look like, but we know that it to a good approximation can be viewed as a piecewise linear relation. This will be the subject of future studies.

The combined knowledge of BEP relations and scaling relations opens up the possibility to evaluate the activity of oxides in terms of simplified descriptors. Hence, extending the fundamental knowledge of the reaction chemistry at the atomic level may widen our perspectives of oxides as future heterogeneous catalysts.

ACKNOWLEDGMENTS

A.V., F.S., J.K.N., and F.A.-P. wish to acknowledge support from the (U.S.) Department of Energy (DOE), Office of Basic Energy Sciences. The Catalysis for Sustainable Energy (CASE) initiative is funded by the Danish Ministry of Science, Technology and Innovation. CAMD is funded by the Lundbeck foundation. The authors acknowledge support from the Danish Center for Scientific Computing. F.C.V. acknowledges support from the Danish Council for Strategic Research, via the Science and Engineering Research Council (SERC) project, through grant no. 2104-06-0011. J.I.M. acknowledges funding from Spanish MICINN through Juan de la Cierva Program.

[1] J. N. Brønsted, Chem. Rev. **5**, 231 (1928).
[2] M. G. Evans and M. Polanyi, Trans. Faraday Soc. **34**, 11 (1938).
[3] V. Pallassana and M. Neurock, J. Catal. **191**, 301 (2000).
[4] A. Logadóttir, T. H. Rod, J. K. Nørskov, B. Hammer, S. Dahl, and C. J. H. Jacobsen, J. Catal. **197**, 229 (2001).
[5] Z.-P. Liu and P. Hu, J. Chem. Phys. **114**, 8244 (2001).
[6] J. K. Nørskov, T. Bligaard, A. Logadóttir, S. Bahn, L. B. Hansen, M. Bollinger, H. Bengaard, B. Hammer, Z. Sljivancanin, M. Mavrikakis, Y. Xu, S. Dahl, and C. J. H. Jacobsen, J. Catal. **209**, 275 (2002).

[7]A. Michaelides, Z.-P. Liu, C. J. Zhang, A. Alavi, D. A. King, and P. Hu, J. Am. Chem. Soc. **125**, 3704 (2003).
[8]H. Falsig, B. Hvolbæk, I. S. Kristensen, T. Jiang, T. Bligaard, C. H. Christensen, and J. K. Nørskov, Angew. Chem. Int. Ed. **47**, 4835 (2008).
[9]P. Crawford, B. McAllister, and P. Hu, J. Phys. Chem. C **113**, 5222 (2009).
[10]S. Wang, B. Temel, J. Shen, G. Jones, L. C. Grabow, F. Studt, T. Bligaard, F. Abild-Pedersen, C. H. Christensen, and J. K. Nørskov, Catal. Lett. **141**, 370 (2010).
[11]S. Wang, V. Petzold, V. Tripkovic, J. Kleis, J. G. Howalt, E. Skúlason, E. Fernandez, B. Hvolbæk, G. Jones, A. Toftelund, H. Falsig, M. Björketun, F. Studt, F. Abild-Pedersen, J. Rossmeisl, J. K. Nørskov, and T. Bligaard, "Universal transition state scaling relations for hydrogenation and dehydrogenation reactions over transition metals," Phys. Chem. Chem. Phys. (submitted).
[12]A. Vojvodic, A. Hellman, C. Ruberto, and B. I. Lundqvist, Phys. Rev. Lett. **103**, 146103 (2009).
[13]F. Studt, F. Abild-Pedersen, H. A. Hansen, I. C. Man, J. Rossmeisl, and T. Bligaard, ChemCatChem **2**, 98 (2010).
[14]T. Bligaard, J. K. Nørskov, S. Dahl, J. Matthiesen, C. H. Christensen, and J. Sehested, J. Catal. **224**, 206 (2004).
[15]V. Shapovalov and H. Metiu, J. Catal. **245**, 205 (2007).
[16]S. Chretien and H. Metiu, Catal. Lett. **107**, 143 (2006).
[17]M. V. Ganduglia-Pirovano, A. Hofmann, and J. Sauer, Surf. Sci. Rep. **62**, 219 (2007).
[18]A. Michalak, M. Witko, and K. Hermann, Surf. Sci. **375**, 385 (1997).
[19]C. Loschen, J. Carrasco, K. M. Neyman, and F. Illas, Phys. Rev. B **75**, 035115 (2007).
[20]J. Carrasco, N. Lopez, and F. Illas, Phys. Rev. Lett. **93**, 225502 (2004).
[21]G. Pacchioni, J. Chem. Phys. **128**, 182505 (2008).
[22]H.-Y. Li, Y.-L. Guo, Y. Guo, G.-Z. Lu, and P. Hu, J. Chem. Phys. **128**, 051101 (2008).
[23]F. Abild-Pedersen, J. Greeley, F. Studt, J. Rossmeisl, T. R. Munter, P. G. Moses, E. Skúlason, T. Bligaard, and J. K. Nørskov, Phys. Rev. Lett. **99**, 016105 (2007).
[24]J. Rossmeisl, Z. W. Qu, H. Zhu, G. J. Kroes, and J. K. Nørskov, J. Electroanal. Chem. **607**, 83 (2007).
[25]E. M. Fernández, P. G. Moses, A. Toftelund, H. A. Hansen, J. I. Martínez, F. Abild-Pedersen, J. Kleis, B. Hinnemann, J. Rossmeisl, T. Bligaard, *et al.*, Angew. Chem. Int. Ed. **47**, 4683 (2008).
[26]J. Nørskov, F. Abild-Pedersen, F. Studt, and T. Bligaard, Proc. Natl. Acad. Sci. U.S.A. **108**, 937 (2011).
[27]K. Reuter and M. Scheffler, Phys. Rev. B **65**, 035406 (2001).
[28]M. A. Peña and J. L.G. Fierro, Chem. Rev. **101**, 1981 (2001).
[29]B. Hammer, L. B. Hansen, and J. K. Nørskov, Phys. Rev. B **59**, 7413 (1999).
[30]J. Greeley and M. Mavrikakis, J. Phys. Chem. **109**, 3460 (2005).
[31]J. I. Martínez, H. A. Hansen, J. Rossmeisl, and J. K. Nørskov, Phys. Rev. B **79**, 045120 (2009).
[32]L. Wang, T. Maxisch, and G. Ceder, Phys. Rev. B **73**, 195107 (2006).
[33]S. Kümmel and L. Kronik, Rev. Mod. Phys. **80**, 3 (2008).
[34]R. M. Nieminen, Modell. Simul. Mater. Sci. Eng. **17**, 084001 (2009).
[35]S. R. Bahn and K. W. Jacobsen, Comput. Sci. Eng. **4**, 56 (2002).
[36]D. Vanderbilt, Phys. Rev. B **41**, 7892 (1990).
[37]L. Bengtsson, Phys. Rev. B **59**, 12301 (1999).
[38]J. K. Nørskov, J. Rossmeisl, A. Logadóttir, L. Lindqvist, J. Kitchin, T. Bligaard, and H. Jónsson, J. Phys. Chem. B **108**, 17886 (2004).
[39]S. Kurth, J. P. Perdew, and P. Blaha, Int. J. Quantum Chem. **75**, 889 (1999).
[40]J. K. Nørskov, T. Bligaard, B. Hvolbæk, F. Abild-Pedersen, I. Chorkendorff, and C. H. Christensen, Chem. Soc. Rev. **37**, 2163 (2008).

Paper III

Universal transition state scaling relations for (de)hydrogenation over transition metals

S. Wang, V. Petzold, V. Tripkovic, J. Kleis, J. G. Howalt, E. Skúlason, E. M. Fernández, B. Hvolbæk, G. Jones, A. Toftelund, H. Falsig, M. Björketun, F. Studt, F. Abild-Pedersen, J. Rossmeisl, J. K. Nørskov and T. Bligaard

Phys. Chem. Chem. Phys., 2011, 13, 20760-20765

PCCP

Cite this: *Phys. Chem. Chem. Phys.*, 2011, **13**, 20760–20765

www.rsc.org/pccp

PAPER

Universal transition state scaling relations for (de)hydrogenation over transition metals†

S. Wang,[a] V. Petzold,[a] V. Tripkovic,[a] J. Kleis,[a] J. G. Howalt,[ab] E. Skúlason,[ac] E. M. Fernández,[a] B. Hvolbæk,[a] G. Jones,[a] A. Toftelund,[a] H. Falsig,[a] M. Björketun,[a] F. Studt,[d] F. Abild-Pedersen,[d] J. Rossmeisl,[a] J. K. Nørskov[de] and T. Bligaard*[a]

Received 28th February 2011, Accepted 21st September 2011
DOI: 10.1039/c1cp20547a

We analyse the transition state energies for 249 hydrogenation/dehydrogenation reactions of atoms and simple molecules over close-packed and stepped surfaces and nanoparticles of transition metals using Density Functional Theory. Linear energy scaling relations are observed for the transition state structures leading to transition state scaling relations for all the investigated reactions. With a suitable choice of reference systems the transition state scaling relations form a universality class that can be approximated with one single linear relation describing the entire range of reactions over all types of surfaces and nanoclusters.

1. Introduction

Linear energy relations have proven useful in simplifying the theoretical analysis of a number of catalytic reactions, thereby helping to establish an improved understanding of their underlying trends.[1–3] The linear energy relations in question are especially the so-called Brønsted–Evans–Polanyi (BEP) relations[4–13] describing correlations between transition states and reaction energies, and the adsorbate scaling relations[14] describing correlations between the adsorption energies of adsorbed reaction intermediates containing hydrogen with respect to either C, N, or O. More generalized, the BEP relations can be viewed as resulting from a scaling relation between reaction intermediates and transition states. By combining transition state scaling relations and adsorbate scaling relations the number of individual parameters that needs to be determined in order to describe the energetic trends underlying the kinetics of a complex catalytic reaction can be significantly reduced, and often limited to only one or very few descriptors. Good descriptors are typically adsorption energies of some of the key reactive intermediates, or combinations of these.[15–23]

In the present paper we analyse the transition state energies for 249 dehydrogenation reactions of small hydrogen containing molecules over close-packed and stepped surfaces and nanoparticles of transition metals using Density Functional Theory (DFT). Linear energy correlations are observed for the transition state structures leading to transition state scaling relations for all the investigated reactions. Upon implementing a suitable choice of reference systems all the transition state scaling relations form a universality class[8,9] in which only one single descriptor can be used to determine the transition state for every reaction over all types of surfaces and nanoclusters.

2. Computational method

The calculations were carried out using the DACAPO plane wave Density Functional Theory code.[24] Exchange–correlation effects were described using the RPBE functional[25] with an energy cutoff of 340 eV or more. The ionic cores were described by Vanderbilt ultrasoft pseudopotentials.[26] A slab model with three (or in some cases four) close-packed atomic-layers was chosen to represent the transition metal surfaces describing the close-packed and stepped surfaces. At least one (in some cases two) top layer was fully relaxed and the rest of the metal layers were held at fixed positions. The size of a surface supercell was 2×2 for the close-packed surfaces, and supercell sizes of 1×2, 2×2, and 2×3 were used for the stepped surfaces depending on the size of the adsorbed molecules. The Brillouin zones were sampled using

[a] *Center for Atomic-scale Materials Design, Department of Physics, Building 307, Technical University of Denmark, DK-2800 Kgs. Lyngby, Denmark. E-mail: bligaard@fysik.dtu.dk; Fax: +45 4593 2399; Tel: +45 4525 3179*
[b] *Risø National Laboratory for Sustainable Energy, Materials Research Division, Building 228, Technical University of Denmark, DK-4000 Roskilde, Denmark*
[c] *Science Institute, VR-III, University of Iceland, IS-107 Reykjavik, Iceland*
[d] *SUNCAT Center for Interface Science and Catalysis, SLAC National Accelerator Laboratory, 2575 Sand Hill Road, Menlo Park, California 94025, USA*
[e] *Department of Chemical Engineering, Stanford University, Stanford, CA 94305, USA*
† Electronic supplementary information (ESI) available. See DOI: 10.1039/c1cp20547a

Monkhorst-Pack k-point meshes of 4 × 4 × 1 points or denser.[27] For the M12 nanoparticles, all the 12 atoms were fixed, while the adsorbates were allowed to relax. The M12 cluster was fixed in a planar structure identical to the geometry used in a recent study on CO oxidation.[18] The calculations on the M12 nanoparticles were carried out using only the gamma-point. The transition state energies were calculated using either a bond stretching method[28] or the nudged elastic band method which can be combined with the climbing image method to precisely determine the maximum barrier.[29] Several pathways were tested for each reaction step and in this paper we only report the first order saddle points corresponding to the lowest barrier. The maximum coverage on the active site was one half.

The convergence with respect to, number of layers, cutoff energy, and k-point sampling has been studied elsewhere[30] and we refer to this work for a more detailed evaluation of the accuracy of the data presented in this paper.

3. Results and discussion

A diagram explaining the reference energy levels used in the transition state scaling relations and in the Brønsted–Evans–Polanyi (BEP) relations for the dehydrogenation/hydrogenation processes is presented in Scheme 1. The transition state scaling relations are based on the transition state energy, E_{ts}, and the final state energy E_{diss}, with respect to the gas phase species[31] CH_4, NH_3, H_2O and H_2, see Scheme 1A. Whereas the BEP relation is based on the reaction energy, ΔE_{diss}, which is the energy difference between the initial and the final state, while the activation barrier, ΔE^{a}_{diss}, is the energy based on the difference in energy between the initial state and the transition state. This can be seen in Scheme 1B.

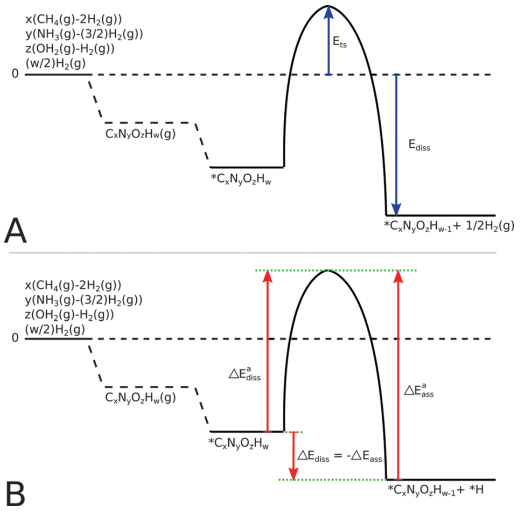

Scheme 1 The definition of energies used in this paper for the hydrogenation/dehydrogenation processes. All energies are with respect to the gas phase molecules of CH_4, NH_3, H_2O, and H_2. Top-view. (A) The transition state (TS) scaling relation are based upon the energies given by the two blue arrows denoted as E_{ts} for the transition state energy and E_{diss} for the final state energy. Bottom-view. (B) The Brønsted–Evans–Polanyi (BEP) relations use another reference energy. The BEP relations are based upon the activation barrier $\Delta E^{a}_{diss/ass}$ and the reaction energy $\Delta E_{diss/ass}$ as defined in the bottom panel.

Fig. 1 shows a universal transition state (TS) scaling relation for a series of dehydrogenation reactions over a wide range of transition metal surfaces, such as close-packed and stepped surfaces and nanoparticles. The fitted data for the transition state scaling relations for all the dehydrogenation reactions are presented in Table 1. Here the data have been arranged in categories of individual, classes, groups and overall. The individual fit is based on only one type of reaction on one surface type, the class is based on a specific reaction on all the types of surfaces, the grouped data are for all data containing either nitrogen, carbon or oxygen, and lastly the overall fit is based on all reactions on all types of surfaces.

The mean absolute error (MAE) of the fitted line in Fig. 1 is 0.28 eV. The correlation is certainly not perfect, and compared to so-called "chemical accuracy" which is typically defined as 1 kcal $mole^{-1}$ or approximately 40 meV, the error on a prediction based on using the linear relation shown in Fig. 1 will have a typical error one order of magnitude larger. The prediction error, however, has to be seen in the light of how well a typical GGA exchange–correlation functional can describe the reaction and transition state energies. The error in currently employed exchange–correlation functionals could easily be of the same size as the error from predictions based on the transition state scaling relations. The errors in the presented relation are certainly small enough to rapidly produce a first rough estimation of activation barriers for hydrogenation/dehydrogenation reactions. The universal TS scaling relation relates the energies of transition states with final states of dehydrogenation reactions.[13] Such correlation originates from the geometrical similarity of the structures of transition states and final states.[8]

Fig. 1 collects different types of dehydrogenation reactions on transition metal surfaces and clusters. The deviation of the

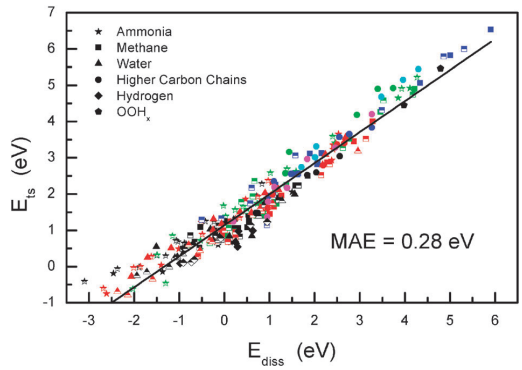

Fig. 1 Transition state energies plotted against dissociation energies with respect to energies of gas-phase CH_4, H_2O, NH_3, and H_2. The fully filled symbols refer to dissociation over close-packed surfaces, and the half-filled symbols refer to dissociation over stepped surfaces and OOH_x species have been dissociated on a M12 nanocluster. The colors represent the different hydrogen content in the molecules, where black is the first dehydrogenation step, red is the second step, green is the third step, and blue is the fourth dehydrogenation step.

Table 1 The fitted parameters of the transition state scaling relations with respect to energies of gas-phase CH_4, H_2O, NH_3, and H_2

Reaction	Surface	Slope	Constant/eV	MAE/eV
$H_2O(g) + 2^* \rightarrow OH^* + H^*$	Close packed	0.47 ± 0.10	0.99 ± 0.07	0.20
	Step	0.77 ± 0.02	0.95 ± 0.04	0.17
	All	0.58 ± 0.05	0.94 ± 0.04	0.16
$OH^* + ^* \rightarrow O^* + H^*$	Close packed	0.75 ± 0.03	1.32 ± 0.04	0.12
	Step	0.63 ± 0.03	0.92 ± 0.03	0.21
	All	0.78 ± 0.03	1.13 ± 0.05	0.20
Water group	All	0.74 ± 0.03	1.06 ± 0.04	0.20
$NH_3^* + ^* \rightarrow NH_2^* + H^*$	Close packed	0.57 ± 0.09	0.95 ± 0.11	0.24
	Step	0.69 ± 0.05	1.45 ± 0.07	0.14
	All	0.59 ± 0.06	1.19 ± 0.09	0.23
$NH_2^* + ^* \rightarrow NH^* + H^*$	Close packed	0.81 ± 0.03	1.26 ± 0.05	0.15
	Step	0.78 ± 0.04	1.41 ± 0.05	0.16
	All	0.79 ± 0.03	1.32 ± 0.04	0.16
$NH^* + ^* \rightarrow N^* + H^*$	Close packed	0.92 ± 0.04	1.09 ± 0.08	0.12
	Step	0.91 ± 0.04	1.41 ± 0.09	0.17
	All	0.87 ± 0.03	1.34 ± 0.07	0.19
Ammonia group	All	0.82 ± 0.02	1.33 ± 0.04	0.24
$CH_4(g) + 2^* \rightarrow CH_3^* + H^*$	Close packed	0.67 ± 0.11	1.04 ± 0.10	0.19
	Step	0.64 ± 0.09	1.01 ± 0.07	0.19
	All	0.67 ± 0.06	1.03 ± 0.05	0.18
$CH_3^* + ^* \rightarrow CH_2^* + H^*$	Close packed	0.92 ± 0.05	0.80 ± 0.08	0.11
	Step	0.86 ± 0.03	0.78 ± 0.05	0.09
	All	0.89 ± 0.03	0.79 ± 0.05	0.11
$CH_2^* + ^* \rightarrow CH^* + H^*$	Close packed	0.94 ± 0.02	1.02 ± 0.07	0.20
	Step	0.88 ± 0.06	1.22 ± 0.11	0.22
	All	0.90 ± 0.04	1.20 ± 0.10	0.27
$CH^* + ^* \rightarrow C^* + H^*$	Close packed	1.00 ± 0.03	0.72 ± 0.06	0.16
	Step	0.88 ± 0.07	1.29 ± 0.17	0.26
	All	0.92 ± 0.04	1.02 ± 0.08	0.23
$C_2H_6(g) + 2^* \rightarrow C_2H_5^* + H^*$	Step	0.85 ± 0.03	0.87 ± 0.05	0.14
$C_2H_5^* + ^* \rightarrow C_2H_4^* + H^*$	Step	0.99 ± 0.10	0.77 ± 0.20	0.11
$C_2H_4^* + ^* \rightarrow C_2H_3^* + H^*$	Step	0.92 ± 0.11	1.57 ± 0.31	0.18
$C_3H_8(g) + 2^* \rightarrow C_3H_7^* + H^*$	Step	0.76 ± 0.06	1.49 ± 0.13	0.08
$C_3H_6^* + ^* \rightarrow C_3H_5^* + H^*$	Step	1.04 ± 0.04	1.03 ± 0.13	0.07
Hydrocarbon group	All	0.95 ± 0.02	0.97 ± 0.04	0.25
$H_2(g) + 2^* \rightarrow 2H^*$	Close packed	0.67 ± 0.06	0.69 ± 0.04	0.08
	Step	0.54 ± 0.14	0.60 ± 0.08	0.11
	All	0.61 ± 0.07	0.65 ± 0.04	0.10
All	All	0.86 ± 0.01	1.14 ± 0.02	0.28

points comes predominantly from the difference of the structures of the reactions. As expected from Table 1, the MAE becomes smaller when we look into a certain reaction or a series of similar reactions, since the structures are more similar to each other. The MAE is typically smaller than 0.15 eV for an individual reaction over a given geometry of an active surface site, as evidenced in Table 1. When looking at several reactions simultaneously or several surface geometries, the uncertainty of a prediction made from their common linear regression fit will generally increase, but in all cases stays below 0.3 eV. It is therefore useful to see Table 1 as a hierarchy of accuracy that allows treating a particular reaction more accurately if it resembles one of the specifically presented reactions, whereas the overall universal TS scaling can be used for a general hydrogen bond breaking reaction which has not been specifically treated in this study.

Fig. 2 shows the BEP relations of the whole set of dehydrogenation reactions. The MAE of 0.27 eV is close to that of the above-discussed universal TS scaling relation. The practical performance of these two relations with respect to estimation of activation energies should be very similar, based on the fact that their MAEs are very close.

Although the universal BEP relation in Fig. 2 may at a first glance look less presentable than the universal TS scaling relation, we would like to emphasize several merits of it. The first merit of BEP relations is of course the clear trend reflected by the relations. Since activation energies and reaction

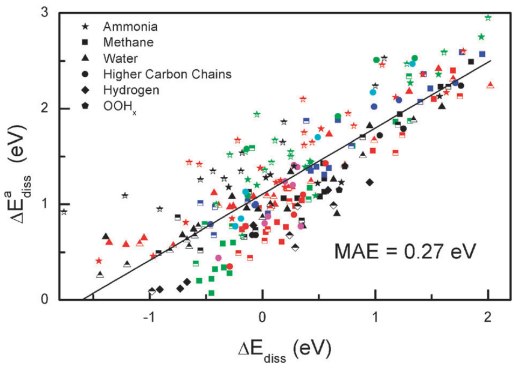

Fig. 2 Activation energies, ΔE^a_{diss}, plotted against reaction energies, ΔE_{diss}, of the dehydrogenation reactions. The fully filled symbols refer to data on close-packed surfaces, and the half filled symbols mean the data on step surfaces. The colors represent the different hydrogen content in the molecules, where black is the first dehydrogenation step, red is the second step, green is the third step and blue is the fourth dehydrogenation step.

energies are typical experimentally measured properties for the analysis of catalytic reactions, rather than the transition state total energies and final state total energies with respect to a gas phase reference it may also be easier to correlate theory and experiments using the BEP relations. The TS scaling relations are (in the present study) based on the structural similarities of the transition states and the final states of a reaction. Such direct similarity between states generally only holds for a limited range of surface reactivity. On the late transition metals there will be a tendency towards having late transition states, and over the early transition metals the transition states will also be earlier. The TS scaling relations (in the form presented above) will thus have a relatively larger MAE when applied to reactions over early transition metals. Therefore it makes more sense to use the TS scaling relations in the presented form for reactions over surfaces of a rather similar reactivity. The BEP relations correlate the activation barrier with contributions from both initial and final states. Therefore the BEP relations tend to be valid for the catalytic reactions in a larger window of variation of the surface reactivity. The shift in similarity of the transition state structures with initial and final states thus gives rise to a slightly v-shaped distribution of errors in Fig. 1, whereas the noise distribution is more homogeneous in Fig. 2.

The fitted parameters of separate BEP relations of the dehydrogenation reactions are listed in Table 2. It is found that the MAE becomes gradually smaller from the whole set of data to similar groups of reactions and one reaction. The reason is that the scattering caused by the difference of geometric structures has been eliminated to a large degree when only focusing on similar reactions. Hence, using parameters for a certain reaction will yield high accuracy for that or very similar reactions. The parameters for grouped reactions and the universal relation are also useful for fast calculations for preliminary and rough trends. This becomes useful when not all parameters are available or in cases where the demand for accuracy is less strict.

According to the scaling relations, the binding energies of a series of hydrogen-containing molecules are linearly correlated with the binding energies of their central atoms.[14] Fig. 3 shows that the linear relations are also valid for the correlation of the transition state energies for hydrogenation/dehydrogenation reactions and binding energies of the central atoms. Furthermore, Fig. 4 shows that the adsorption energies of hydrogen scale approximately with the adsorption energies of C, N, and O. The scatter increases as one moves from C to O. The linear TS scaling relations and the BEP relations are therefore both manifestations of the scaling relation between reaction intermediates and transition states with the adsorption energies of the central

Table 2 The fitted parameters of BEP relations

Reaction	Surface	Slope	Constant/eV	MAE/eV
$H_2O(g) + 2^* \rightarrow OH^* + H^*$	Close packed	0.44 ± 0.10	1.04 ± 0.07	0.19
	Step	0.57 ± 0.03	1.00 ± 0.02	0.06
	All	0.51 ± 0.05	1.01 ± 0.04	0.14
$OH^* + ^* \rightarrow O^* + H^*$	Close packed	0.62 ± 0.06	1.23 ± 0.05	0.16
	Step	0.59 ± 0.04	1.08 ± 0.03	0.09
	All	0.59 ± 0.04	1.15 ± 0.03	0.17
Water group	All	0.57 ± 0.03	1.09 ± 0.03	0.15
$NH_3^* + ^* \rightarrow NH_2^* + H^*$	Close packed	0.46 ± 0.13	1.21 ± 0.09	0.14
	Step	0.57 ± 0.06	1.65 ± 0.05	0.13
	All	0.42 ± 0.08	1.47 ± 0.06	0.20
$NH_2^* + ^* \rightarrow NH^* + H^*$	Close packed	0.68 ± 0.05	1.23 ± 0.05	0.14
	Step	0.57 ± 0.08	1.66 ± 0.08	0.19
	All	0.68 ± 0.06	1.41 ± 0.06	0.21
$NH^* + ^* \rightarrow N^* + H^*$	Close packed	0.79 ± 0.09	1.13 ± 0.09	0.11
	Step	0.74 ± 0.11	1.45 ± 0.09	0.19
	All	0.72 ± 0.08	1.35 ± 0.07	0.19
Ammonia group	All	0.61 ± 0.04	1.43 ± 0.04	0.23
$CH_4(g) + 2^* \rightarrow CH_3^* + H^*$	Close packed	0.92 ± 0.07	0.77 ± 0.07	0.07
	Step	0.66 ± 0.10	1.00 ± 0.08	0.18
	All	0.72 ± 0.06	0.96 ± 0.06	0.16
$CH_3^* + ^* \rightarrow CH_2^* + H^*$	Close packed	0.96 ± 0.07	0.67 ± 0.05	0.07
	Step	0.80 ± 0.07	0.71 ± 0.06	0.10
	All	0.87 ± 0.05	0.70 ± 0.04	0.10
$CH_2^* + ^* \rightarrow CH^* + H^*$	Close packed	1.02 ± 0.07	0.73 ± 0.04	0.09
	Step	0.75 ± 0.16	1.09 ± 0.11	0.25
	All	0.91 ± 0.11	0.88 ± 0.07	0.22
$CH^* + ^* \rightarrow C^* + H^*$	Close packed	0.87 ± 0.07	0.97 ± 0.07	0.09
	Step	0.71 ± 0.11	1.19 ± 0.08	0.18
	All	0.75 ± 0.06	1.12 ± 0.06	0.15
$C_2H_6(g) + 2^* \rightarrow C_2H_5^* + H^*$	Step	0.86 ± 0.03	0.75 ± 0.03	0.03
$C_2H_5^* + ^* \rightarrow C_2H_4^* + H^*$	Step	1.05 ± 0.22	0.75 ± 0.08	0.16
$C_2H_4^* + ^* \rightarrow C_2H_3^* + H^*$	Step	0.86 ± 0.18	1.45 ± 0.15	0.18
$C_3H_8(g) + 2^* \rightarrow C_3H_7^* + H^*$	Step	0.76 ± 0.06	1.11 ± 0.06	0.09
$C_3H_6^* + ^* \rightarrow C_3H_5^* + H^*$	Step	1.04 ± 0.07	1.13 ± 0.05	0.08
Hydrocarbon group	All	0.84 ± 0.04	0.94 ± 0.03	0.21
$H_2(g) + 2^* \rightarrow 2H^*$	Close packed	0.67 ± 0.06	0.69 ± 0.04	0.08
	Step	0.54 ± 0.14	0.60 ± 0.08	0.11
	All	0.61 ± 0.07	0.65 ± 0.04	0.10
Universal	All	0.69 ± 0.03	1.11 ± 0.02	0.27

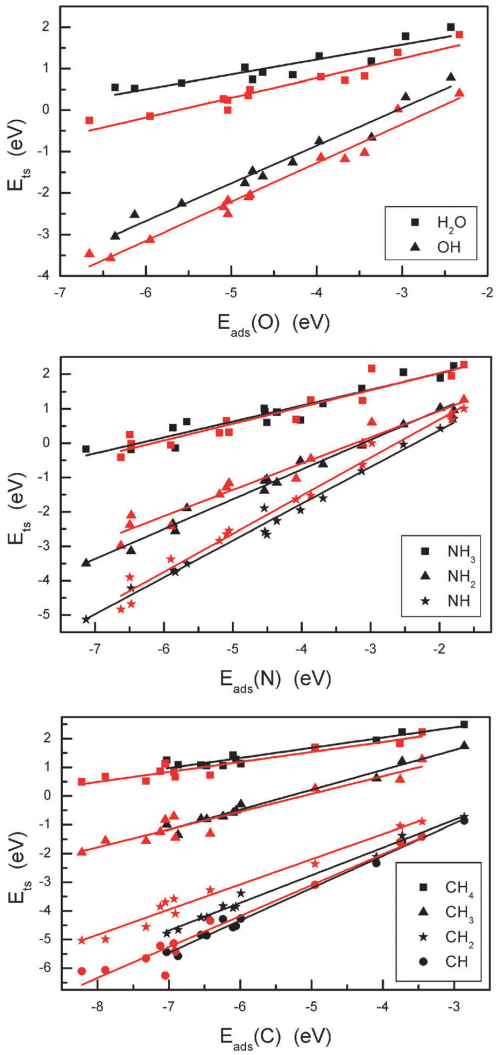

Fig. 3 The transition state energies of dehydrogenation reactions plotted against the adsorption energies of (a) O, (b) N and (c) C with respect to their gas-phase energies. The black and red colors indicate the results on close-packed and step surfaces respectively.

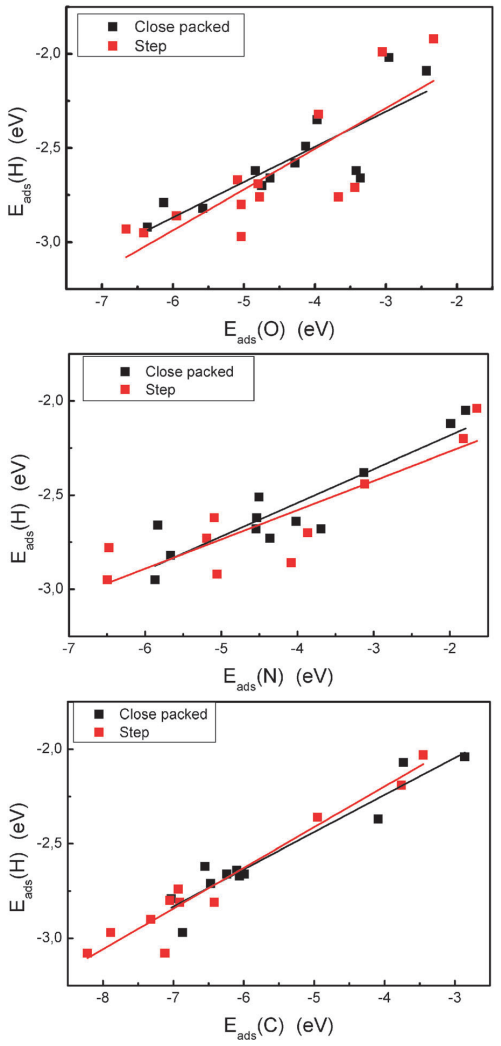

Fig. 4 The adsorption energies of H plotted against the adsorption energies of (a) O, (b) N and (c) C with respect to their gas-phase energies.

atoms (those atoms in contact with the surface). Because the transition state for dehydrogenation reactions is very similar over close-packed and stepped surfaces or a nanoparticle, there is no major geometrical effect for the single TS scaling relation and the BEP relation for all treated hydrogenation/dehydrogenation steps, and all points fall on one line in Fig. 2. For a single reaction, however, there can be a significant electronic effect going from a close-packed surface to a more under-coordinated surface, such as a step or a nanocluster. This is a particular feature of hydrogenation/dehydrogenation reactions and somewhat different from many other bond-breaking reactions on transition metal surfaces, where steps are typically many orders of magnitude more reactive than the close-packed surfaces.[10,32]

If we now more generally consider a transition state scaling relation to represent a general correlation between the energy of the transition state and some combination of relevant adsorption energies, then the BEP relation is one such particular choice of linear combination of the relevant adsorption energies. One may then well ask the question: "what linear combination of relevant energies of adsorption intermediates is the best representation of a given reaction?" This question we shall attempt to address in a subsequent piece of work based on a statistical viewpoint.[33]

Conclusions

We have presented a universal transition state scaling relation for dehydrogenation reactions over close-packed and stepped surfaces as well as nanoparticles of transition metals. One

simple relation is demonstrated to cover a very broad class of hydrogenation/dehydrogenation surface chemistry over transition metals, since all of the investigated reactions, metals, and surface geometries can be reasonably well approximated by one universal linear transition state scaling relation. This holds promise that in the future the search for new hydrogenation catalysts may be facilitated by the fact that a first rough initial screening can be carried out based on this general linear energy relation without the need for performing full DFT calculations. Together with the adsorbate scaling relations for various reaction intermediates, the universal BEP relation for (de)hydrogenation reactions can become a tool with predictive power and give a fast and semi-accurate first-hand knowledge for a number of catalytic reactions which can then subsequently be analyzed in greater detail.

Acknowledgements

The Center for Atomic-scale Materials Design is funded by The Lundbeck Foundation. The SUNCAT Center for Interface Science and Catalysis at SLAC is funded by the U.S. Department of Energy. We thank the Danish Center for Scientific Computing (DCSC) and the Catalysis for Sustainable Energy (CASE) initiative funded through the Danish Ministry of Science, Technology, and Innovation for financial support.

Notes and references

1 J. K. Nørskov, T. Bligaard, J. Rossmeisl and C. H. Christensen, *Nat. Chem.*, 2009, **1**, 37.
2 J. K. Nørskov, F. Abild-Pedersen, F. Studt and T. Bligaard, *Proc. Natl. Acad. Sci. U. S. A.*, 2011, **108**, 937.
3 M. Neurock, *Ind. Eng. Chem. Res.*, 2010, **49**, 10183.
4 M. G. Evans and M. Polanyi, *Trans. Faraday Soc.*, 1938, **34**, 11.
5 V. Pallassana and M. Neurock, *J. Catal.*, 2000, **191**, 301.
6 Z.-P. Liu and P. Hu, *J. Chem. Phys.*, 2001, **114**, 8244.
7 A. Logadottir, T. H. Rod, J. K. Nørskov, B. Hammer and C. J. H. Jacobsen, *J. Catal.*, 2001, **197**, 229.
8 J. K. Nørskov, T. Bligaard, A. Logadottir, S. R. Bahn, L. B. Hansen, M. V. Bollinger, H. S. Bengaard, B. Hammer, Z. Sljivancanin, M. Mavrikakis, Y. Xu, S. Dahl and C. J. H. Jacobson, *J. Catal.*, 2002, **209**, 275.
9 A. Michaelides, Z.-P. Liu, C. J. Zhang, A. Alavi, D. A. King and P. Hu, *J. Am. Chem. Soc.*, 2003, **125**, 3704.
10 S. Wang, B. Temel, J. Shen, G. Jones, L. C. Grabow, F. Studt, T. Bligaard, F. Abild-Pedersen, C. H. Christensen and J. K. Nørskov, *Catal. Lett.*, 2011, **141**, 370.
11 P. Crawford, B. McAllister and P. Hu, *J. Phys. Chem. C*, 2009, **113**, 5222.
12 J. Cheng, P. Hu, P. Ellis, S. French, G. Kelly and C. M. Lok, *J. Phys. Chem. C*, 2008, **112**, 1308.
13 D. Loffreda, F. Delbecq, F. Vigné and P. Sautet, *Angew. Chem., Int. Ed.*, 2009, **48**, 4978.
14 F. Abild-Pedersen, J. Greeley, F. Studt, J. Rossmeisl, T. R. Munter, P. G. Moses, E. Skúlason, T. Bligaard and J. K. Nørskov, *Phys. Rev. Lett.*, 2007, **99**, 016105.
15 F. Studt, F. Abild-Pedersen, T. Bligaard, R. Z. Sørensen, C. H. Christensen and J. K. Nørskov, *Science*, 2008, **320**, 1320.
16 M. P. Andersson, T. Bligaard, A. Kustov, K. E. Larsen, J. Greeley, T. Johannessen, C. H. Christensen and J. K. Nørskov, *J. Catal.*, 2006, **239**, 501.
17 G. Jones, J. G. Jakobsen, S. S. Shim, J. Kleis, M. P. Andersson, J. Rossmeisl, F. Abild-Pedersen, T. Bligaard, S. Helveg, B. Hinnemann, J. R. Rostrup-Nielsen, I. Chorkendorff, J. Sehested and J. K. Nørskov, *J. Catal.*, 2008, **259**, 147.
18 H. Falsig, B. Hvolbæk, I. S. Kristensen, T. Jiang, T. Bligaard, C. H. Christensen and J. K. Nørskov, *Angew. Chem., Int. Ed.*, 2008, **47**, 4835.
19 A. Hellman, E. J. Baerends, M. Biczysko, T. Bligaard, C. H. Christensen, D. C. Clary, S. Dahl, R. van Harrevelt, K. Honkala, H. Jónsson, G. J. Kroes, M. Luppi, U. Manthe, J. K. Nørskov, R. A. Olsen, J. Rossmeisl, E. Skúlason, C. S. Tautermann, A. J. C. Varandas and J. K. Vincent, *J. Phys. Chem. B*, 2006, **110**, 17719.
20 P. Ferrin, D. Simonetti, S. Kandoi, E. Kunkes, J. A. Dumesic, J. K. Nørskov and M. Mavrikakis, *J. Am. Chem. Soc.*, 2009, **131**, 5809.
21 G. A. Somorjai and Y. Li, *Top. Catal.*, 2010, **53**, 311.
22 N. Schumacher, A. Boisen, S. Dahl, A. A. Gokhale, S. Kandoi, L. C. Grabow, J. A. Dumesic, M. Mavrikakis and I. Chorkendorff, *J. Catal.*, 2005, **229**, 265.
23 J. Cheng and P. Hu, *J. Am. Chem. Soc.*, 2008, **130**, 10868.
24 The Dacapo plane wave/pseudopotential DFT code is available as open source software at http://wiki.fysik.dtu.dk/dacapo.
25 B. Hammer, L. B. Hansen and J. K. Nørskov, *Phys. Rev. B: Condens. Matter Mater. Phys.*, 1999, **59**, 7413.
26 D. Vanderbilt, *Phys. Rev. B: Condens. Matter*, 1990, **41**, 7892.
27 H. J. Monkhorst and S. D. Pack, *Phys. Rev. B: Solid State*, 1976, **13**, 5188.
28 M. P. Andersson, F. Abild-Pedersen, I. N. Remediakis, T. Bligaard, G. Jones, J. Engbæk, O. Lytken, S. Horch, J. H. Nielsen, J. Sehested, J. R. Rostrup-Nielson, J. K. Nørskov and I. Chorkendorff, *J. Catal.*, 2008, **255**, 6.
29 G. Henkelman and H. Jónsson, *J. Chem. Phys.*, 2000, **113**, 9978.
30 F. Abild-Pedersen and M. P. Andersson, *Surf. Sci.*, 2007, **601**, 1747.
31 R. Alcalá, M. Mavrikakis and J. A. Dumesic, *J. Catal.*, 2003, **218**, 178.
32 J. K. Nørskov, T. Bligaard, B. Hvolbæk, F. Abild-Pedersen, I. Chorkendorff and C. H. Christensen, *Chem. Soc. Rev.*, 2008, **37**, 2163.
33 T. Bligaard, *et al.*, in preparation.

Paper IV

Volcano Relations for Oxidation of Hydrogen Halides over Rutile Oxide Surfaces

Anja Toftelund, Isabela C. Man, Heine A. Hansen, Frank Abild-Pedersen, Thomas Bligaard, Jan Rossmeisl, and Felix Studt

Submitted

DOI: 10.1002/cctc.200((will be filled in by the editorial staff))

Volcano Relations for Oxidation of Hydrogen Halides over Rutile Oxide Surfaces

Anja Toftelund,[a] Isabela C. Man,[a] Heine A. Hansen,[b] Frank Abild-Pedersen,[c] Thomas Bligaard,[b,c] Jan Rossmeisl,[a] and Felix Studt[c]*

We investigate the heterogeneous catalytic oxidation of HX (X = Cl, Br, and I) on the RuO_2 (110) surface with density functional theory (DFT). We solve a micro-kinetic model of HX oxidation and compare oxidation activity at different coverage. We further establish linear energy relations for the reaction intermediates over a range of different rutile oxide surfaces. Based on the obtained scaling relations two descriptors are identified that describe the reactions uniquely. By combining scaling with the micro-kinetic model activity volcanoes for the three different oxidation reactions are derived. It is found that the commonly used RuO_2 catalyst for HCl oxidation is closest to optimal for all three oxidation processes.

Introduction

Halides are versatile compounds in the chemical industry with chlorine being the most important one. Being produced at scales of 65 Mtonnes per year, chlorine is used as disinfectants and for water treatment as well as for the production of e.g. polyvinylchloride, isocyanates, and chloromethanes.[1,2,3] Bromine and iodine are produced at much smaller scales; bromine is found in flame retardants, dyes, and insect repellents[4] while iodine's main applications are as a co-catalyst for the production of acetic acid and as food supplement for live-stock in the form of ethylenediammonium diiodide.[5] Bromine has recently attracted attention as it was suggested to be used in small to medium-scale gas to liquid processes[6,7] where Br_2 can be used to brominate methane or other alkanes into alkyl bromide in formation of longer alkanes. In this process Br_2 needs to be completly recovered from HBr.

Chlorine is mainly produced via electrochemical reduction of chloride salt solution using the so-called membrane, mercury, or diaphragm processes.[8] Alternatively it can also be produced (and originally was) via the heterogeneously catalysed oxidation of HCl by oxygen (the Deacon process, see equation 1).[9,10] This process has a much lower energy consumption compared to the electrochemical processes,[11] but needs HCl as a starting point. This, however, could also make the Deacon process interesting for recycling reactions. Bromine as well as iodine are usually produced via oxidation with chlorine gas.[8] Oxidation of HBr and HI with air via a process similar to the Deacon process, however, should in principle be possible as well (see equation 2 and 3). Recycling of bromine via oxidation could potentially become one of the key steps in the economically viable catalytic gas to liquid process described above.

$$4\ HCl(g) + O_2(g) \rightarrow 2\ Cl_2(g) + 2\ H_2O(g)\ (\Delta H^{298} = -114\ kJ\ mol^{-1}) \quad (1)$$

$$4\ HBr(g) + O_2(g) \rightarrow 2\ Br_2(g) + 2\ H_2O(g)\ (\Delta H^{298} = -276\ kJ\ mol^{-1}) \quad (2)$$

$$4\ HI(g) + O_2(g) \rightarrow 2\ I_2(g) + 2\ H_2O(g)\ (\Delta H^{298} = -465\ kJ\ mol^{-1}) \quad (3)$$

Industrial production of chlorine via the Deacon process utilizes a RuO_2 catalyst supported on TiO_2.[10] There are a few theoretical studies for this process,[12,13,14,15,16] a theoretical analysis regarding a similar process for HBr and HI oxidation, however, is still missing.

Herein we investigate the heterogeneously catalysed oxidation of all three halides (HCl, HBr, and HI) over rutile oxide surfaces. This study presents an extension of our earlier study on HCl oxidation over three rutile oxide surfaces.[12] We are expanding the study to the other two halides, HBr and HI, under the assumption that the oxidation follows the same route as found for HCl. Furthermore, we include more rutile oxide surfaces and are solving the full micro-kinetics without any assumptions on rate determining steps. We will also refine previously obtained scaling relations of adsorbates[12] in order to get an improved description of reaction parameters.

We will start by investigating the three different processes over the RuO_2(110) surface which represents the active site of the industrially used catalyst in HCl oxidation.[14] By applying scaling relations for the different adsorbates and transition states we find that two descriptors define the activity of the surfaces employed in this study. With the help of these descriptors a

[a] *Anja Toftlelund, Dr. Isabela C. Man, Prof. Jan Rossmeisl*
Center for Atomic-scale Materials Design, Department of Physics
Technical University of Denmark
DK-2800 Kgs. Lyngby, Denmark
[b] *Dr. Heine A. Hansen, Dr. Thomas Bligaard,*
Department of Chemical Engineering
Stanford University, Stanford, CA 94305, U.S.A.
[c] *Dr. Frank Abild-Pedersen, Dr. Thomas Bligaard, Dr. Felix Studt,*
SUNCAT Center for Interface Science and Catalysis
SLAC National Accelerator Laboratory
2575 Sand Hill Road, Menlo Park, CA 94025, U.S.A.
E-mail: studt@slac.stanford.edu

Supporting information for this article is available on the WWW under http://dx.doi.org/10.1002/cctc.200xxxxxx.

micro-kinetic model is solved so that two dimensional volcano-shaped activity plots are obtained for the three different processes.

Results and Discussion

The rutile oxide (110) surface

The chemistry on the rutile oxide (110) surfaces is primarily taking place on the coordinative unsaturated (cus) sites. These cus sites are situated between rows of oxygen atoms that are strongly bound at the bridge sites between two metal atoms. Experimental and theoretical work on the RuO_2 surface shows that under reaction conditions of the Deacon process most of these bridging oxygen atoms will be replaced by chlorine.[12,14,15] Bridging oxygen atoms of TiO_2 and IrO_2 surfaces on the other hand are not predicted to be replaced.[12] Similar calculations predict that RuO_2 and PtO_2 exposed to HBr and HI will have the bridging oxygen atoms replaced by Br and I, respectively (see supplementary material, figures S1 and S2).

Replacing bridged oxygen by halides has been shown to have a rather small effect to adsorption energies on cus sites in the case of chlorine[12] and we assume that the same is true for bromine and iodine. We therefore limit this first analysis to surfaces with oxygen in the bridge site only. Since bridge oxygen is hard to replace in most surfaces it can be seen as a spectator and the reaction is occurring along the cus sites only. We considered both, the high and low coverage regime on the cus sites; the low coverage model has 50% of the sites occupied whereas the high coverage model has 100% of the cus sites occupied by adsorbates.

Reaction mechanism

Figure 1 shows the free energy diagram of the heterogeneously catalysed oxidation of HCl, HBr, and HI on the RuO_2(110) surface at 573K for both, the high and low coverage regime. The same analysis of the reaction pathway has been used for the high coverage regime of HCl oxidation in our earlier study.[12]

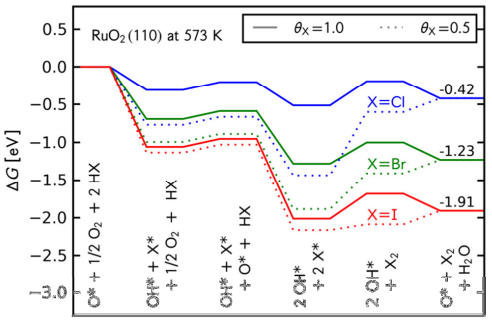

Figure 1. Gibbs free energy diagram for the oxidation of HCl, HBr, and HI on RuO_2(110) at 573K as obtained from DFT calculations. Solid and dotted lines represent high and low coverages, respectively. X denotes a halide (Cl, Br, or I) and * denotes an adsorbed atom or molecule.

As can be seen in figure 1, oxidation of HX becomes more exothermic from Cl to Br to I with the reaction free energies being -0.42, -1.23, and -1.91 eV. The reaction cycle starts with the dissociative adsorption of HX (X = Cl, Br, I) on the cus site of an oxygen pre-covered surface. Adsorption proceeds via dissociation of H-X where the hydrogen atom binds on top the oxygen and the chlorine binds directly to the free cus site. This step is thermodynamically downhill for all three halides, being most downhill for iodine. The next step is the dissociative adsorption of O_2. After coadsorption of a second HX the two OH groups recombine to give H_2O and adsorbed O and the two X recombine to X_2. For HCl, this recombination of two Cl atoms represents the most difficult step of the catalytic cycle. Moreover, it can be seen that this step is only feasible in the high coverage regime as recombination becomes prohibitively endothermic at low chlorine coverages, in agreement with earlier theoretical studies.[12,13]

When going from chlorine to bromine to iodine the overall process becomes more exothermic. This is reflected in the thermodynamics where especially the dissociative adsorption of HX becomes more exothermic being -0.31 eV (-0.77 eV) for HCl, -0.69 eV (-1.00 eV) for HBr, and -1.06 eV (-1.14 eV) for HI (for high (low) coverage of X*). Desorption of Br_2 is the most energy demanding step in HBr oxidation being uphill in free energy by 0.28 eV (0.48 eV) at 573K. As for HCl oxidation, this step is more facile at high coverages, though the difference to the low coverage regime is not as large. Interestingly, recombination of two iodine atoms to form I_2 is similarly uphill as the recombination of two Cl and two Br at high coverages. Recombination of two iodine atoms at low coverages on the other hand is only slightly endothermic by 0.08 eV. This is due to interactions between iodine atoms that increase overall iodine binding at high coverages. HI oxidation will thus be more active at low coverages whereas HCl and HBr oxidation will occur in the high coverage regime.

Microkinetic model

We will now employ a microkinetic model for the three oxidation processes on the RuO_2(110) surface. The model consists of the five elementary reaction steps (1-5):

1) $O_2+2^* \rightarrow O_2^{**}$
2) $O_2^{**} \rightarrow 2O^*$
3) $O^*+^*+HX \rightarrow OH^*+X^*$
4) $2X^* \rightarrow X_2+2^*$
5) $2OH \rightarrow O^*+^*+H_2O$

where * denotes an empty site on the surface. Note that the dissociative adsorption of O_2 has been split up into two steps; the molecular adsorption of O_2 and its dissociation into two O*. The same model is described in earlier work for the HCl oxidation with reaction step 2 and 4 (O_2 dissociation and chlorine recombination) as the rate determining steps.[12] It has been found that dissociation of diatomic molecules over cus-cus on rutile oxide surfaces almost exclusively have the barrier given by the change in reaction energy.[27] If extra transition barriers exist they are reasonably small and therefore neglected in our model. We extend our analysis here to other halides without making any assumptions on rate determining steps. Our results are hence based on the exact steady-state solution of the micro-kinetic model. In the model the following systems of equations are

solved with respect to the four different surface species present at HX oxidation, θ_{O_2}, θ_O, θ_{OH}, and θ_X:

$$r_1 = r_2 \quad (1)$$

$$r_2 = 4r_3 \quad (2)$$

$$2r_3 = r_4 \quad (3)$$

$$r_4 = r_5 \quad (4)$$

$$\theta_{O_2} + \theta_O + \theta_X + \theta_{OH} + \theta_* = 1 \quad (5)$$

where the reaction rates r_1 - r_5 are the reaction rates for the five elementary reaction steps:

$$r_1 = k_1 p_{O_2} \theta_*^2 - 1/2 k_{-1} \theta_{O_2} \quad (6)$$

$$r_2 = 1/2 k_2 \theta_{O_2} - k_{-2} \theta_O^2 \quad (7)$$

$$r_3 = k_3 p_{HX} \theta_O \theta_* - k_{-3} \theta_{OH} \theta_X \quad (8)$$

$$r_4 = k_4 \theta_X^2 - k_{-4} p_{X_2} \theta_*^2 \quad (9)$$

$$r_5 = k_5 \theta_{OH}^2 - k_{-5} p_{H_2O} \theta_O \theta_* \quad (10)$$

The equilibrium constants are given by:

$$K_i = e^{\frac{-\Delta G_i}{kT}} \quad (11)$$

and the forward and backward rates are:

$$k_i = \frac{kT}{h} e^{\frac{-\Delta G_i^+}{kT}} \quad (12)$$

$$k_{-i} = \frac{k_i}{K_i} \quad (13)$$

(See the supplementary material for the full description of the model).

Solving the model described above yields the turnover frequencies (TOFs) for the three oxidation processes. Figure 2 shows the TOFs as a function of temperature for both, for the high and low coverage regime.

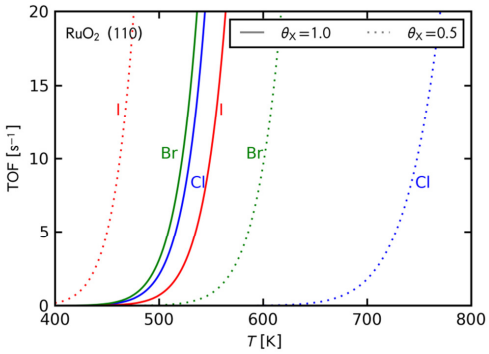

Figure 2. Turnover frequencies (TOFs) as a function of temperature for HCl, HBr, and HI oxidation over RuO_2(110) as obtained from the solution of the microkinetic model. Results for high (solid lines) and low (dotted lines) coverages are shown.

Inspection of Figure 2 reveals what one would expect from the energetics shown in Figure 1. As recombination of two X to form X_2 is very similar for all three halides at high coverages; their onset activities for X_2 production are very similar. All three halides start X_2 production around 500K. A similar result was found for HCl oxidation on the basis of RuO_2(110) data that was derived from scaling relations[12] as well as experimental work.[13] For chlorine and bromine, the activity of the low coverage regime is much lower whereas a higher activity is predicted for iodine at low coverages; I_2 production at low coverages is starting already around 400 K.

We performed a sensitivity analysis of the rates shown in Figure 2 in order to get an estimate of the accuracy of our model (see supplementary material). We applied an "error" of 0.2 eV to the adsorption energy of chlorine and found that the onset temperature calculated with our model shifts by as much as 150K. The rates given in Figure 2 should therefore be taken with care and we see this more as a trend study rather than being able to predict the magnitude of total rates.

Extension to other rutile surfaces

In order to extend this model to other rutile surfaces, we applied scaling relations between different adsorbates and surfaces. These scaling relations were first described for transition metal surfaces[17,18] but have been extended to oxides[19,20] and have been used recently to scale the Deacon process for different surfaces.[12] Whereas only one parameter, the dissociative chemisorption energy of oxygen, was used in the earlier model, we will extend our analysis in the following to two parameters. The reason for that extension is explained below.

In order to describe the overall processes, the adsorption energies of the six different surface species, O_2**, O*, OH*, Cl*, Br*, and I* are considered. In earlier studies O* was used to describe the adsorption of OH*.[20,12,21] Later models, however, differentiate between O* and OH* adsorption energies since their scaling behaviour is not always perfect, so that a better description is often achieved when OH* as a second variable is invoked.[22,23] This can also be seen in Figure 3 where the relation between OH* and O* is shown. While the overall trend between OH* and O* is clearly observed, a mean absolute error (MAE) of 0.74 eV suggests that one has to take care when using this scaling relation.

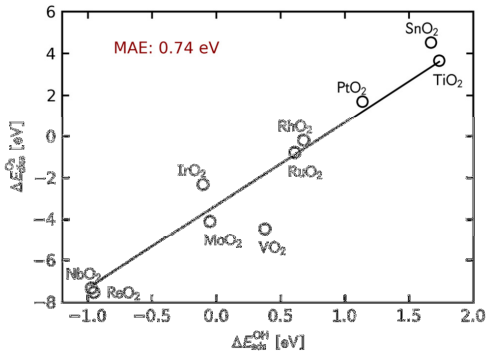

Figure 3. Dissociative chemisorption energy of O_2 ($\Delta E_{diss}^{O_2}$) plotted as a function of the adsorption energy of OH (ΔE_{ads}^{OH}) on a variety of rutile(110) surfaces as obtained from DFT calculations. Gas-phase O_2 and H_2O are used as a reference, respectively. Gas-phase O_2 has been corrected as described in reference [24].

Interestingly, a few outliers, e.g. IrO_2 and VO_2, cause the large MAE. We tested the values obtained for IrO_2 and RuO_2 with the all electron DFT code GPAW[25] using the RPBE functional,[26] and obtained similar results (see supplementary material). This may indicate that the deviations originate from differences in the underlying physics of the systems that are not described by the scaling relations. We have therefore chosen to invoke OH* as a second descriptor in our model. All other adsorption energies can be described well by either one of them, as we will show in the following.

Figure 4a and 4b show the scaling of intermediates as a function of OH* for the low and high coverage regimes, respectively. As can be seen in figure 4a the halides scale with the OH binding energy. A slope of 1 has been fitted through the binding energies of the halides giving reasonable correlations. The error does, however, increase when going from chlorine to bromine and is largest for iodine. Molecular adsorption of O_2 has been found to scale reasonably with the adsorption energy of OH as well. A slope of 1.42 is obtained when fitting through the O_2 adsorption values which is possibly due to an extensive activation of the O=O double bond on the rutiles.

Figure 4b shows the scaling of Cl, Br and I that are adsorbed next to Cl, Br, and I, respectively, corresponding to high coverage of the halides. The adsorption energies are plotted as a function of the OH binding energy of an OH group that is also adsorbed next to a Cl, Br or I, respectively. As can be seen from figure 4b, the slopes are less than those obtained for the low coverage and are decreasing from Cl to Br and I, with I having a slope of 0. This is due to an extensive interaction between two halides that are adsorbed next to each other. This interaction increases from Cl to Br and I so that the effect is largest for iodine. One would expect a slope of 1 as observed for the low coverage regime and the interaction between halides can be seen as decreasing this scaling due to a decrease in interaction between the halides and the oxide surfaces.

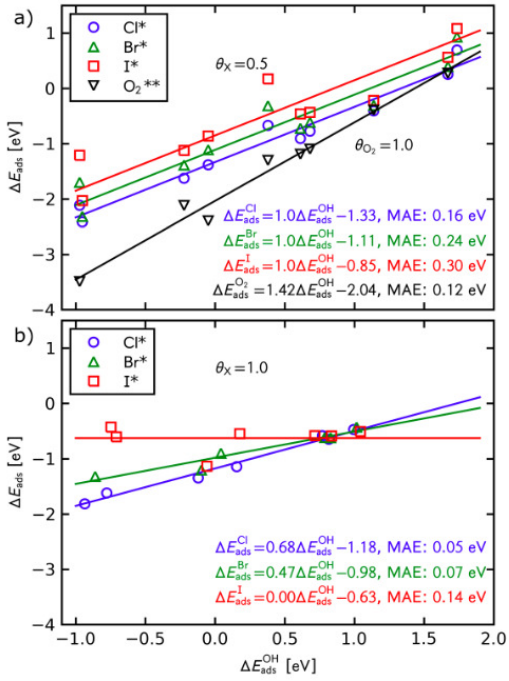

Figure 4a. Adsorption energies of Cl, Br, and I at a coverage of 0.5 and adsorption energies of O_2 at a coverage of 1.0 plotted as a function of the chemisorption energy of OH at a coverage of 0.5 on a variety of rutile(110) surfaces as obtained from DFT calculations. b. Adsorption energies of Cl, Br, and I, at a coverage of 1.0 plotted as a function of the chemisorption energies of OH at a coverage of 1.0. OH coverage of 1.0 is achieved by adsorbing an OH in a 2x1 unit cell next to a Cl, Br, and I for the Cl, Br, and I scaling, respectively. Gas-phase Cl_2, Br_2, I_2, O_2, and H_2O are used as a reference, respectively. Gas-phase O_2 has been corrected as described on reference [24].

Activity volcanoes

In order to establish a volcano-shaped relationship for the activity of the three different oxidation processes we extended the microkinetic model described above using the scaling relations of Figure 4 and the Brønsted-Evans-Polanyi relation that was found for the splitting of O_2.[27] Using the two descriptors, ΔE_{ads}^{OH} and $\Delta E_{diss}^{O_2}$, we obtain the two dimensional volcano plots shown in Figure 5.

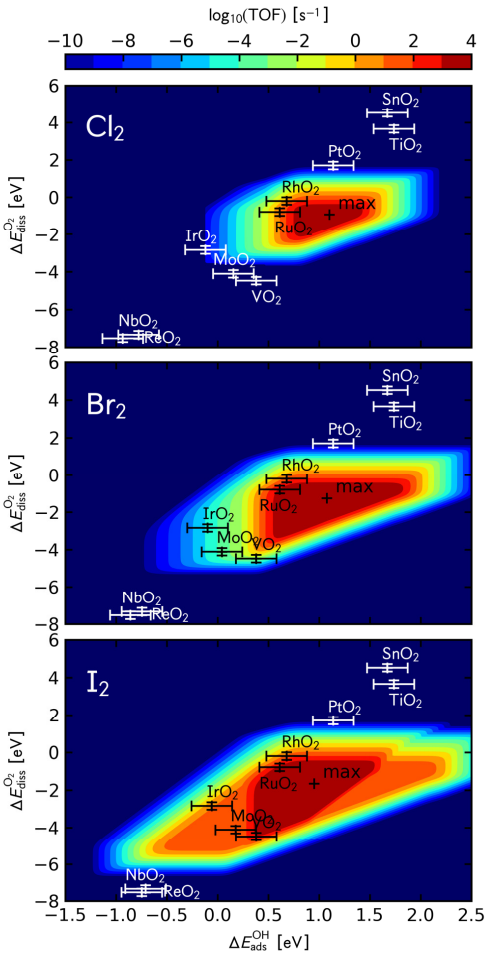

Figure 5. Volcano plots (turnover frequencies (TOFs) plotted as a function of ΔE_{ads}^{OH} and $\Delta E_{diss}^{O_2}$) for HCl, HBr, and HI oxidation. The TOFs are based on a combination of high and low coverage regimes, where the highest rate of these two is plotted. Accordingly, O_2 and OH binding energies of metal oxides employed in this study at high and low coverages are depicted with an error bar of 0.2 eV. Reaction conditions are: 573 K, (pO_2=0.6 bar, pHX=0.3 bar, pH_2O=0.05 bar, and pX_2=0.05bar)

We have treated the case of high and low coverage as two separate models. Figure 5 combines these two models, where the more active one of the two is shown. Accordingly, O_2 dissociation energies and OH adsorption energies are shown for the respective cases of high and low coverage. For all three processes, RuO_2 is the oxide that is closest to the top of the volcano. As expected from the reaction free energies of the different processes, the volcano increases in magnitude when going from Cl to Br to I.

It should be noted that the volcano is quite steep and that the error bars of materials that are located at the edges stretch over three orders of magnitude. This stresses again that our analysis is more of a trend study rather than a quantitative prediction of reaction rates.

Conclusion

We investigated the heterogeneously catalysed oxidation of the three halides HCl, HBr, and HI with molecular oxygen over rutile oxide (110) surfaces. We used the previously established reaction mechanism for HCl oxidation and assume that the HBr and HI oxidation follow a similar reaction mechanism. By employing a full micro-kinetic model without any presumptions on rate determining steps we were able to show that HCl and HBr oxidation over the RuO_2(110) surface are starting at about 500K while HI oxidation already starts at about 400K. Interestingly, HI oxidation was found to occur at low I coverages, whereas high coverages of Cl and Br are needed to facilitate Cl_2 and Br_2 desorption.

We have extended earlier developed scaling relations between different adsorbates on rutile oxide surfaces and were able to describe all three reactions by only two parameters, ΔE_{ads}^{OH} and $\Delta E_{diss}^{O_2}$. These linear energy relations were combined with the micro-kinetic modelling leading to volcano-shaped relationships for HX oxidation. It was found that HX oxidation occurs at high coverages on the strong binding site whereas low coverages yield higher turnovers for the weaker binding oxides. RuO_2 was found to be close to the top of all three oxidation volcanoes. The rate over RuO_2 is observed to increase from chlorine to bromine to iodine. Having established these volcano relationships new catalytic materials could now in principle be screened using simple DFT calculations of adsorption energies of O and OH.

It should be noted that HBr and HI oxidation is analysed under the presumption that the reaction mechanism is similar to that established for HCl. Importantly, further oxidation of Br_2 (I_2) to BrOx species is neglected in this study. Inclusion of further oxidation products might, however, be an important part of the analysis and calls for a treatment on selectivity. In addition, the stability of the catalytic materials and their active surface is not treated in this study and needs to be taken into account in the search for HX oxidation catalysts due to the extremely harsh reaction conditions present.

Calculational details

Density functional theory (DFT) calculations were carried out using the Dacapo code,[28] in which plane waves describe the valence electrons and the core electrons are represented by Vanderbilt ultrasoft pseudo-potentials.[29] The plane wave energy cut-off was 350 eV and the density cutoff 700 eV. All calculations were performed using the RPBE[26] generalized gradient approximation (GGA) functional. The self-consistent electron density was determined by iterative diagonalization of the Kohn-Sham Hamiltonian, with the occupation of the Kohn-Sham states being smeared according to a Fermi-Dirac distribution with a smearing factor of k_bT = 0.1 eV, and Pulay mixing of the resulting electron densities.[30] All energies have been extrapolated to k_bT = 0 eV. The rutile oxide (110) surfaces are modelled by slabs with four metal layers. These are periodically repeated in 1x2 unit cell and separated by 16 Å of vacuum. The Brillouin zone is sampled by a Monkhorst-Pack 4x4x1 *k*-point grid.[31] Two bottom layers are fixed in their bulk structure, while the top layers and possible adsorbates are relaxed until the force of each individual atom is smaller than 0.05 eV/Å. Zero point energy corrections as well as entropies and internal energies of adsorbed species are calculated

using harmonic normal-mode approximation. Entropies and enthalpies of gas phase molecules are obtained from standard table values.[32,33]

Acknowledgements

We acknowledge support for calculational resources from the Danish Center for Scientific Computing (DCSC) and for SUNCAT from the U.S. Department of Energy - Office of Basic Energy Sciences (BES).

Keywords: Deacon • halides • rutile oxides • chlorine production • density functional theory

[1] Chlorine industry review 2009-2010, http://www.eurochlor.org/routes
[2] P. Schmittinger, T. Florkiewicz, L.C. Curlin, B. Lüke, R. Scannell, T. Navin, E. Zelfel, R. Bartsch in *Ullmann's Encyclopedia of Industrial Chemistry*, Wiley-VCH, Weinheim, **2006**.
[3] J. Pérez-Ramírez, C. Mondelli, T. Schmidt, O. F.-K. Schlüter, A. Wolf, L. Mleczko, T. Dreier, *Energy Environ. Sci.* **2011**, *4*, 4786.
[4] Commodity Report 2007: Bromine, United States Geological Survey, http://minerals.usgs.gov/minerals/pubs/commodity/bromine/mcs-2008-bromi.pdf
[5] P.A. Lyday, Iodine and Iodine Compounds, Ullmann's Encyclopedia of Industrial Chemistry, Wiley-VCH (2002)
[6] I. M. Lorkovic, A. Yilmaz, G. A. Yilmaz, X.-P. Zhou, L. E. Laverman, S. Sun, D. J. Schaefer, M. Weiss, M. L. Noy, C. I. Cutler, J. H. Sherman, E. W. McFarland, G. D. Stucky, P. C. Ford, *Catal. Today* **2004**, *98*, 317.
[7] A. Breed, M. Doherty, S. Gadewar, P. Grosso, I. Lorkovic, E. McFarland, M. Weiss, *Catal. Today* **2005**, *106*, 301.
[8] K.H. Büchel, H.-H. Moretto, P. Woditsch, Industrial Inorganic Chemistry, 2nd Ed., Wiley-VCH (2000)
[9] H. Deacon, US patent 165 802, **1875**.
[10] K. Iwanaga, K. Seki, Y. Hibi, K. Issoh, T. Suzuta, M. Nakada, Y. Mori, T. Abe, *Sumitomo Kagaku* **2004**, *1*, 4.
[11] K. Seki, *Catal. Surv. Asia* **2010**, *14*, 168.
[12] F. Studt, F. Abild-Pedersen, H. A. Hansen, I. C. Man, J. Rossmeisl, T. Bligaard, *ChemCatChem* **2010**, *2*, 98.
[13] N. López, J. Gómez-Segura, R.P. Marín, J. Pérez-Ramírez, *J. Catal.* **2008**, *255*, 29.
[14] D. Crihan, M. Knapp, S. Zweidinger, E. Lundgren, C. J. Weststrate, J. N. Andersen, A. P. Seitsonen, H. Over, *Angew. Chem. Int. Ed.* **2008**, *47*, 2131.
[15] S. Zweidinger, D. Crihan, M. Knapp, J. P. Hofmann, A. P. Seitsonen, C. J. Weststrate, E. Lundgren, J. N. Andersen, H. Over, *J. Phys. Chem. C* **2008**, *112*, 9966.
[16] A. P. Seitsonen, H. Over, *J. Phys. Chem. C* **2010**, *114*, 22624.
[17] F. Abild-Pedersen, J. Greeley, F. Studt, J. Rossmeisl, T. R. Munter, P. G. Moses, E. Skúlason, T. Bligaard, J. K. Nørskov, *Phys. Rev. Lett.* **2007**, *99*, 016105.
[18] G. Jones, F. Studt, F. Abild-Pedersen, J. K. Nørskov, T. Bligaard, *Chem. Eng. Sci.* **2011**, *66*, 6318.
[19] J. Rossmeisl, Z.-W. Qu, H. Zhu, G.-J. Kroes, J. K. Nørskov, *J. Electroanal. Chem.* **2007**, *607*, 83.
[20] E. M. Fernández, P. G. Moses, A. Toftelund, H. A. Hansen, J. I. Martínez, F. Abild-Pedersen, J. Kleis, B. Hinnemann, J. Rossmeisl, T. Bligaard, J. K. Nørskov, *Angew. Chem. Int. Ed.* **2008**, *47*, 4683.
[21] H. A. Hansen, I. C. Man, F. Studt, F. Abild-Pedersen, T. Bligaard, J. Rossmeisl, *Phys. Chem. Chem. Phys.* **2010**, *12*, 283.
[22] J.K. Nørskov, J. Rossmeisl, A. Logadottir, L. Lindqvist, J.R. Kitchin, T. Bligaard, H. Jonsson, *J. Phys. Chem. B* **2004**, *108*, 17886-17892.
[23] I.C. Man, H-Y Su, F. Calle-Vallejo, H.A. Hansen, J. I. Martinez, N.G. Inoglu, J. Kitchin, T.F. Jaramillo, J.K. Nørskov, and J. Rossmeisl, *ChemCatChem* **2011**, *3*, 1159
[24] J. Rossmeisl, A. Logadottir, J. K. Nørskov, *Chem. Phys.* **2005**, *319*, 178.
[25] J. J. Mortensen, L. B. Hansen, K. W. Jacobsen, *Phys. Rev. B* **2005**, *71*, 035109.
[26] B. Hammer, L. B. Hansen, J. K. Nørskov, *Phys. Rev. B* **1999**, *59*, 7413.
[27] A. Vojvodic, F. Calle-Vallejo, W. Guo, S. Wang, A. Toftelund, F. Studt, J. I. Martínez, J. Shen, I. C. Man, J. Rossmeisl, T. Bligaard, J. K. Nørskov, F. Abild-Pedersen, *J. Chem. Phys.* **2011**, *134*, 244509.
[28] The Dacapo plane wave/pseudopotential code is available as open source software at http://wiki.fysik.dtu.dk/dacapo.
[29] D. Vanderbilt, *Phys. Rev. B* **1990**, *41*, 7892.
[30] G. Kresse, J. Furthmüller, *Comput. Mater. Sci.* **1996**, *6*, 15.
[31] H. J. Monkhorst, J. D. Pack, *Phys. Rev. B* **1976**, *13*, 5188.
[32] P.W. Atkins and Julio de Paula, Physical Chemistry, 8th Ed. Oxford University Press, **2006**
[33] M.W. Jr. Chase, *NIST-JANAF Themochemical Tables*, 4th Ed., J. Phys. Chem. Ref. Data, Monograph 9, **1998**, pp. 1-1951

Received: ((will be filled in by the editorial staff))
Published online: ((will be filled in by the editorial staff))

Paper IV

Supplementary materials

Calculated Phase diagrams

As shown in Figure 1 RuO_2 (110) surface exposed to HCl will have 50% of the bridging oxygen atoms exchanged by chlorine atoms under reaction conditions relevant to the Deacon process [1]. The same is observed for both RuO_2 and the PtO_2 exposed to HBr or HI, see Figure 2. At IrO_2 and TiO_2, however, the bridging oxygen atoms remain under same conditions in all three cases of hydrogen halides.

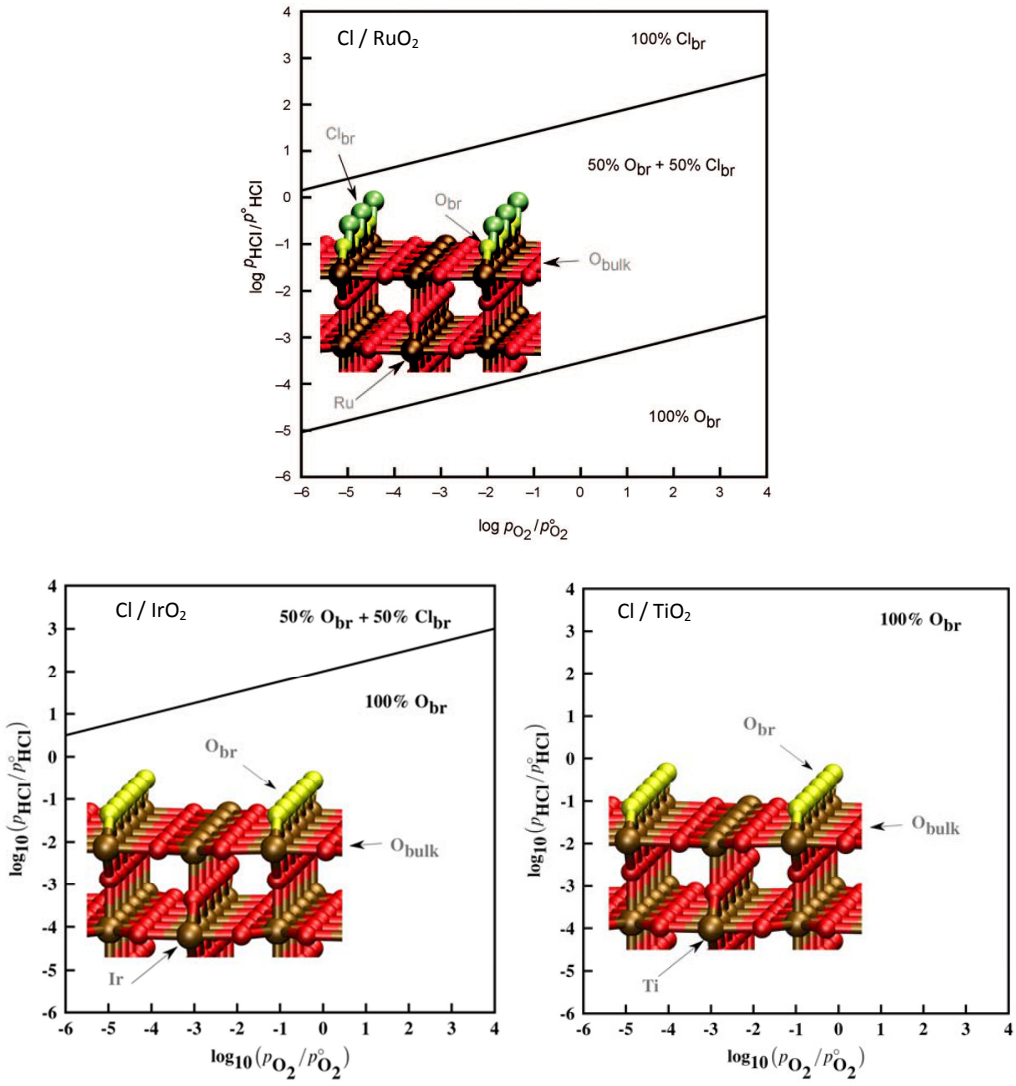

Figure 1: Stability range of different rutile oxide (110) surfaces for bridge adsorbed 100% O, 50% O +50% Cl and 100% Cl as a function of O_2 and HCl pressure at 573 K. Obtained from DFT calculations. Adapted from [1].

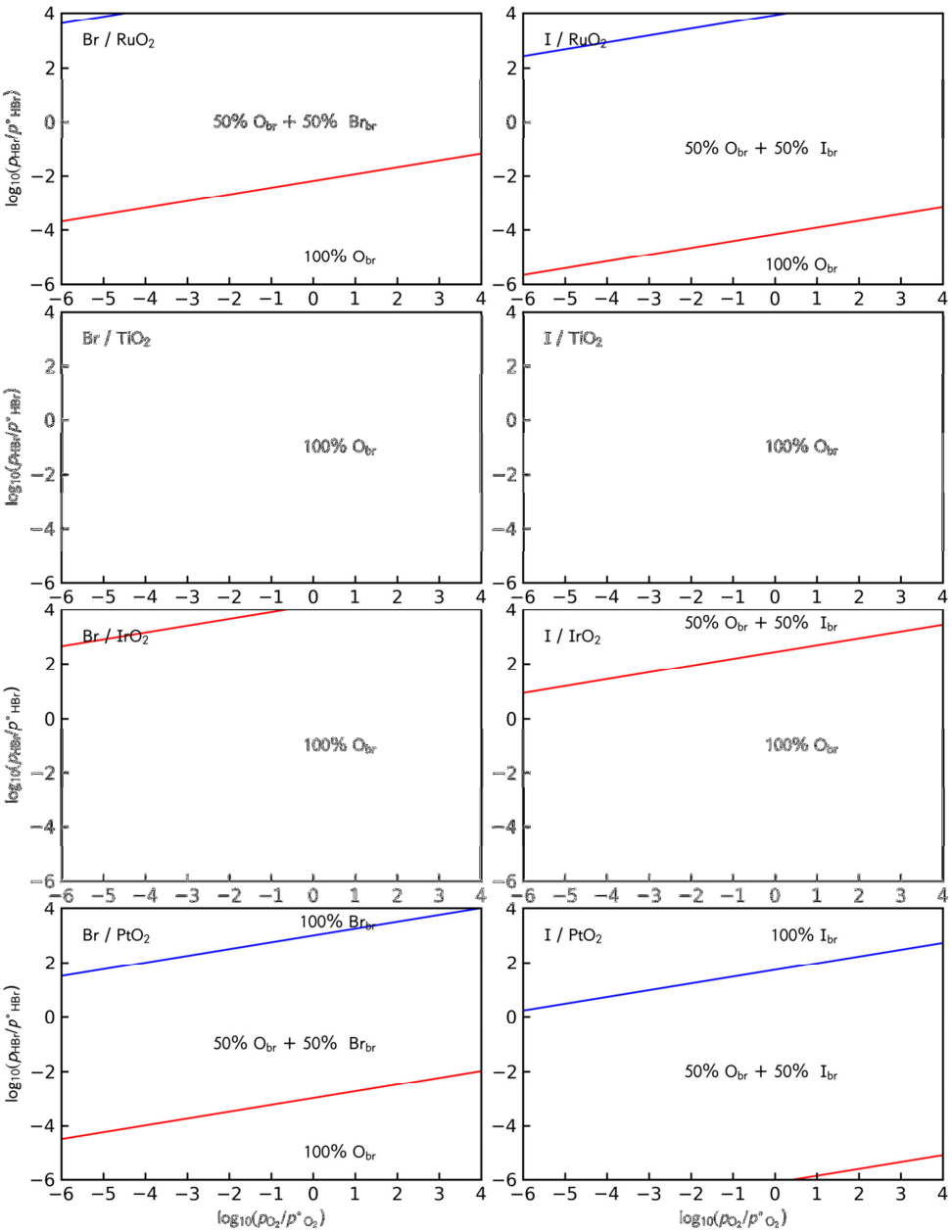

Figure 2: Stability range of different rutile oxide (110) surfaces for bridge adsorbed 100% O, 50% O +50% X and 100% X (X=Br,I) as a function of O_2 and HX pressure at 573 K. Obtained from DFT calculations.

Micro-kinetic model

The five elementary reaction steps in our micro-kinetic model are

1) $O_2 + 2* \rightarrow O_2{**}$

2) $O_2{**} \rightarrow 2O*$

3) $O* + * + HX \rightarrow OH* + X*$

4) $2X* \rightarrow X_2 + 2*$

5) $2OH* \rightarrow O* + * + H_2O$

where * denotes an empty site on the surface and X can be either Cl, Br or I. Following system of equations is solved with respect to the coverages of the four different surface species θ_{O_2}, θ_O, θ_X and θ_{OH}:

$$r_1 = r_2, \qquad r_2 = 4r_3, \qquad 2r_3 = r_4, \qquad r_4 = r_5 \quad \text{and} \quad \theta_{O_2} + \theta_O + \theta_X + \theta_{OH} + \theta_* = 1 \tag{1}$$

Where $0 < \theta_A < 1$ (A = O_2, O, X, OH, *). The reaction rates, r_i ($i = 1,2,3,4,5$), for the five elementary reaction step above are given by

$$r_1 = k_1 p_{O_2} \theta_*^2 - \frac{1}{2} k_{-1} \theta_{O_2} \tag{2}$$

$$r_2 = \frac{1}{2} k_2 \theta_{O_2} - k_{-2} \theta_O^2 \tag{3}$$

$$r_3 = k_3 p_{HX} \theta_O \theta_* - k_{-3} \theta_{OH} \theta_X \tag{4}$$

$$r_4 = k_4 \theta_X^2 - k_{-4} p_{X_2} \theta_*^2 \tag{5}$$

$$r_5 = k_5 \theta_{OH}^2 - k_{-5} p_{H_2O} \theta_O \theta_* \tag{6}$$

p_M (M = XH, O_2, Cl_2, H_2O) denotes the partial pressures of the gas phase molecules.

The equilibrium constant of reaction i is given by

$$K_i = e^{\frac{-\Delta G_i}{kT}}, \qquad i = 1,2,3,4,5 \tag{7}$$

where k is Boltsmann's constant, T is the reaction temperature and the reaction free energy, ΔG_i, is calculated as

$$\Delta G_i = \Delta E_i + \Delta H_i^{0,T} - T\Delta S_i \tag{8}$$

where ΔE_i is the change in reaction energy calculated with DFT and zero-point corrections included. $\Delta H_i^{0,T}$ is the part of the change in enthalpy that arises from raising the temperature from 0 K to T, and ΔS_i is the change in entropy. The forward and backward rate constants k_i and k_{-i} are given by:

$$k_i = \frac{kT}{h} e^{\frac{-\Delta G_i^+}{kT}} \qquad \text{and} \qquad k_{-i} = \frac{k_i}{K_i} \tag{9}$$

Where h is Planck's constant, and ΔG_i^+ defined as

$$\Delta G_i^+ = \Delta E_i^+ + \Delta H_i^{0,T+} - T\Delta S_i^+ \quad (10)$$

is the effective activation barrier of the reaction step i. The values included in equation (10) (marked with superscript +, are usually obtained from systems in transition state configuration. On rutile oxides, however, it is found that in many cases the dissociation of dimers over cus-cus only have the barrier given by the change in reaction energy[2]. If an extra transition state barrier exists it is found to be very small, and is therefore neglected in this work. In order to be able to use transition state theory as in Equation (9), although no real transition state saddle point is found, following is used for the transition state values.

$$\Delta E_i^+ = \Delta E_i \ \text{ for } \ \Delta E_i \geq 0 \qquad \text{and} \qquad \Delta E_i^+ = 0 \ \text{ for } \ \Delta E_i < 0 \quad (11)$$

and

$$\Delta H_i^{0,T+} - T\Delta S_i^+ = \Delta H_i^{0,T} - \mathrm{T}\Delta S_i \quad \text{for} \quad \Delta H_i^{0,T} - \mathrm{T}\Delta S_i \geq 0 \quad \text{and}$$
$$\Delta H_i^{0,T+} - T\Delta S_i^+ = 0 \quad \text{for} \quad \Delta H_i^{0,T} - \mathrm{T}\Delta S_i < 0 \quad (12)$$

For an exothermic adsorption step, where ΔE_i as well as ΔS_i is negative equation (11) and (12) gives an effective activation barrier of $\Delta G_i^+ = \Delta H_i^{0,T} - \mathrm{T}\Delta S_i$.

Sensitivity test

In the following we apply an error of 0.2 eV to the adsorption energy of chlorine, $\Delta E_{\mathrm{ads}}^{\mathrm{Cl}}$, on RuO_2 in order to estimate the influence on the onset temperature for Cl_2 production and the overall reaction rate. We assume here that reaction step 4), the recombination of chlorine is rate determining and only the forward rate is important. Furthermore we assume and that the coverage of chlorine, θ_{Cl} , is constant and equal to one. This is reasonable, as θ_{Cl} of RuO_2 obtained with the full micro-kinetic model described above is close to one in a broad range near the onset temperature. ΔE_4 is positive and there is an increase in entropy. Therefore a decrease in $\Delta U_4 - \mathrm{T}\Delta S_4$. From equation (10), (11) and (12) we, therefore, have that the effective energy barrier is $\Delta G_4^+ = \Delta E_4 = -2\Delta E_{\mathrm{ads}}^{\mathrm{Cl}}$. With these assumptions the overall rate becomes

$$r = k_4 = \frac{kT}{h} e^{\frac{-\Delta E_4}{kT}} \quad (13)$$

Applying an error δ in the effective barrier results in a shift in onset temperature ΔT and following expression is valid.

$$r = \frac{kT}{h} e^{\frac{-\Delta E_4}{kT}} = \frac{kT}{h} e^{\frac{-(\Delta E_4 + \delta)}{k(T+\Delta T)}} \quad (14)$$

This can be rearranged into

$$\Delta T = \frac{\delta T}{\Delta E_4} \quad (15)$$

Shifting $\Delta E_{\mathrm{ads}}^{\mathrm{Cl}}$ by -0.2 eV from -0.65 eV to -0.85 eV, i.e. δ=0.4 eV, and choosing the temperature T=473 K, which is close to the onset temperature of Cl_2 production, we get a shift ΔT=146 K in temperature. Note that for lower barriers or higher temperatures this shift will be even larger.

Similar the sensitivity of the reaction rate can be estimated by

$$\frac{kT}{h}e^{\frac{-(\Delta E_4+\delta)}{kT}} = re^{-\frac{\delta}{kT}} \quad (16)$$

This means that if we apply an error, δ, to the barrier the rate will change with a factor of $e^{-\delta/(kT)}$. If we set δ=0.4 eV and T=573 K, the temperature at which the volcano plots in figure 5 in the main paper are calculated, this factor is as much as 3.0×10^{-4}.

Quality test with GPAW

Figure 3 in the main paper, shows a strong linear correlation between the dissociative chemisorption energy of O_2, $\Delta E_{\mathrm{diss}}^{\mathrm{O_2}}$, and the adsorption energy of OH, $\Delta E_{\mathrm{ads}}^{\mathrm{OH}}$. A few surfaces, however, deviate significant from the line. In order to check the quality of the calculations the values for IrO_2 and RuO_2 was recalculated in the all electron DFT code GPAW [3]. The result is shown in Figure 3. It can be seen that even though the new values differ slightly from the values obtained with Dacapo, they do not improve the overall scaling relation.

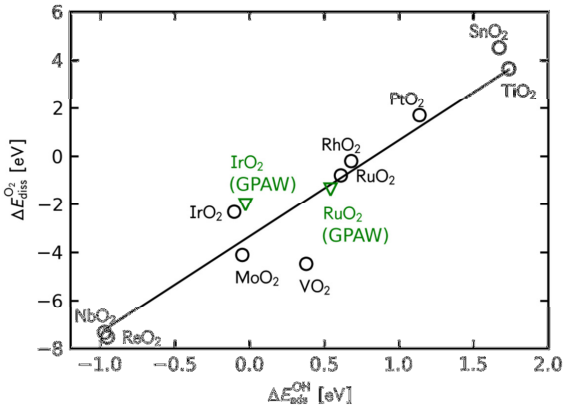

Figure 3: Dissociative chemisorption energy of O_2 ($\Delta \boldsymbol{E}_{\mathbf{ads}}^{\mathbf{OH}}$) calculated by DFT and plotted as a function of the adsorption energy of OH ($\Delta \boldsymbol{E}_{\mathbf{ads}}^{\mathbf{OH}}$) as obtained from DFT calculations. Energies shown with black circles are calculated with Dacapo [4] and green triangle with GPAW [1].

Volcanoes

Figure 5 in the main paper shows volcano plots, which combine a high and a low coverage model by showing the more active for each point. Figure 4 shows the volcano plots for each of the models separately.

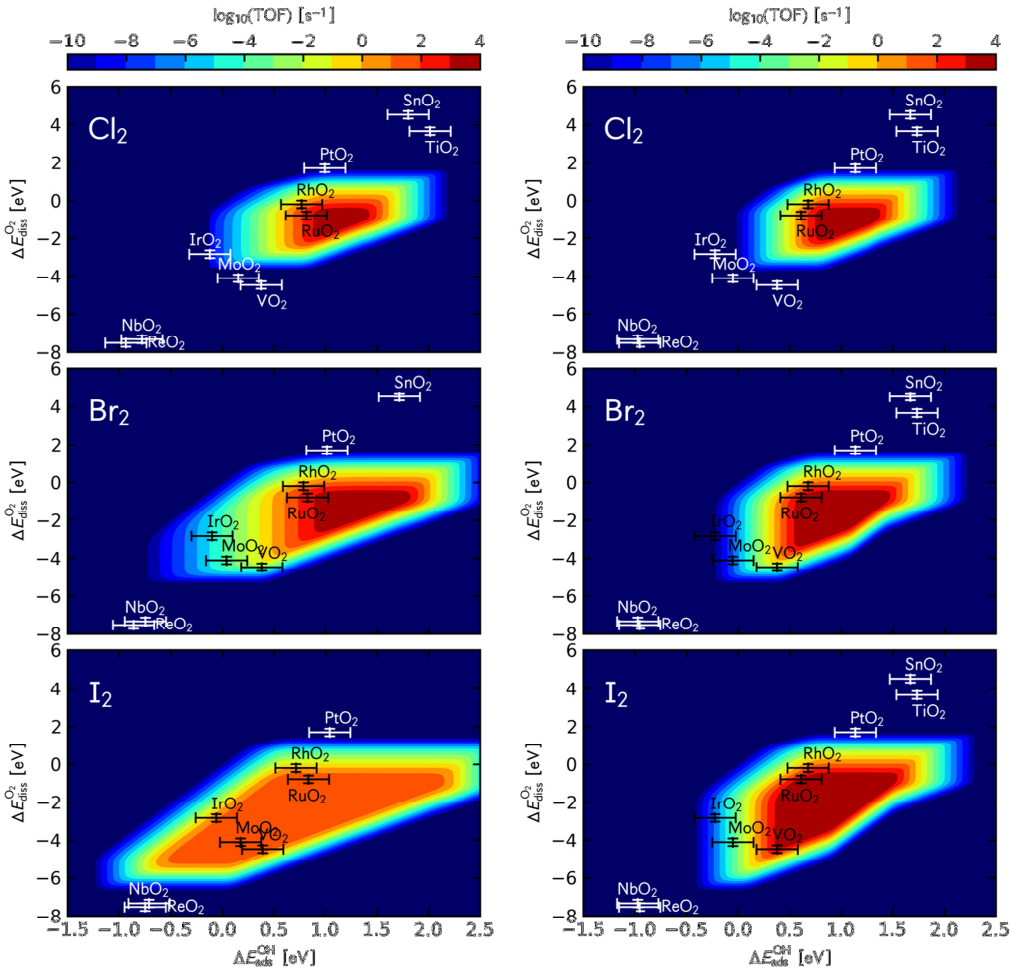

Figure 4: Volcano plots (turnover frequencies (TOF)) plotted as a function of the dissociative chemisorption energy of O_2, $\Delta E_{\mathrm{diss}}^{\mathrm{O_2}}$, and the adsorption energy of OH, $\Delta E_{\mathrm{ads}}^{\mathrm{OH}}$) for HCl, HBr and HI oxidation. Left: High coverage model, where adsorption of the halide atom and OH is calculated with halides as next neighbors. Right: Low coverage model, where adsorption of the halide atom and OH is calculated with no nearest neighbors. Otherwise the two models are identical.

[1] F. Studt, F. Abild-Pedersen, H. A. Hansen, I. C. Man, J. Rossmeisl, T. Bligaard, *ChemCatChem* **2010**, *2*, 98.

[2] A. Vojvodic, F. Calle-Vallejo, W. Guo, S. Wang, A. Toftelund, F. Studt, J. I. Martínez, J. Shen, I. C. Man, J. Rossmeisl, T. Bligaard, J. K. Nørskov, F. Abild-Pedersen, *J. Chem. Phys.* **2011**, *134*, 244509.

[3] GPAW Grid base projector augmented-wave method DFT code is available as open source sofware at wiki.fysik.dtu.dk/gpaw

[4] Dacapo plane waves/pseudopotential DFT code is is available as open source sofware at wiki.fysik.dtu.dk/dacapo